# Complementary visualization of the pseudogap states in $Bi_2Sr_2CaCu_2O_{8+\delta}$: SI-STM study in real and momentum space

A Dissertation
Presented to the Faculty of the Graduate School
of Cornell University
in Partial Fulfillment of the Requirements for the Degree of
Doctor of Philosophy

by
Chung Koo Kim
May 2013

COMPLEMENTARY VISUALIZATION OF THE PSEUDOGAP STATES IN $Bi_2Sr_2CaCu_2O_{8+\delta}$: SI-STM STUDY IN REAL AND MOMENTUM SPACE

Chung Koo Kim, Ph.D.

Cornell University 2013

The high-temperature superconductivity has remained one of the most puzzling phenomena in contemporary condensed matter physics since its discovery in 1986. Despite enormous quantity of experimental results and theoretical proposals over 25 years, the pairing glue as well as the nature of the normal states are still not clearly identified. The enigmatic pseudogap phase, characterized by the loss of spectral weight above the superconducting transition temperature ($T_c$), is believed to be a key to understanding the superconductivity. This dissertation primarily investigates the underdoped BSCCO, a double layered cuprate perovskite which exhibits pseudogap over wide range.

Spectroscopic-Imaging Scanning Tunneling Microscopy (SI-STM) is a unique probe in that it allows simultaneous access to complimentary spaces. For SI-STM can visualize the electronic structure of a physical system with atomic resolution and register in real space, with its Fourier-transform revealing the dispersion of quasiparticle excitations in momentum space.

Three discoveries made with SI-STM are presented here. First, the real-space electronic nematicity observed within $CuO_2$ unit cell demonstrates that the C4 rotational symmetry of the underlying crystal lattice is broken into the C2 symmetry in the electronic structure. Inequivalence of the orthogonal crystallographic axes narrows down the possible models for pseudogap in favor of stripe order.

Momentum space provides two other discoveries. Ratio of the differential conductance data measured at opposite bias voltage, which amplifies the particle-hole symmetric dispersion of the Bogoliubov quasiparticle, shows that the pseudogap state retains the tri-partite electronic excitation structure present below $T_c$. The signature of the Cooper pairs without long-range phase coherence renders the pseudogap as a pre-cursor to the superconducting state. In contrast, the anti-nodal charge-ordering dominant in the raw data but washed out

in the ratio map is found to weakly disperse in a continuous but asymmetric manner. The peculiarity of the dispersion distinct in the strongly underdoped regime of cuprate family with high maximum $T_c$ is discussed in the context of the low-energy psdueogap in the last chapter.

# BIOGRAPHICAL SKETCH

Chung Koo grew up in Suwon, now a big city where Samsung Electronics manufactures memory devices. He was born inclined to the arcane language of mathematics, a little kid pleasantly skimming through his sister's algebra books without even understanding a single line. Inspired by his brother, high school teacher and friends, his interest turns to physics, to which he returned after 4-year digression into electronics major in undergraduate days. Chung Koo's ever-growing experience in bringing the electronics into advancing atomic scale physics led him to Cornell to Brookhaven, where he needs a light to find his way in science, as well as in science lab located in the basement.

*To Hyelin, my love*

# ACKNOWLEDGEMENTS

First of all, it was such a great honour, privilege, and luck to work with professor Séamus Davis as an advisor, whose support I truly appreciate made each and every piece of work presented here possible. His passion for discovery, persistence on incremental improvement, respectful and intellectual interaction with people were always exemplary of a distinguished scholar. I only wish I can distribute his legacy around.

A very special thanks goes to Dr. Kazuhiro Fujita, who was always more than willing to answer to my endless questionnaire from the beginning of my PhD course. It must have taken a lot longer for me to learn about and get used to the high-$T_c$ superconductivity field without him. I am also greatly indebted to Dr. Jinho Lee as an on-site supervisor in Brookhaven National Laboratory(BNL). His phenomenal tenacity in problem solving was very influential. I would like to thank Dr. Jhinhwan Lee too for many lessons including his dexterous craftsmanship of elaboration. I appreciate Dr. Tien-Ming Chuang for being my immediate role model as a balanced researcher with smile. And I thank Dr. Inhee Lee, who taught me the importance of interaction with people from other fields and experience, and who greatly helped me out of burden during the extended period of my thesis writing.

I thank other colleagues, in particular, Dr. Vikram Gadagkar, a thoughtful listener who always shared my story with sympathy, Dr. Mohammad Hamidian, a classmate and a labmate who led me into higher standards, and Inês Firmo, for the big help in BNL STM repair.

It was a great pleasure to happily interact with: Dr. Ethan Pratt, Dr. Benjamin Hunt, Dr. Milan Allan, Yang Xie, Dr. Andy Schmidt, Dr. Jacob Alldredge, Dr. Curry Taylor, Dr. Alfred Wang, Dr. Minoru Yamashita, Dr. Andreas Rost, Dr. Jean-Philippe Reid, Dr. Freek Massee, Ethan Kassner, Andrey Kostin, Hiro Miyake, Warasinee Chaisangmongkon, Chris Gerig, Neal Harrington, Jong Min Yoon.

I am grateful to a number of faculty. First of all, prof. Eun-Ah Kim and Kyle Shen for providing insightful feedback at critical moments. Prof. Piet Brouwer, whom I taught P327 with, teaching me how best to teach students. Prof. Tomas Arias, for his energetic input to a lecture. Prof. James Sethna for his warm-hearted support for students. I also would like to express my appreciation to BNL senior scientists including Peter Johnson,

John Tranquada, Yimei Zhu, and Ivan Bozovic for their interest and feedback on STM experiments.

I should also acknowledge technical and administrative staffs in Cornell as well as BNL: Rodney Bowman, Nick Brown, Nathan Ellis, Harold Wiesman, William Leonhardt, Jim O'Malley, Omar Lee, Eileen Levine.

I was fortunate to have good friends who were invaluable in helping me through hard times: Oukjae, Jeehye, Woo song, Jeonghoon, Hongwoo, Jungwook, Ho sung, Poegeun, and all others for whom I feel sorry for not having enough space to name. But most importantly, I would have been able to achieve none of these without immeasurable encouragement and love of my parents, family, and my wife Hyelin. The present thesis is dedicated to them.

# Contents

# List of Figures

# Chapter 1

# High-temperature superconductivity and cuprates

## 1.1 Conventional superconductivity

### 1.1.1 Weak-coupling : BCS theory

Superconductivity was first discovered in 1911 when Heike Kamerlingh Onnes observed abrupt resistance drop in solid mercury at 4.2K.[1] Since the seminal theoretical explanation by Bardeen, Cooper and Schrieffer(BCS theory),[2] it is now well understood that the conventional superconductivity results from the second-order phase transition due to the condensation of the Cooper pairs into a macroscopic wavefunction.

In most elements in their solid state, the electrons interact with each other via screened Coulomb repulsion as well as the Frölich interaction of the form[3]

$$V(\mathbf{q}) = \frac{4\pi e}{q^2 + \lambda^2} + \frac{2\hbar\omega_{\mathbf{q}}|M_{\mathbf{q}}|^2}{(\epsilon_{\mathbf{k}} - \epsilon_{\mathbf{k}+\mathbf{q}})^2 - (\hbar\omega_{\mathbf{q}})^2}. \tag{1.1.1}$$

$1/\lambda$ gives the screening length scale, and the second term represents the strength of the second-order process in which electrons exchange virtual phonon of momentum $\mathbf{q}$. Evidently,

the net interaction can be attractive provided that the Frölich interaction becomes negative overwhelming the electron repulsion.

The Debye energy $\hbar\omega_D$, or the upper bound of the phonon energy $\hbar\omega_q$ is very small compared to the Fermi energy as $\hbar\omega_D/E_F \sim \sqrt{m/M}$. Therefore net attractive interaction occurs only for small $q$, and consequently for $\epsilon_k$ within the same small energy range around $E_F$. In short, the Fermi sea is unstable against the formation of a bound pair of electrons in momentum space. Under the assumption of zero center-of-mass (COM) momentum and zero total spin of the pair, the pair-binding energy, or the shift of the energy eigenvalue evaluates to[4]

$$\begin{aligned}\Delta &= \frac{2\hbar\omega_D}{\exp(2/V_0N(E_F)) - 1} \\ &\sim 2\hbar\omega_D \cdot \exp(-2/V_0N(E_F))\end{aligned}$$

where $V_0$ and $N(E_F)$ represent the strength of the simplified $s$-wave pair-scattering matrix element and the density of states at the Fermi energy, respectively, and the approximation is valid in the weak-coupling limit $V_0N(E_F) \ll 1$. The singularity of the exponent prohibits perturbational approach in any order, which is a characteristic of phase transitions for which Green's function in matrix form is required.[3] Reduced binding energy for non-zero COM momentum, and the vanishing scattering amplitude for pairs with parallel spins validates the assumption of the zero COM momentum and total spin.[4]

Extending the one-pair problem, BCS constructed many-body superconducting ground state in a form which pairing is already incorporated:

$$|\Psi_{BCS}\rangle = \prod_{\mathbf{p}} (u_{\mathbf{p}} + v_{\mathbf{p}} a^\dagger_{\mathbf{p}\uparrow} a^\dagger_{\text{-}\mathbf{p}\downarrow})|0\rangle.$$

The coherence factors $u_{\mathbf{p}}$ and $v_{\mathbf{p}}$ are the probability amplitude that the pair-quasiparticle-state $(\mathbf{p}\uparrow, \text{-}\mathbf{p}\downarrow)$ is empty and occupied such that $|u_{\mathbf{p}}|^2 + |v_{\mathbf{p}}|^2 = 1$ from the closure relation or by definition. Minimizing the ground-state energy under this restriction using variational method not only determines $u_{\mathbf{p}}$ and $v_{\mathbf{p}}$, but also defines the superconducting order parameter in terms of the pair scattering potential

$$\Delta_{\mathbf{p}} = -\sum_{\mathbf{p}'} V_{\mathbf{p}\mathbf{p}'} u^*_{\mathbf{p}'} v_{\mathbf{p}'} = -\sum_{\mathbf{p}'} V_{\mathbf{p}\mathbf{p}'} \frac{\Delta_{\mathbf{p}'}}{2\sqrt{{\epsilon_{\mathbf{p}'}}^2 + |\Delta_{\mathbf{p}'}|^2}} \tag{1.1.2}$$

as well as the condensation energy

$$\Delta E = E_s - E_n = -\frac{N(E_F - \mu)\Delta^2}{2}$$

which can also be obtained from thermodynamics.

Quasi-particle excitation of the above ground state can be described not by either electron creation or annihilation operator alone, but by a linear combination of them

$$\gamma^\dagger_{\mathbf{p}\uparrow} = u^*_{\mathbf{p}} a^\dagger_{\mathbf{p}\uparrow} - v^*_{\mathbf{p}} a_{\text{-}\mathbf{p}\downarrow}$$

following the Bogoliubov transformation.[5] Writing the coupled equations of motion between $a_{\mathbf{p}\uparrow}$ and $a^\dagger_{\text{-}\mathbf{p}\downarrow}$, and diagonalizing the matrix Hamiltonian gives the dispersion of the quasi-particle[4]

$$\varepsilon_{\mathbf{p}} = \sqrt{{\epsilon_{\mathbf{p}}}^2 + |\Delta_{\mathbf{p}}|^2},$$

where the minimum excitation energy or gap $\Delta_{\mathbf{p}}$ opens in the normal-state band $\epsilon_{\mathbf{p}}$. Note that this term is already present in the self-consistent gap equation 1.1.2. Again, if the pair scattering interaction $V_{\mathbf{pp}'}$ is approximated by an s-wave potential, the solution to the eq. 1.1.2 can be explicitly obtained to be isotropic,[6] implying an s-wave superconducting order parameter.

### 1.1.2 Strong-coupling : Eliashberg formalism

The superconductivity observed in many pure metals, including their magnetic and thermodynamic properties, are well described by the weak-coupling theory as above. Ironically, in solid mercury, the first superconducting material, the electron-phonon interaction is rather strong so that the weak-coupling theory is not a proper framework. In strong-coupling superconductors such as lead and mercury, electron and phonon interacts over a finite time duration rather than instantaneously. As a result the Frölich term in eq. 1.1.1 is no longer valid; it has to be replaced by a frequency-dependent form incorporating the retarded nature of the interaction. Moreover, including the time (or frequency) degree of freedom also requires reconstructing the entire formalism using Green's function which naturally deals

with the frequency at equal footing with the momentum. In fact, the BCS theory is the static approximation of the generalized Eliashberg strong-coupling theory.

In diagrammatic approach, the 'bubble' diagram within the Random Phase Approximation (RPA) renormalizes all interactions between charged particles through frequency-dependent dielectric function $\kappa(\mathbf{q},\omega)$. First, the screened $e$-$e$ repulsion becomes

$$V_c^{RPA}(\mathbf{q},\omega) = \frac{V(q)}{1+V(q)P^{RPA}(\mathbf{q},\omega)} = \frac{V(q)}{\kappa(\mathbf{q},\omega)}$$

where the bare Coulomb interaction $V(q) = 4\pi e^2/q^2$ is a function of $q^2$ only. Next, the dressed phonon propagator reads

$$D_l(\mathbf{q},\omega) = \frac{2\Omega_{ql}}{q_0^2 - (\Omega_{ql}^2/\kappa(\mathbf{q},\omega)) + i\delta}$$

in which the characteristic frequency (ionic plasma frequency) is given by $\Omega_{ql}^2 = 4\pi nZe^2/M$. Lastly, the electron-phonon vertex $g_{ql}$ is also modified into the screened matrix element $\bar{g}_{ql} = g_{ql}/\kappa(\mathbf{q},\omega)$.

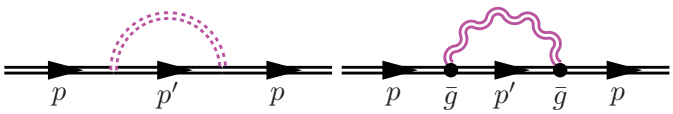


FIGURE 1.1: **Exchange interactions for strong-coupling theory.** Diagrams for the lowest-order self-consistent perturbation theory. Contribution from (left) the screened Coulomb interaction and (right) the dressed virtual phonon exchange. Double solid line for the Green's function is also self-consistently determined.

The electron self-energy $\Sigma(\mathbf{p},\omega)$ can be evaluated with the first-order self-consistent perturbation theory involving exchange correction due only to the above generalized interactions (see Fig. 1.1). In a scheme developed by Nambu,[7] 2×2 matrix Matsubara Green's function which has the pairing correlation embedded inside does the task neatly:

$$\mathbf{G}_0(\mathbf{p},\omega)^{-1} = \omega\mathbf{1} - \epsilon_{\mathbf{p}}\tau_3 + i\delta\omega\mathbf{1}$$

Here $\mathbf{1}$ and $\tau_3$ denotes the unit matrix and the Pauli matrix $\sigma_z$. After lengthy calculations, Eliashberg[8] was able to obtain the electron self-energy $\Sigma(\omega)$ as well as the cross-coupled

renormalization factor $Z(\omega)$ and the frequency-dependent gap $\Delta(\omega)$, in terms of the effective electron-phonon interaction which is the product of the phonon density of states $F(\omega)$ and the electron-phonon coupling $\alpha^2(\omega)$. The final form of the gap parameter at zero temperature is[9]

$$\Delta(\omega) = \left[\mu^* - \int_{\Delta_0}^{\infty} d\omega_0 \alpha^2(\omega_0) F(\omega_0) \left(\frac{1}{\omega' + \omega + \omega_0 - i\delta} + \frac{1}{\omega' - \omega + \omega_0 - i\delta}\right)\right] \times \frac{1}{Z(\omega)} \int_{\Delta_0}^{\infty} d\omega' \mathrm{Re}\left[\frac{\Delta(\omega')}{\sqrt{\omega'^2 - [\Delta(\omega')]^2}}\right]. \tag{1.1.3}$$

Tunneling density of states (the integrand in the second integral of eq. 1.1.3) calculation as in figure 1.2 is one example testifying the great success of the strong-coupling theory. In a density of states ratio plot between the superconducting and the normal state, strong-coupling theory predicts a complicated structure[10] unlike the monotonous BCS counterpart, which agrees remarkably well with the experiment by Rowell *et al.*[11]

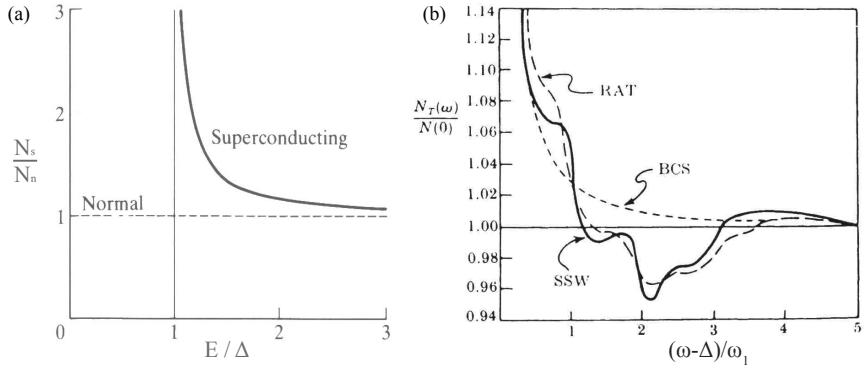


FIGURE 1.2: **Strong Coupling: deviation from the weak-coupling prediction.** (a) Density of states in an isotropic gap superconductor compared to the normal state is predicted by BCS theory to be a monotonously decreasing function starting from the singularity at the gap edge.[12] (b) Tunneling experiment by RAT (Rowell, Anderson, Thomas) on a Pb-($Al_2O_3$)-Al junction[11] reveals intricate features beyond BCS prediction, which is very similar to the calculation by SSW (Schrieffer, Scalapino, Wilkins)[10] with strong-coupling theory.[6]

## 1.2 The advent and advance of High-Tc superconductivity

BCS theory extended into the strong electron-phonon coupling cases has been a successful formalism in explaining the conventional low-temperature superconductors over many years. However, the recent discovery of the superconductivity of fundamentally different origin demands a significant revision of the BCS-Eliashberg theory or even a new picture. For the first step, the new superconducting materials are briefly reviewed in chronological order of their first discovery.

### 1.2.1 Non-cuprate

#### Heavy-Fermion compounds

In intermetallic compounds containing elements such as Uranium or Cerium, the normal conduction electrons hybridize with the $f$-electrons into a flat DOS near Fermi energy below the 'hidden order' transition temperature.[13] The effective mass of the quasiparticles associated with the hybridized band is about 30 times that of the free electron, thus giving the name Heavy Fermion. The superconductivity in heavy Fermion compound was first discovered by Steglich in 1978, from measurement of both specific heat and the resistivity of $CeCu_2Si_2$ at 0.51K.[14] One counter-intuitive aspect of the heavy Fermion superconductivity is that it coexists with the magnetic order by localized $f$-electrons, which is detrimental to the superconductivity in BCS picture. In fact, the fluctuation of the magnetic order itself is believed to be the pairing glue of the Cooper pairs in this group of material. Due to the discovery of half of the 30+ known compounds so far within the past 8 years, out of its history over 30 years,[15] heavy Fermion superconductivity became a very active field recently. $T_c$ of this class is about 1K, with 2.3K on $CeCoIn_5$ being the highest.[16]

#### Organic compounds

Superconductivity in organic material is of particular interest as the compounds are made of carbon and hydrogen, the most abundant elements on earth. The first compound $(TMTSF)_2PF_6$ (Tetra-Methyl-Tetra-Selena-Fulvalene) discovered in 1979 develops superconductivity out of quasi-one-dimensional spin density wave(SDW) ground state beyond

6.5kbar[17] with $T_c$=1.1K. Two-digit $T_c$ can be achieved with quasi-two-dimensional superconductor that followed the 1D predecessor, for example $\kappa$-(BEDT-TTF)$_2$Cu(NCS)$_2$ (Bis-Ethylene-Di-Thio-Tetra-Thia-Fulvalene, $T_c$=10.4K at ambient pressure).[18] Besides exhibiting antiferromagnetism, some 2D materials indicate the existence of the exotic Fulde-Ferrell-Larkin-Ovchinnikov (FFLO) phase.[19] Two other important families of organic superconductor are Fullerene compound doped with interstitial alkali metal such as $Rb_3C_{60}$ with $T_c$ over 30K,[20] and graphite intercalation compound such as $CaC_6$.[21]

### Ruthenates

Single layered member of $Sr_{n+1}Ru_nO_{3n+1}$ Ruddlesden-Popper series exhibits superconductivity at 0.93K.[22] The structure of this perovskite compound is almost identical to the cuprate cousin $La_2CuO_4$ with Ruthenium in place of Copper. The low $T_c$ compared with cuprates suggests the importance of copper although not a prerequisite for superconductivity in perovskite. One other notable difference is that the parent $Sr_2RuO_4$ is metallic in contrast to the anti-ferromagnetic Mott insulating parent state of cuprates. $Sr_2RuO_4$ is a chiral $p$-wave triplet superconductor[23] with broken time-reversal symmetry as revealed by muon-spin resonance ($\mu$SR).[24]

### $MgB_2$

The superconductivity of the long-known material magnesium diboride with $T_c$=39K was first reported in 2001.[25] Believed to be phonon-mediated,[26] this multi-band superconductor has two order parameters of different strength associated with $\sigma$ and $\pi$ electrons.[27] $MgB_2$ is thus an unconventional superconductor because BCS theory predicts all paired electrons are 'phase-locked' into a single condensate wavefunction.

### Iron-based superconductors

As in heavy fermion material, iron was avoided in synthesizing superconductors due to its strong ferromagnetic character. So it came as surprise when iron-based superconductivity was first discovered in fluorine-doped $LaFeAsO_{1-x}F_x$ by Hideo Hosono in 2008.[28] There are many variants containing pnictogen (N, P, As, Sb, Bi) or chalcogen (O, Se, S, Te) in 11 / 111 / 122 / 1111 composition; they all share common features such as doping-dependent $T_c$ variation and quasi-2D electronic states resembling cuprates. On the other hand, they are multi-band material with both electron- and hole-like bands, at the same time their parent

compounds are metallic, in sharp contrast to the cuprates. Fe-based superconductors are therefore of very high importance not only on its own, but also as a reference in cuprates study. The breathtaking expansion of this field during the last few years is a sign of the enormous interest on the iron-based superconductivity. One of the most recent and comprehensible series of reviews can be found in the Dec 2011 issue of *Reports of Progress in Physics.*[29]

### 1.2.2 Brief history of cuprates

Despite earlier materials defying BCS-Eliashberg framework, it was copper-based compounds that finally raised $T_c$ above liquid nitrogen temperature (77K), truly opening the realm of high-temperature superconductivity. $T_c$ of the very first group of materials $La_{2-x}Ba_x CuO_4$ (Apr 1986)[30] and $La_{2-x}Sr_xCuO_4$ (late 1986)[31,32] were thirties, but the immediate next Yittrium family $(Y_{1-x}Ba_x)_2CuO_{4-\delta}$ (Jan 1987) synthesized in less than a year hit $T_c$=93K.[33] The discovery of the long-sought dream material awarded the initial discoverers Johannes Georg Bednorz and Karl Alex Müller of IBM at Zurich 1987 Nobel prize in physics, the fastest winning record of which signifies the immense surprise of and its profound influence on the world.

$T_c$ was further raised with accompanying families: 105K with $Bi_2Sr_2CaCu_2O_x$ (Dec 1987),[34] 120K with $Tl_2BaCa_{1.5}Cu_3O_{8.5+x}$(1988),[35] 133.5K with $HgBa_2Ca_2Cu_3O_{8+x}$ (1993).[36] These transitions were all observed at ambient pressure; superconducting transition sets in at higher temperatures under higher pressures. The record $T_c$ up to date of 164K is thus measured in the optimally-doped $HgBa_2Ca_2Cu_3O_{8+x}$ at 31GPa (1994).[37]

## 1.3 Cuprates : phenomenology

### 1.3.1 Structure

The defining feature of the *cuprate* compound is the presence of the $CuO_2$ plaquette that gives rise to the superconductivity. Copper atoms form a tetragonal (or nearly so) lattice with oxygen atom in between the nearest-neighbor Cu pairs, and one or more $CuO_2$ plane(s)

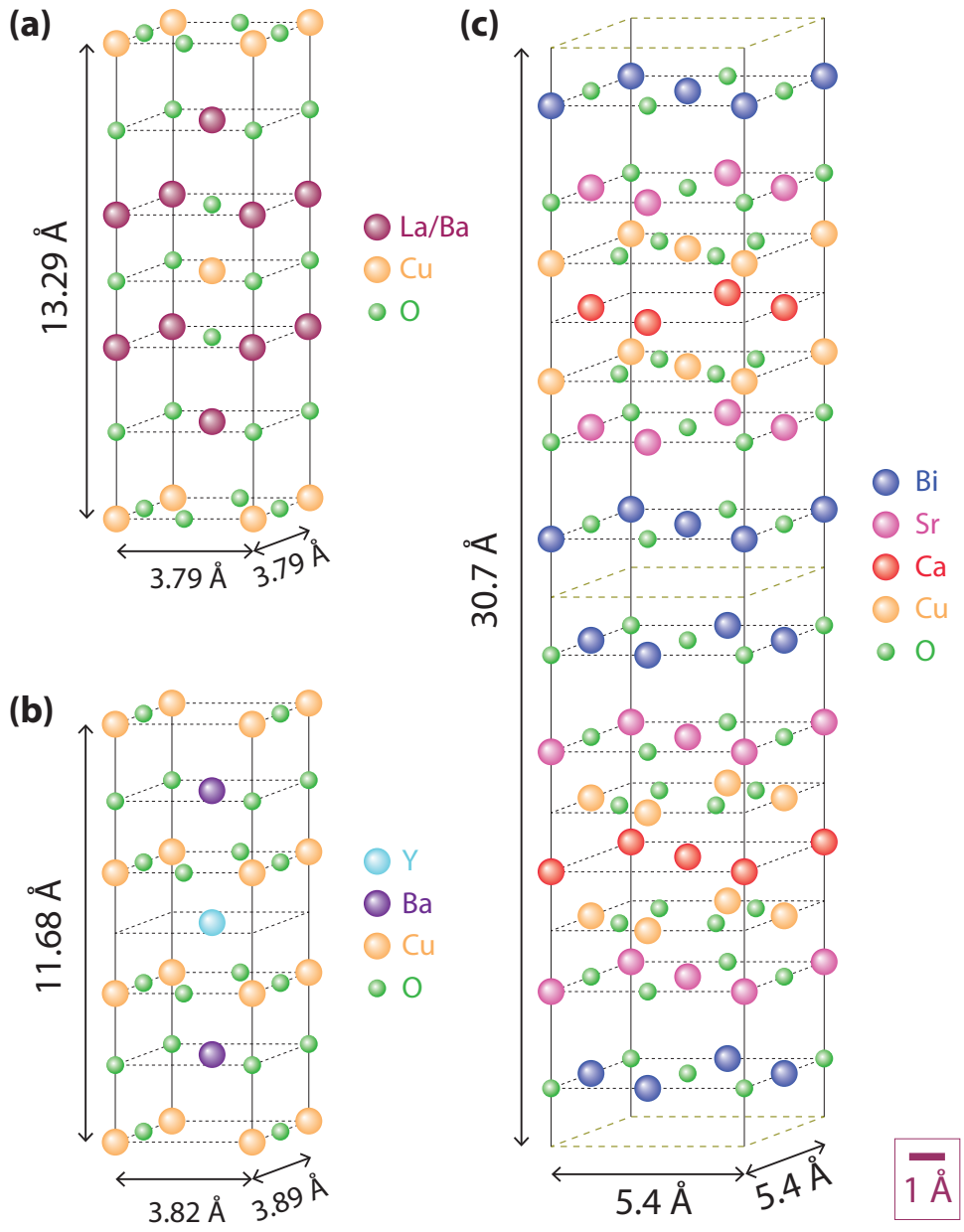


FIGURE 1.3: **Cuprate unit cell.** Unit cell lattice structures of the major cuprate compounds, drawn to scale (1Å scale bar at the bottom right corner) in accordance with the lattice parameters experimentally determined: (a) $(La, Sr/Br)_2CuO_4$[38] (b) $YB_2C_3O_7$[39] (c) $Bi_2Sr_2CaCu_2O_8$.[40] Dashed planes in (c) are the boundary of the half unit cell. These are also the cleaving planes. Buckling structures are not shown.

are covered by mirror-symmetric charge reservoir metallic-oxide layers as shown in Fig. 1.3. Four in-plane and two apical oxygen atoms surrounding a Cu atom form an octahedra in a single-layered family, while multi-layered ones have sparsely populated Y or Ca layers separating $CuO_2$ planes (see Shimizu *et al.*[41] for example). $T_c$ grows with increasing number ($n$) of $CuO_2$ layer, but synthesis of cuprate with $n > 3$ is known to be very difficult. Quasi-2D nature of the electronic wavefunctions results in the strong anisotropy in transport properties between in-plane and out-of-plane values, with anisotropy factor $\gamma$ ranging from as low as ∼10 for YBCO[42] to over 1000 for Bi2212.[43]

### 1.3.2 Comparison with conventional superconductivity

Cuprate is in many respect fundamentally different from conventional superconducting material as will be discussed below. However, as a superconductor, it has a number of characteristics that can be directly compared on the same footing with the low-$T_c$ counterpart. At first, cuprate HTS is a strong type-II superconductor. The upper critical field ($H_{c2}$) is estimated to be very high in the underdoped regime,[44] beyond the present record of ∼100T pulsed magnetic field in Los Alamos.[45]

Second, the coherence length $\xi$ is extremely small and the penetration depth $\lambda$ is very large even when compared with other type-II materials. For example, $\xi_{ab}$=14Å, $\xi_c$=1.5Å, $\lambda_{ab}$=1400Å, $\lambda_c$=7000Å for $YB_2C_3O_7$.[46] Short coherence length, much less than the electron's mean-free path (100-200Å), and comparable to the order of unit-cell dimension, is the primary culprit of the granular real-space structure along with the strong phase-fluctuation (to be discussed in Chapter 5). On the other hand, long penetration depth implies extremely small superfluid density[47]

$$\rho_s(T) \equiv \lambda_{ab}(T)^{-2} = \mu_0 \frac{e^2 n_s}{m^*},$$

where $n_s$ is the superconducting carrier density and $m^*$ their effective mass. Higher $T_c$ with smaller $\xi$ and $\rho_s$ than the conventional superconductivity is another factor that complicates understanding the HTS.

One other deviation of cuprate from BCS framework is found in the ratio $\Delta/k_BT_c$ ($2\Delta \equiv$ superconducting gap). The ratio being greater than 3.54 as predicted by BCS can be explained with the strong-coupling theory, but non-constancy of the ratio cannot. In fact,

$\Delta/k_BT_c$ is very high in the lightly-doped side, gradually falling with increasing doping. Even worse, $\Delta$ for HTS can't be defined conveniently in one single parameter like in BCS theory because of the anisotropic superconducting gap structure (to be discussed below). Consequently HTS demands a substantially different approach.

### 1.3.3 Carrier-doped charge-transfer insulator

One major complication into the understanding of the high-temperature superconductivity is that their undoped parent compound is an anti-ferromagnetic insulator, contrary to the conventional superconductors in which Cooper pairs form out of metallic Fermi liquid sea of dressed Landau quasiparticles. In fact, copper oxide was hardly conceived of as a candidate HTS in BCS picture.

Carrier conduction in band insulators is prohibited by the band structure; available low-energy density of states are absent because the conduction band bottom lies well above and the valence band top well below the Fermi energy. Undoped transition metal oxides are insulators even though $E_F$ is within the half-filled conduction band. Large on-site Coulomb repulsion energy ($U$) prohibits carrier hopping into double occupancy as described by the Hubbard Hamiltonian[48]

$$H = -t \sum_{<ij>\sigma} (c^{\dagger}_{i\sigma} c_{j\sigma} + h.c.) + U \sum_{i} n_{i\uparrow} n_{i\downarrow}.$$

The first term represents energy gain owing to the carrier delocalization by inter-atomic hopping over nearest-neighbor sites, while the second represents the energy cost of site sharing. $t$ is order of 1/10eV, while $U$ ranges a few eV so that $U \gg t$.

The actual insulating gap size, or the minimum excitation energy can be smaller than $U$ in case oxygen band lies between the upper and the lower Hubbard band separated by $U$ as in Cuprates or Manganites. Because the charge transfer between oxygen and copper atoms involves smaller energy($\Delta$), cuprates are charge-transfer type insulator rather than Mott-Hubbard type in which $U$ is smaller than $\Delta$. Hybridization between copper $3d$ and oxygen

$2p$ orbital further splits the oxygen band into Zhang-Rice singlet bound state[49] and non-bonding state in Fig. 1.4. The inter-band transition observed with optical measurements[50] corresponds to process A in the figure. $U$ is about 8eV, and $\Delta$ is 1.5∼2eV for cuprates.[51]

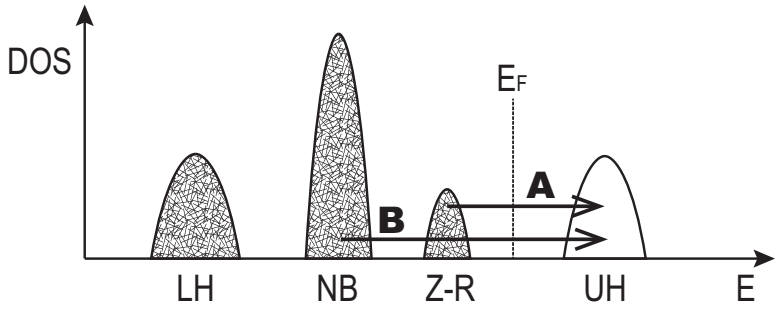


FIGURE 1.4: **Cuprate, a charge transfer insulator.** Insulating energy scale of cuprate is governed by the Cu-O charge transfer. As the oxygen $2p$ band splits off into non-bonding(NB) band and Zhang-Rice(Z-R) singlet bound states due to $3d$-$2p$ orbital hybridization, the lowest-energy charge transfer excitation corresponds to the interband transition from Z-R to Upper Hubbard (UH) band (process A). Illustration reproduced from Mizuno *et al.*[52]

Removing or adding electrons on the half-filled $CuO_2$ plane by doping introduces poor but finite conductivity of non-Fermi-liquid behavior. Hole-doping can be achieved either by substituting $La^{3+}$ in $La_2CuO_4$ with elements of 2+ valence such as Ba or Sr, or by increasing oxygen concentration in YBCO or BSCCO. The former injects less electron into, and the latter pulls electron out of the plane. In YBCO, the oxygen occupation along the CuO chain changes while additional oxygen in BSCCO stays in interstitial locations.[53] Electron-doped compounds have chemical composition $R_{2-x}M_xCuO_4$, where tetravalent (+4) M (Ce or Th) substitutes trivalent (+3) R (rare-earth element such as La, Nd, Pr, Sm or Eu).[54]

Superconductivity eventually arises when the doping level is increased beyond a threshold value. $T_c$ increases on further doping until optimum carrier concentration, and then drops back to zero in the *over*-doping regime. The doping($p$)-temperature($T$) phase diagram common to both hole- and electron-doped cuprates can be summarized as in Fig. 1.5. Antiferromagnetic insulator below Néel temperature $T_N$ near zero doping develops poor conducting states with increasing doping, evolving into normal Fermi liquid past intermediate strange-metal of linear DC resistivity.[56] $T^*$ associated with the onset of the pseudogap drops to zero

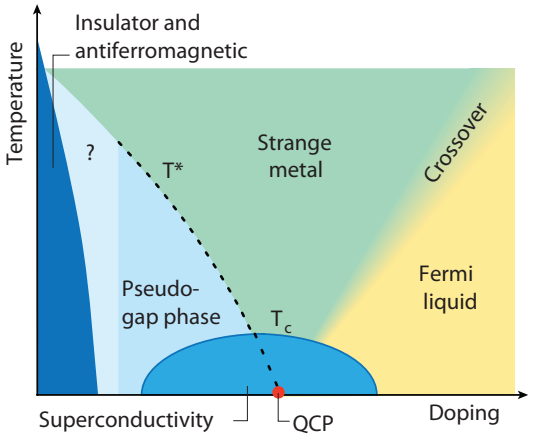


FIGURE 1.5: **$p$-$T$ phase diagram of cuprate.** Cuprate phase diagram in doping ($p$) vs. temperature ($T$) space.[55] Here the carrier concentration is the tuning parameter for the quantum phase transition near the optimal doping. Note that the precise location of the pseudogap boundary is not agreed upon among researchers.

at the quantum critical point (QCP)[1] about which the superconductivity dome appears. The $T_c(p)$ curve empirically falls on a universal equation $T_c = T_{\max}[1-82.6(0.16-p)^2]$ with 0.16 being the optimal doping.[58] LBCO and LSCO exhibits an additional dip on the dome near $p = 1/8$, corresponding to the development of the spin-charge 'stripe' order.[59]

### 1.3.4 d-wave order parameter

One of the crucial information required in establishing a correct theory of pairing mechanism is the symmetry of the condensate wavefunction. First, depending on the spin arrangement of paired electrons, the order parameter(OP) can assume either triplet (total spin S=1) or singlet (S=0) symmetry. The latter is classified into $d$-wave or $s$-wave type by the outcome of the 90-degree rotation: $d$-wave if the sign flips, and $s$-wave otherwise. Each type can be further divided into subgroup including (1) isotropic $s$-wave (constant magnitude in all $k$-direction) (2) anisotropic $s$-wave (azimuthal magnitude variation with four-fold symmetry) (3) $d_{x^2-y^2}$ (+/− lobes along x/y direction) (4) $d_{xy}$ (+/− lobes at 45° to x/y direction).

[1]The exact locus and termination point of $T^*$ curve is controversial. There are other possibility in favor of $T^*$ merging with superconducting dome, which is consistent with precursor picture of pseudogap. See Figure 9 of Norman *et al.*,[57] for example.

OP symmetry of the Fe-based superconductors are still under debate,[60] whereas the $d$-wave gap structure of the cuprate compound is generally accepted now.

The superconducting gap symmetry can be probed with numerous experimental probes. For example, the symmetry can be determined from the tunneling conductance spectra near the Fermi energy since the presence of node in the gap (zero magnitude) will give V-shaped profile associated with low-energy excitations instead of U-shape.[61] Or ARPES can directly trace the gap magnitude variation over the entire Brillouin zone.[62] Still other tools such as angle-resolved specific heat[63] and penetration depth measurement[64] can map the **k**-dependence of the superconducting gap.

But all these probes measure the *magnitude* of the gap only. In other words, the existence of the node alone can't tell if the OP changes sign near the node or not. A phase-sensitive superconducting quantum interference device (SQUID) measurement is one definitive way to distinguish between $s$-wave and $d$-wave scenario. In DC-SQUID magnetometry, spontaneous screening current circulates the loop such that the net magnetic flux (due to the external field plus field associated with the screening current) is adjusted to an integer multiple of the flux quantum. As a result, total supercurrent undergoes periodic modulation with applied field, whose phase is determined by the OP symmetry as well as the SQUID geometry.

Of particular importance is the phase at zero applied field since 'corner' junction is expected to give supercurrent maxima for $s$-wave and minima for $d$-wave gap. Using double contact corner configurations fabricated with YBCO-Au-Pb film SNS (Superconductor - Normal metal - Superconductor) junction, Dale Van Harlingen has demonstrated that the latter is the case, at the same time showing that the phase shift extrapolates to finite value for vanishing bias current limit with single contact corner geometry, both of which are direct evidences of $d_{x^2-y^2}$ pairing symmetry.[65]

Tsuei and Kirtley at IBM obtained the same conclusion with $\pi$-ring tri-crystal magnetometry.[66] When cuprate is epitaxially grown on $SrTiO_3$ substrate and patterned into a ring, half-flux quantum can be spontaneously generated if the ring is located on a junction of three crystals with special orientation and cuprate assumes $d$-wave pairing symmetry. In contrast, those located at a boundary of two crystals or entirely within a single crystal shows integer flux quantization. Even further, they were able to visualize the spontaneous half-flux quantum in the absence of external field with scanning SQUID microscopy.[67]

## 1.4 Cuprates compounds

### 1.4.1 Hole-doped family

#### La-(B/S)CO

(La, Ba/Sr)$_2$CuO$_4$ is an important compound not only as the HTS initiator. LBCO/LSCO develops peculiar static charge/spin density wave texture near $p$=0.125 which is more important because the static stripe suppresses $T_c$[59] (so-called 1/8-anomaly). Dynamic version of the stripe phase are also investigated both theoretically[68] and experimentally,[69] but its role for and relation with the superconductivity is still under debate. Another unique feature of LBCO/LSCO is that they undergo structural phase transition from high-temperature tetragonal (HTT) to low-temperature orthorhombic (LTO) to low-temperature tetragonal (LTT) phase upon cooling.[70] LBCO/LSCO are very hard materials so that they can be synthesized into very large single crystal but hardly cleaves. Thus La-based cuprates are good for scattering experiments but bad for ARPES / STM.[71] LSCO allows access to wide doping range.[72]

#### Y-BCO

$YBa_2Cu_3O_{6+x}$ (Y123) unit cell contains 1D CuO chains along with 2D $CuO_2$ planes (see Fig. 1.3 (b)). The presence of the out-of-plane copper structure influences the crystals in a number of ways. First, increasing oxygen concentration ($x$) in the chain layer distorts YBCO crystal from tetragonal to orthorhombic. In addition the non-uniform local a-b axes anisotropy introduces twinning, which can be removed ('detwinned') with external pressure. Second, the chain layer is also the charge reservoir layer to the $CuO_2$ plane whose oxygen content determines the doping level of the plane.[73] YBCO is thus very unique in that the hole concentration can be adjusted without foreign element. In fact, stoichiometric ortho-I (chain oxygen half-filled, $x$=0.5) and ortho-II (fully occupied, $x$=1) phases are doped but chemically highly homogeneous compounds. The observation of quantum oscillation[74] was also made possible by the extremely high-purity of ortho-I YBCO.

### Bi-SCCO

BSCCO is the most widely studied material with surface-sensitive probes including ARPES and STM, as it is weak and easily cleaves to expose atomically flat BiO layers. For the same reason, obtaining a BSCCO crystal of sufficiently large volume required for X-ray and neutron scattering is very hard. Limited number of scattering data are thus available for BSCCO.[75] Incommensurate supermodulation along bond diagonal direction[76] is one complicating factor. The modulation disappears if Bi atoms are partially substituted with Pb.[77] Bilayer splitting of the anti-nodal electronic structure into bonding and anti-bonding band in overdoped double-layer family[78] can be avoided using single-layer compounds.

### Tl-BCCO

Thallium-based cuprate series $Tl_2Ba_2Ca_{n-1}Cu_nO_{4+2n+\delta}$ is the best material for studying overdoped regime, as the $T_c$ drops from 90 to below 4K by adding oxygen. This is in good contrast with BSCCO for which overdoping is hard to achieve so that minimum accessible $T_c$ of double-layer compound is only about 55K.[79] Resistivity is shown to evolve from non-Fermi-liquid behavior of linear temperature dependence near optimal doping to square variation characteristic of normal metal in overdoping.[80] Full closed Fermi surface of overdoped cuprate was confirmed with quantum oscillation of dHvA effect in this compound, too.[81]

### Hg-BCCO

Mercury-based compounds $Hg_2Ba_2Ca_{n-1}Cu_nO_{4+2n+\delta}$ is a model HTS of the highest $T_c$, or the strongest superconductivity. Single-layered family $HgBa_2CuO_{4+\delta}$ (Hg1201) is particularly important not only because the $T_{c,\max} = 90K$ is way higher than any other single-layer compound ($T_{c,\max}$ of Bi2201 is under 40K, for example), but also because the tetragonal structure is simpler than other cuprates. Large single-crystal Hg1201 recently became available for neutron scattering study, to reveal a magnetic-order signature of pseudogap in underdoped regime.[82]

### Na-CCOC

Sodium-doped cupric oxy-chloride $Ca_{2-x}Na_xCuO_2Cl_2$ ($T_{c,\max}$=28K), iso-structural to LSCO / LBCO of $K_2NiF_4$ type,[83] has apical oxygen replaced by Chlorine.[84] Na-CCOC can be very

lightly hole-doped all the way to the undoped parent compound $Ca_2CuO_2Cl_2$.[85] Combined with easy cleaving to expose as nice flat surface as BSCCO, Na-CCOC offers an exclusive opportunity to investigate with STM the emergence of the pseudogap state from Mott insulator,[86] electronic cluster glass (ECG) state,[87] and 'checker-board' modulation[88] (to be discussed in Chapter 6).

### 1.4.2 Electron-doped family

Although the majority of the cuprate study over the last 25+ years was carried out with $p$-type superconductors in which electrons are pulled out of the $CuO_2$ planes, less-studied $n$-type cuprate with electron concentration exceeding half-filling also provides valuable insights from the inverse side of the phase diagram. Akimitsu *et al.* synthesized the first electron-doped cuprates $Nd_{2-x-y}Sr_xCe_yCuO_4$ in 1989.[89]

$n$-type cuprates have similar phase diagram as $p$-type counterparts (Fig. 1.5) in that AFM Mott-insulator develops superconductivity with increasing electron doping level. But $n$-type material has AFM regime reaching farther, overlapping with the onset of the superconducting phase[90] which is shifted toward lower doping ($p \sim 0.09$)[91] compared with hole-doped compounds($p \sim 0.16$). The proximity of the AFM and SC phase invoked investigations into the role of spin fluctuation[92] and spin excitation[93] in pairing mechanism.

# Chapter 2

# Pseudogap and probes

Since the early stage of 26 years of HTS history, the *pseudo*-gap observed in the intermediate doping-temperature range has been a truly mysterious and elusive phenomena. The temperature below which the pseudogap appears, commonly denoted by $T^*$, are not still completely agreed upon among experimental probes, let alone the underlying mechanism. Even whether it is a friend or a foe of superconductivity[57] is under intense debate to date. As a starting point, this chapter surveys diverse experimental probes, with particular emphasis on what they *see* and how they contribute to our understanding of the pseudogap.

## 2.1 Nuclear Magnetic Resonance (NMR)

NMR refers to a resonant absorption of electromagnetic field when the frequency matches the energy difference between nuclear spin states. In the presence of strong static magnetic field, degenerate energy levels of nuclei with non-zero spin $\boldsymbol{I}$ Zeeman-split into $(2\boldsymbol{I}+1)$ evenly-spaced magnetic sub-levels with separation proportional to the field. When a weak electromagnetic field perpendicular to the static B-field is applied (Fig. 2.1), it is strongly absorbed when the photon energy $h\nu$ is close to the level separation of a particular atom because the incident wave induces transition between adjacent states. In a real material, unlike isolated atom, the nuclear spin interacts with the surrounding environment; their response to the combination of external fields thus reveal underlying modes/structures that couple

to the nuclear spin. In fact, NMR was the first probe to discover pseudogap phenomena in underdoped YBCO.[94]

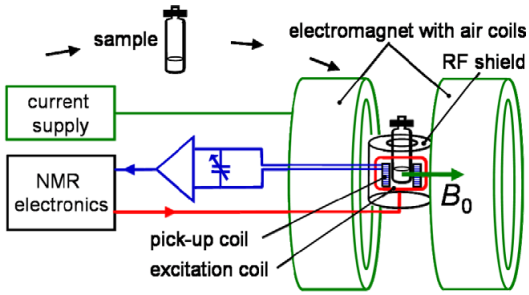


FIGURE 2.1: **NMR experimental setup**.[95] Strong static magnetic field by Helmholtz coil Zeeman-splits nuclear spin states. Excitation field induces transition between the split states, and the resulting Larmor precession of the spins are detected with the pickup coil.

Temporal response of the nuclear spin is governed by two relaxation processes. The first, spin-lattice relaxation, is associated with the evolution of the (volume-integrated) longitudinal magnetization toward $\mathbf{M}_0$ at thermal equilibrium. Once the static magnetic field $\mathbf{B}_0$ is turned on the energy levels split depending on the nuclear spin state. According to the Boltzmann statistics at finite temperature, the lower-energy states will have higher population than the higher-energy states. The imbalance of the spin states effectively lowers total magnetic energy $\sum(-\mathbf{m}\cdot\mathbf{B})$ of the spin system, giving rise to the net magnetization parallel to the level-splitting field which is zero in the absence of field. The speed of this balance-breaking energy-reduction process and the growth of the longitudinal magnetization depends on the energy exchange efficiency between the spin system and the lattice. In the case of cuprate HTS, the spin-lattice relaxation rate $1/\mathrm{T}_1$ of the $^{63}$Cu nucleus is greatly enhanced by the antiferromagnetic spin fluctuations. More formally, the spin-relaxation rate is related to the imaginary part of the susceptibility through[96]

$$\frac{1}{T_1} = \frac{k_B T}{4\mu_B^2 \hbar^2} \sum_{\mathbf{q}} |F(\mathbf{q})|^2 \frac{\chi''(\omega)}{\omega}$$

where $F(\mathbf{q})$ denotes nuclear form factor.

The spin-lattice relaxation can be observed with static magnetic field (let's say, along $\hat{\mathbf{z}}$) alone. In contrast, measurement of the spin-spin relaxation requires alignment of the nuclear spin components transverse to the static field, which can be achieved with magnetic field perpendicular to the Zeeman-splitting field. In a typical spin-echo experiment, a perpendicular pulsed magnetic field $\mathbf{B}_1$ with prescribed duration (a few $\mu$S) is applied to tip over the equilibrium $\mathbf{M}_0$ onto the xy-plane. The longitudinal component returns to $\mathbf{M}_0$ through spin-lattice relaxation once $\mathbf{B}_1$ is turned off, and the transverse component will precess about $\hat{\mathbf{z}}$. The precession frequency will be determined by the magnetic field at the individual atomic sites, in which spatial variation of the magnetic field intrinsic to the material is superposed onto the uniform $\mathbf{B}_0$. Each spin will precess at slightly different frequencies; the coherence of the precession phase gradually disappears, diminishing the net transverse magnetization. The amplitude decay gives the time scale $T_2$ for the spin-spin relaxation. $T_2$ can be deduced from the width of Lorentzian lineshape, as the Fourier transform of a decaying sinusoidal function is Lorentzian; the decay rate T in time domain translates to FWHM $(\pi T)^{-1}$ in frequency domain. The pulsed field may be replaced by a continuous sinusoidal driving signal as the decaying dynamics is independent of the driving signal. $T_2$ is related with the real part of the susceptibility.

One special case of $\chi'(\mathbf{q} = 0, \omega)$ corresponds to the Knight shift($K_s$), which refers to the resonance frequency shift due to the internal magnetic field. This effect will be maximum when the local field on all atoms of the same kind are the identical, therefore reflected onto the spatially-uniform component of $\chi'$.

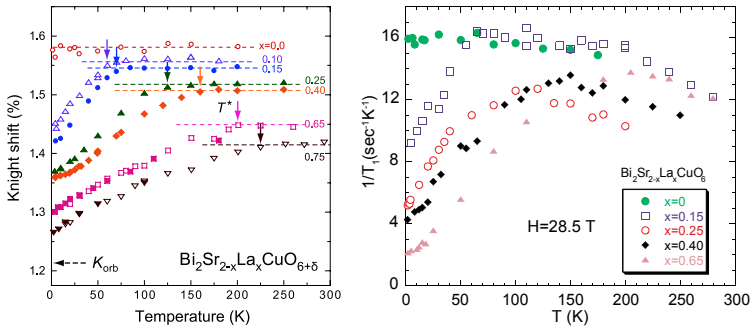


FIGURE 2.2: **Pseudogap by NMR.** (left) Pseudogap set-in temperature clearly decreases, and (right) Spin-lattice relaxation rate starts to decrease at lower temperatures with increasing doping (decrasing La concentration $x$).

According to the Korringa law, $K_s$ is proportional to the density of states at the chemical potential within the Fermi liquid picture.[97] Development of pseudogap, which is signaled by the suppression of the coherent quasiparticle spectral weight, should thus reduce the amount of $K_s$ at temperature above $T_c$. Decreasing $K_s$ below $T^*$ and decreasing $T^*$ with increasing doping is evident in the $^{63,65}$Cu NMR data on La-Bi2201[98] as shown on the left panel in Fig 2.2. On the right side the spin-lattice relaxation rate of the same material is shown to start decreasing at temperatures scaling with $T^*$.[99]

## 2.2 Electronic specific heat

Entropy and specific heat are key fundamental thermodynamic quantities as they are measure of the internal degree of freedom summed over all excitation modes. Phonon and electron contributions are of particular interest, but it is a delicate task to separate electronic component because the phonon dominates the spectra particularly at higher temperatures. Loram *et al.* extracted electronic specific heat of YBCO up to room temperature with high-resolution differential technique between doped and 7% Zn-substituted nearly-undoped samples.[100]

The temperature variation of the electronic specific heat is distinct between overdoped and underdoped regime as in Fig. 2.3 (a) and (b). In overdoped side, the high-temperature values are flat and independent of doping. In addition, the peak temperatures follow $T_c$ and $\Delta\gamma(T_c)$ jump grows toward optimal doping ($\delta$=0.32). In underdoped side, on the contrary, $\gamma$ starts to decrease above $T_c$ signaling the onset of the pseudogap. $\Delta\gamma(T_c)$ rapidly vanishes while $T_c$ doesn't change much near optimal doping, implying faster decay of condensation energy U(0) ($\propto \Delta\gamma(T_c) \cdot T_c^2$) with decreasing doping than the reduction of $T_c$. One other feature to note is the critical doping for which $\gamma(T)$ depressions set-in is slightly higher than the doping for the highest $T_c$.

Similar variations are observed in two other major cuprate family BSCCO and LSCO as in Figure 2.3 (c) and (d), respectively, except for the observation that the critical doping of LSCO is greater than YBCO and BSCCO. In other words, the pseudogap extends farther into the overdoped regime in LSCO.

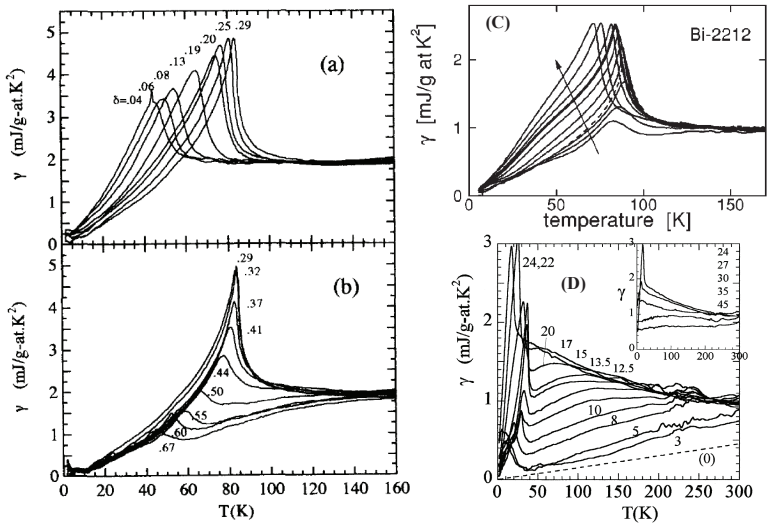


FIGURE 2.3: **Temperature variations of the specific heat coefficients $\gamma$.** (a) overdoped (b) underdoped $Y_{0.8}Ca_{0.2}Ba_2Cu_3O_{7-\delta}$[101] (c) $Bi_{1.9}Pb_{0.2}Sr_{1.9}CaCu_2O_{8+\delta}$ for $0.13 \leq p \leq 0.23$.[102] Arrow indicates increasing doping, and thick (dashed) curves represent critical (optimal) doping sample. (d) $La_{2-x}Sr_xCuO_4$.[103]

## 2.3 Optical conductivity

Photon in the optical range has wavelength orders of magnitude longer than the lattice spacing and the electron mean free path. Response of a sample to ultra-violet(UV), visible light(VL), infra red(IR), or THz microwave irradiation thus can be primarily understood in terms of electromagnetic (EM) wave and Maxwell equations, particularly when the photon frequency is low so that interband transition is prohibited. In fact, optical conductivity measurement has proved to be successful in investigating charge dynamics.

When free electrons are approximately described by the Drude model

$$m\frac{d\mathbf{v}}{dt} + \frac{m\mathbf{v}}{\tau} = e\mathbf{E}_0 \mathrm{e}^{-i\omega t}$$

in which relaxation time $\tau$ represents damping and the velocity $\mathbf{v}$ has the same time variation $\mathbf{v} = \mathbf{v}_0 \mathrm{e}^{-i\omega t}$, the velocity becomes

$$\mathbf{v}_0 = \frac{e\mathbf{E}_0}{m/\tau - im\omega}.$$

Combined with the definition of the current density $\mathbf{j} = ne\mathbf{v} = \sigma\mathbf{E}$, the complex conductivity is obtained:

$$\sigma = \frac{ne^2\tau}{m(1 - i\omega\tau)}.$$

This formula is valid only when $\tau$ is a constant. By allowing frequency- and temperature-dependence in the relaxation time, the conductivity can be extended into a more general form[104]

$$\sigma(\omega, T) = \frac{1}{4\pi} \frac{\omega_p^2}{1/\tau(\omega, T) - i\omega[1 + \lambda(\omega, T)]},$$

where $1 + \lambda(\omega, T)$ represents mass enhancement due to many-body interaction.

Solving Maxwell's equation gives complex wave number of a plain EM wave (in CGS unit)

$$K = \sqrt{\frac{\epsilon\mu\omega^2}{c^2} + \frac{4\pi i\sigma\mu\omega}{c^2}} = \frac{\omega}{c}\sqrt{\epsilon_\mu}$$

so that the complex dielectric function becomes

$$\epsilon(\omega) = \epsilon_0 + \frac{4\pi i\sigma}{\omega} = (n + ik)^2$$

where $\epsilon_0$ denotes dielectric constant which is a real number.

In actual experiment, $\sigma(\omega, T)$ can be determined from reflectivity measurement with EM wave incident perpendicular to the sample surface

$$\Re = \frac{(1 - n)^2 + k^2}{(1 + n)^2 + k^2}$$

as $n(\omega)$ and $k(\omega)$ are complementary to each other by Kramers-Kronig relation. But this method requires knowledge of either $n$ or $k$ at all frequency. Ellipsometry is an alternative technique, in which linear polarization of incident beam is transformed into elliptical polarization after reflection. As the measurement involves reflection, it is important to have a geometrically flat surface.

Depending on the orientation of reflection geometry and the electric field relative to the lattice, the optical measurement can investigate conductivity either within the $CuO_2$ plane or out-of-plane. Commonly referred to as *ab*-plane (or in-plane) and *c*-axis resistivity, $\rho_{ab}$

and $\rho_c$ reflects the charge dynamics of the nodal metal in the clean-limit and anti-nodal dirty-metal, respectively.

Characteristic features of pseudogap are observed in the DC-resistivity, zero-frequency limit of $\rho_{ab}(\omega, T)$. Unlike the linear temperature dependence with zero intercept over a wide temperature range in optimally doped and overdoped superconductors, $\rho(\omega = 0, T)$ for underdoped $La_{2-x}Sr_xCuO_4$ starts to deviate from the linear behavior toward lower values at around $T^*$ determined by NMR, suggesting that the depression is due to the reduced scattering by antiferromagnetic spin fluctuations with the emergence of spin-gap.[105]

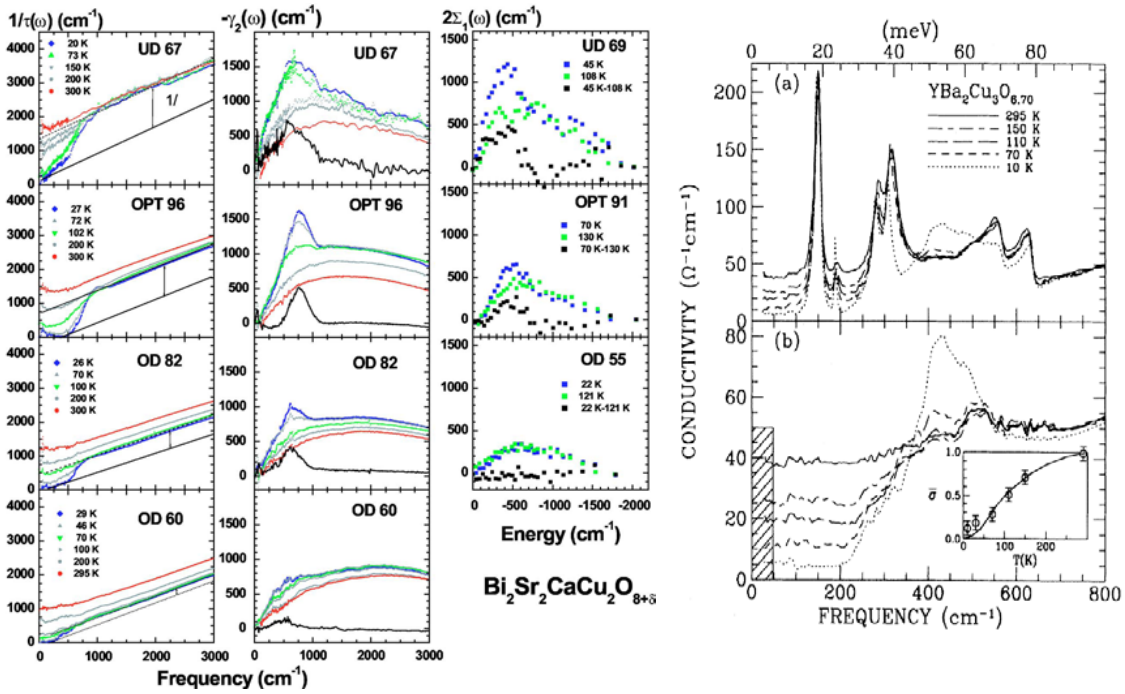


FIGURE 2.4: **In-plane and out-of-plane optical response.** (left, color) In-plane scattering rate and the effective mass. Effective mass enhancements in the second column are compared with ARPES[106] reproduced in the third column (right, black & white) $c$-axis conductivity before and after removing the phonon peaks. In both measurements, $T^*$ can be defined as the temperature where qualitative changes at low frequency sets in.

$1/\tau$ and $1 + \lambda$ can be separated and better resolved in frequency-dependent measurement. As in the left columns of Fig. 2.4, the linear variation of the in-plane scattering rate at room temperature develops gap-like depression and the effective mass increases by a factor of two

up to $\sim$800cm$^{-1}$ ($\sim$100meV), when the temperature is lowered past $T^*$.[107] Interestingly, the mass enhancement is largest at $\sim$500cm$^{-1}$ regardless of doping, closely matching the $\sim$41mV energy scale of magnetic excitation observed in neutron scattering experiment.

$c$-axis resistivity spectra are dominated by strong peaks corresponding to the phonon modes as the charge dynamics strength is relatively low. Electronic contribution to the $c$-axis resistivity is thus better resolved after subtracting the phonon peaks. As shown in the right column of Fig. 2.4, the $c$-axis electronic resistivity is almost flat at room temperature implying incoherent out-of-plane transport. However, upon lowering the temperature below $T^*$, resistivity decreases at low energy range similar to the in-plane component.[108] One thing to note here is that the bandwidth of the pseudogap-like depression doesn't change with temperature, in contrast to the superconducting gap which gradually closes with temperature approaching to $T_c$ from below.

## 2.4 Neutron scattering

As other type of scattering experiments, neutron scattering probes fundamental bulk excitation modes in solids as well as lattice structures. Neutron scattering is unique, however, in that we can study magnetic structures without complication by Coulomb interaction as neutron carries spin but no charge. Moreover, neutron scattering has high energy resolution. It is because the energy of neutron is of meV order for momentum comparable to the lattice spacing, in contrast to X-ray scattering where the photon energy is of 1keV range. One major drawback is that the scattering cross section is small. The target sample must be sufficiently large for substantial intensity of the scattered signal. That was the main reason that the INS experiments were carried out mostly on YBCO and $La_2CuO_4$ systems, with little data on Bi-based system.[109]

Neutron for scattering experiment can be obtained from either nuclear reaction or spallation process. Spontaneous fission of $^{235}$U in research reactor provides continuous stream of neutron beam, while bombarding a high-energy proton on a heavy target such as U, Pb, Hg (spallation) produces pulsed beam. Monochromator (analyzer) selects both the magnitude and direction of momentum $\mathbf{k}$ of incident (scattered) beam. In a typical triple-axis spectrometer, the two selectors as well as the sample can be rotated. (Figure 2.5)

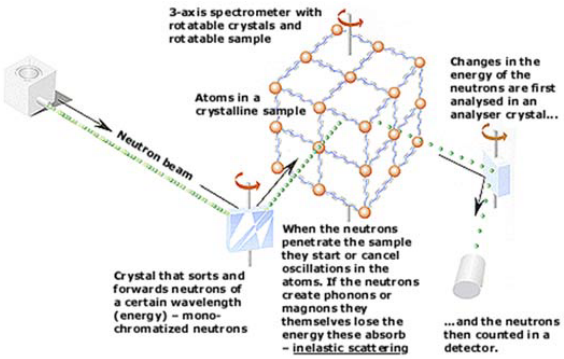


FIGURE 2.5: **Neutron scattering.** Schematic diagram of neutron scattering involving monochromator and analyzer crystal along with 3-axis spectrometer.[110]

Neutron scattering can be considered as a weak perturbation because the energy transfer during inelastic neutron scattering (INS) is small; the incident neutron can induce state transitions of the sample without disturbing the excitation spectrum itself. Thus the differential scattering cross section is determined by three components: (1) incoming neutron flux, (2) transition rate (given by Fermi's Golden Rule), and (3) number of states specified by dE, $d\Omega$, $\mathbf{k}_f$. The scattering cross section reads

$$\frac{d^2\sigma}{d\Omega dE} = \left[\frac{\hbar k_i}{mL^3}\right]^{-1}\left[\frac{2\pi}{\hbar}\left|\langle \mathbf{k}_f, \lambda_f | V | \mathbf{k}_i, \lambda_i \rangle\right|^2\right]\left[\left(\frac{L}{2\pi}\right)^3 \frac{k_f m}{\hbar^2}\right]$$

where $\lambda$ denotes the quantum number of the sample state. Approximating the incoming and outgoing neutrons as plane waves and nuclear potential as delta function reduces the scattering cross section into a simpler form

$$\frac{d^2\sigma}{d\Omega dE} = N\frac{k_f}{k_i} b^2 S(\mathbf{Q}, \omega)$$

in which dynamical structure factor, or the scattering function $S(\mathbf{Q}, \omega)$ is specified as a function of momentum and energy transfer,

$$S(\mathbf{Q}, \omega) = \frac{1}{2\pi\hbar}\iint \frac{1}{N}\sum_{jj'} \delta(\mathbf{r} - (\mathbf{R}_j(t) - \mathbf{R}'_j(t)))e^{i(\mathbf{Q}\cdot\mathbf{r} - \omega t)} d\mathbf{r}dt.$$

This means that $S(\mathbf{Q}, \omega)$ is the Fourier transform of the time-dependent pair correlation

function, and that this quantity reflects the fluctuation inside the sample independent of incident / scattered neutron momenta. In case of coherent atomic magnetic scattering, the spin correlation comes into play in place of the density correlation:

$$S(\mathbf{Q},\omega) = \sum_{\alpha,\beta}(\delta_{\alpha,\beta} - \hat{Q}_\alpha \hat{Q}_\beta)\left[\frac{1}{2\pi}\int e^{-i\omega t}\sum_l e^{i\mathbf{Q}\cdot\mathbf{r}_l}\langle s_0^\alpha(0) s_l^\beta(t)\rangle dt\right]$$

where $\alpha$, $\beta$ refers to the cartesian coordinate indices.

In actual scattering data, broad elastic signal usually extends over a few tens of mV around the zero energy transfer peak contaminating low energy portion of the excitation spectra. One way to attenuate the elastic component is to use polarized neutron. Spin-flip process such as magnetic scattering can be effectively separated from non-flip process such as Bragg diffraction and phonon scattering.

Neutron scattering data are in most cases plotted on energy vs. intensity graph. But the scattering function can be converted into $\chi''(\omega)$ using Fluctuation-Dissipation Theorem (FDT):

$$S(\mathbf{Q},\omega) = \frac{1}{1-e^{-\beta\hbar\omega}}\chi''(\omega).$$

FDT, which relates $S(\mathbf{Q},\omega)$ to the dissipative component of the magnetic response of the system, is based on the assumption that the response of the system to small external perturbation (such as by incident neutron) is the same as that by the spontaneous internal thermal fluctuation. This conversion is particularly helpful when comparing the experimental data with theoretical calculation.

One of the most famous experimental result obtained with neutron scattering in the HTS study is the discovery of the 'stripe' phase in $x$=1/8 hole-doped $La_{1.6-x}Nd_{0.4}Sr_xCuO_4$, in which parallel spinless stripes exist at every 4 Cu-O bond as spin-domain boundary.[59] This is basically elastic neutron scattering, or neutron diffraction measurement involving no energy transfer. But the discovery proved the power of the neutron scattering in understanding magnetic modes underlying HTS.

Another discovery of very high significance is the resonance peak at 41meV and at the antiferromagnetic ordering wavevector ($\pi$,$\pi$) observed on optimally doped $YB_2C_3O_{6+x}$.[111]

The nature and its relation to the superconductivity and/or pseudogap of this resonance peak as well as the '1/8-anomaly' are still under debate.

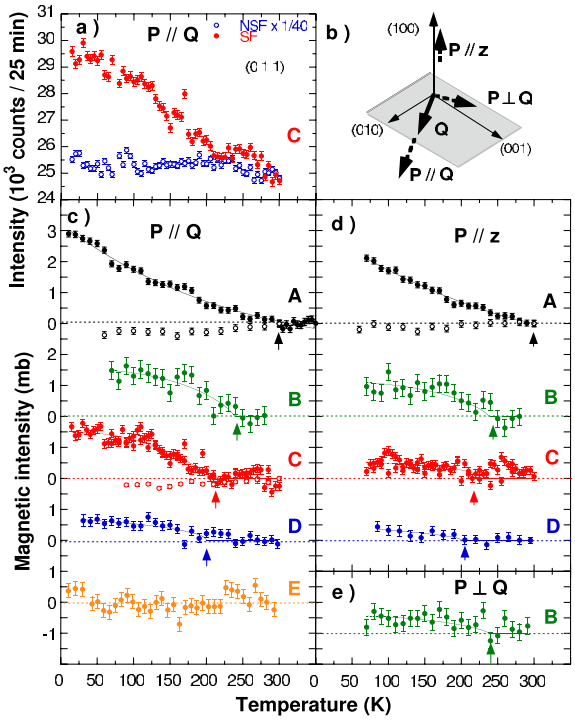


FIGURE 2.6: **Magnetic order in pseudogap phase.** Spin-flip(SF) signal in YBCO starts to deviate from nearly-uniform non-spin-flip(NSF) ones with both polarizations. Arrows indicate the departure temperatures. Doping and $T_c$'s are: A(UD54K) / B(UD61K) / C(UD64K) / D(UD78K) / E(OD75K).

In the context of pseudogap, recent neutron scattering measurements have provided results in favor of the circulating current(CC) phase[112] (Fig. 2.6). Theoretically proposed by Chandra Varma, this ordered phase consists of magnetic moments by rotating currents along O-Cu-O right triangle with alternating orientations in a configuration that translational symmetry is retained. As the magnetic structure has the same periodicity as the underlying $CuO_2$ lattice, neutron diffraction should exhibit peak at the scattering wave vector $\mathbf{Q}$=(1, 0, 1) (or (0, 1, 1), which is equivalent to (1, 0, 1) in tetragonal lattice). But the actual measurement was made only recently because the intensity of the magnetic peak is too weak compared to the Bragg peak, even with spin-polarized neutron. Fauqué *et. al.* observed such unusual 'hidden' magnetic order in underdoped YBCO compound[113] as

the first experimentally confirmed candidate order parameter of the pseudogap. The same magnetic ordering was also observed in the single-layer mercury compound $HgBa_2CuO_{4+\delta}$, [82] where Y. Li *et. al.* further confirmed that the order set-in temperature closely follows $T^*$ by changing the doping by annealing, instead of measuring different samples. These two results suggest that the CC-phase ordering can be a feature common to all hole-doped cuprates, rendering pseudogap as a phase rather than a cross-over phenomenon.

## 2.5 Angle-Resolved Photo-Emission Spectroscopy (ARPES)

ARPES is essentially a momentum-resolved photoelectric effect measurement. Well understood now in terms of particle nature of light and its interaction with matter, photoelectric effect refers to the emission of electron by incident light. ARPES can directly map out the energy-momentum relation of a material as the analyzer can simultaneously resolve both quantities of scattered electrons. Studying 3D materials is complicated as the photo-electron momentum normal to the surface can't be as precisely determined as parallel component. Cuprate HTS, however, do not suffer from this restriction because the material property is determined by the quasi-2D electronic structure on copper oxide planes. As a consequence ARPES has been one of the leading probe in investigating the electronic structure of HTSC for about 20 years.

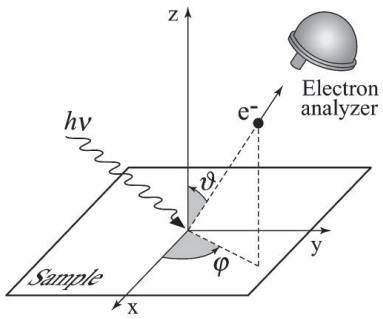


FIGURE 2.7: **ARPES geometry.** Incident photon emits an electron toward a direction defined by $(\vartheta, \varphi)$. Energy and momentum of the scattered electrons are determined by the hemispherical analyzer.

Basic geometry of photoemission process is depicted in Fig. 2.7. Incoming light of energy $h\nu$ emits electrons of kinetic energy $E_{kin} = h\nu - \phi - |E_B|$ into a direction $(\vartheta, \varphi)$, where $\phi$ is the work function of the material and $E_B$ is the biding energy of the electron with respect to the Fermi level. Then the crystal momentum component parallel to the surface is given by[78]

$$\mathbf{p}_{\parallel} = \hbar\mathbf{k}_{\parallel} = \sqrt{2mE_{\text{kin}}} \cdot \sin\vartheta \tag{2.5.1}$$

In quasi-2D material such as cuprate HTSC where $\mathbf{k}_{\perp}$ makes negligible contribution to dispersion, knowledge of the relationship between $\mathbf{k}_{\parallel}$ and $E_{\text{kin}}$ (or equivalently the binding energy) provides direct access to the underlying electronic structure.

Recent ARPES experiments use diverse light sources, including (1) 21.2eV HeI$\alpha$ UV line, (2) photons produced in linear accelerator or synchrotron, and (3) Laser. Synchrotron light source has advantages that the incident photon energy can be varied and that the photon flux is very high which translates to strong photo-electron signal. Due to the requirement of huge facility and limited access, however, Laser is increasingly taking the place. Not only reducing cost and size, coherent Laser light of low photon energy (∼7eV) have provided new results with unprecedented resolutions. One weakness of the Laser-based ARPES is that it cannot probe the antinodal area. Because the available kinetic energy of emitted electron is too small (Eq. 2.5.1).

Emitted electrons are collected and resolved with analyzer. The analyzer is made up of two concentric hemispheres of R∼20cm with applied potential difference. Electrons with specific energy range only could reach the detector and are thus effectively filtered.

ARPES measures the intensity of the emitted electrons which is a product of three factors:

$$I(\mathbf{k}, \omega) = I_0(\mathbf{k}, \nu, \mathbf{A}) f(\omega) A(\mathbf{k}, \omega)$$

$f(\omega)$ is the Fermi-Dirac distribution function, $A(\mathbf{k}, \omega)$ is the spectral weight which represents the probability of adding or removing an electron, and $I_0$ is the matrix element term. $A(\mathbf{k}, \omega)$ is derived from the single particle Green's function $G^{-1}(\mathbf{k}, \omega) = \omega - \epsilon_{\mathbf{k}} - \Sigma(\mathbf{k}, \omega)$ as

$$A(\mathbf{k}, \omega) = -\frac{1}{\pi}\text{Im}G(\mathbf{k}, \omega) = -\frac{1}{\pi}\frac{\Sigma''(\mathbf{k}, \omega)}{[\omega - \epsilon_{\mathbf{k}} - \Sigma'(\mathbf{k}, \omega)]^2 + [\Sigma''(\mathbf{k}, \omega)]^2}$$

where prime and double prime refers to the real and imaginary part of the self-energy $\Sigma(\mathbf{k}, \omega)$, respectively. Real part is evaluated from the difference between the actual dispersion and the expected band structure in the absence of many-body effects; imaginary part is determined from the Lorentzian linewidth of the momentum distribution curve(MDC).

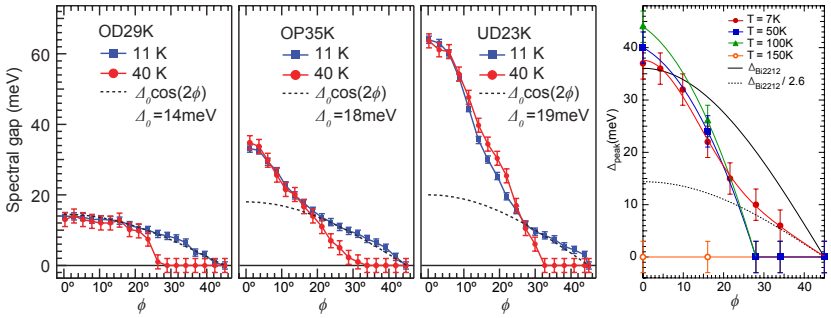


FIGURE 2.8: **Doping dependence and temperature evolution of the gap structure.** Three distinct structures are evident : (1) $\Delta_{SC}(\phi) \sim \cos(2\phi)$ below $T_c$ (2) pseudogap away from the node remains while $\Delta_{SC}$ closes for $T_c < T < T^*$ (3) no gap above $T^*$.

Owing to the unique momentum-resolving capability, ARPES measurement has provided the shape of the anisotropic d-wave superconducting gap in detail from the early days of HTS history.[114] With continual improvement in the instrumental resolution over the last 20 years, recent ARPES experiments are giving consistent pictures about the superconducting gap and pseudogap: (1) $\Delta_{SC}(\mathbf{k}) \sim (\Delta_0/2)(\cos k_x - \cos k_y)$[78] and (2) pseudogap in the antinodal area characterized by disappearance of the coherence peak[115] as shown in Fig. 2.8 and Fig. 2.9.

## 2.6 Raman scattering

Raman scattering is a spectroscopic technique to study low-energy elementary excitation of a lattice, in particular vibrational and rotational modes as well as magnetic modes with sub-meV energy resolution. One of the unique feature of this technique is the capability of investigating symmetrical parts of the Brillouin zone(BZ). This is particularly useful when the governing phenomena come from high-symmetry area as in cuprate HTS.

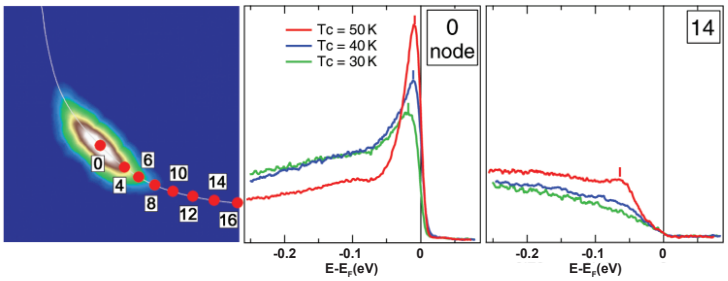


FIGURE 2.9: **coherent nodal vs. incoherent antinodal quasiparticles.** In the underdoped regime, nodal excitations have well-defined coherent peaks while antinodal spectra lose coherence reducing into a broad hump. Energy position of the nodal coherence increases with decreasing doping, showing the evolution of $\Delta_0$.

Electronic Raman spectroscopy (ERS) relies on inelastic scattering of light off a material. Typically Laser with frequency near visible light range illuminates a sample. Interaction of incident light with target sample can either emit(Stokes) or absorb(Anti-Stokes) quasiparticles(QPs) of excitation. Raman scattering is made up of three steps: (1) incident electromagnetic field produces electron-hole pairs (2) the electron-hole pair undergoes a transition in which either electron or hole interacts with elementary excitation (3) recombination of the electron-hole pair creates scattered photon with shifted energy.

The strength of this second-order scattering process is proportional to a quantity known as Raman vertex, $\gamma_k$. The complicated form of $\gamma_k$ can be greatly simplified under the assumptions that (1) photon momentum transferred is negligible compared with BZ and (2) energy difference between the initial and final state is negligible compared with electronic transition involved.[116] On tetragonal lattice structure, Raman vertex for cuprate HTSC can be expressed into the following tensor form,

$$\tilde{\gamma}(k) = \gamma_{A_{1g}}(k) \begin{pmatrix} 1 & 0 \\ 0 & 1 \end{pmatrix} + \gamma_{B_{1g}}(k) \begin{pmatrix} 1 & 0 \\ 0 & -1 \end{pmatrix} + \gamma_{B_{2g}}(k) \begin{pmatrix} 0 & 1 \\ 1 & 0 \end{pmatrix}$$

where the basis vectors are along the Cu-O bond directions. Here the $B_{1g}$ tensor, transforming as $(k_x^2 - k_y^2)$, vanishes along the BZ diagonal thus primarily probing properties along the principal axes of BZ. This component can be picked out with cross polarization of the electric field of incident and scattered light, $\begin{pmatrix} 1 \\ 1 \end{pmatrix}$ and $\begin{pmatrix} 1 \\ -1 \end{pmatrix}$.

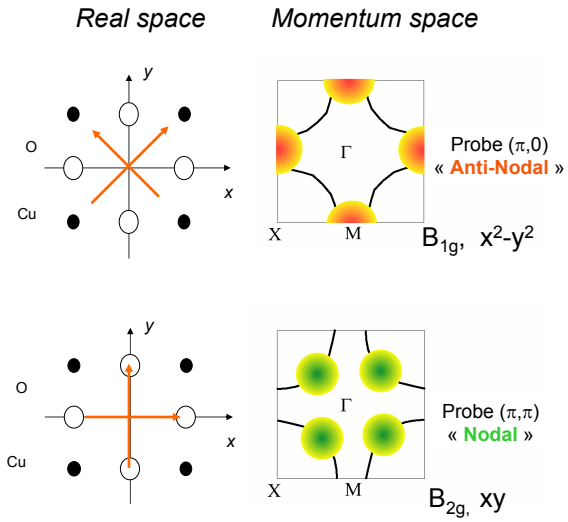


FIGURE 2.10: **Raman scattering geometry.** Red arrows represent the electric field polarization of the incident and scattered electromagnetic wave. Cross combination along (diagonal to) the underlying Cu-O bond direction projects out $B_{1g}$ ($B_{2g}$) channels, probing excitations near the anti-node (node).

Similarly, cross polarization of $\begin{pmatrix} 1 \\ 0 \end{pmatrix}$ and $\begin{pmatrix} 0 \\ 1 \end{pmatrix}$ sorts out $B_{2g}$ component which transforms as $(k_x k_y)$ probing the BZ diagonal. In cuprate material $B_{1g}$ mode is directly related with anti-nodal and $B_{2g}$ with nodal region of the momentum space. The involved geometry in cuprate is summarized in Fig. 2.10. $B_{1g}$ and $B_{2g}$ mode can also be studied with parallel combination of electric field polarization. However both modes are mixed with fully-symmetric $A_{1g}$ channel.

The actual quantity measured by Raman spectroscopy is the dynamical structure factor, which is a Fourier transform of density-density correlation function:[117]

$$S(q,\Omega,T) = \int \frac{dt}{2\pi} e^{i\Omega t} < \hat{\rho}^{\dagger}(q,t)\hat{\rho}(q,0) >_T,$$

where $< ... >_T$ denotes thermal average and the density operator $\hat{\rho}_q$ is given by

$$\hat{\rho}_q = \sum_{n_f,n_i,k} \gamma_{n_f,n_i,k} c^{+}_{n_f,k+q} c_{n_i,k}$$

using the Raman vertex described above. Dissipative (imaginary) part of the response function $\chi''(q, \Omega, T)$ is determined from $S(q, \Omega, T)$ after Bose-Einstein factor correction as in neutron scattering:

$$S(q, \Omega, T) = \frac{\hbar}{\pi}(1 + n(\Omega, T))\chi''(q, \Omega, T).$$

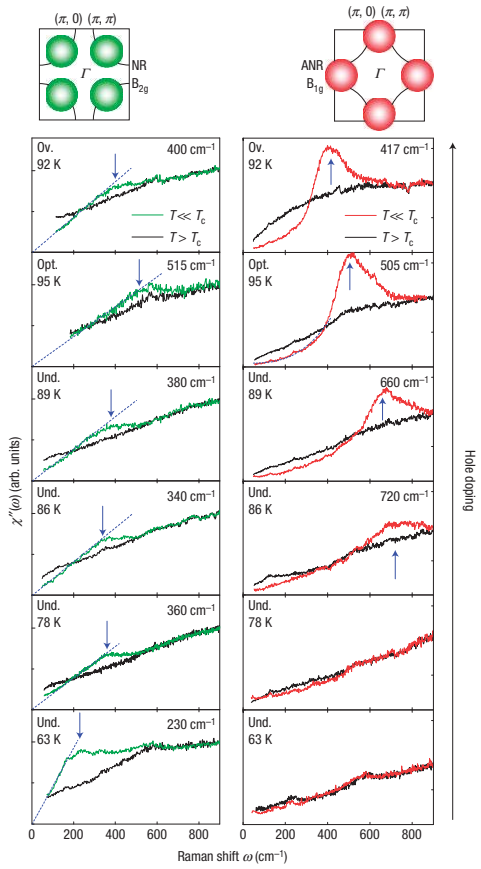


FIGURE 2.11: **Raman responses near the node / antinode.** Raman spectra measured in samples of various doping levels in $B_{2g}$ and $B_{1g}$ channel, at above and below $T_c$ are compared. The blue arrows indicate the energy locations where the difference between the two spectra are maximum.

One example of nodal / antinodal Raman spectra are shown in Fig. 2.11 at different hole-doping levels. The following trends are evident. (1) At low energies nodal excitations below

$T_c$ follow a line passing through origin, while anti-nodal spectra show cubic frequency dependence. (2) Anti-nodal spectra show no significant difference between above and below $T_c$ in underdoped regime, in contrast to nodal spectra retaining the differences. (3) Peak energies of superconducting spectra increase in anti-node as doping is reduced. However, those in nodal spectra increase until optimal doping and decrease in the underdoped samples. (4) For optimal or over-doping the two peak energies are very close.

The anti-nodal excitation spectra are very similar to those of ARPES, in that the coherent quasiparticle peak present in overdoped regime shifts to higher energy gradually losing spectral weight with decreasing doping. One important distinction from ARPES measurement is that the anti-nodal Raman spectra is different above and below $T_c$ in the higher doping side, unlike ARPES spectra that shows no difference over entire doping (compare with Fig. 2.8). But both probes commonly indicate that the superconductivity is either weaker than the pseudogap in the anti-node, which agrees with the observations to be discussed in Chapter 6.

## 2.7 Quantum oscillation

Quantum oscillation generically refers to the oscillatory response of certain physical quantities to magnetic field. This phenomena is observed in many observables which possess strong dependence on the shape and structure of the Fermi surface. Most important of these are the magneto-resistance (Shubnikov-de Haas effect; SdH) and the magnetization (de Haas-van Alphen effect; dHvA). As such, quantum oscillation in fact means that *of resistance* (or *of magnetization*).

The Fermi surface dependence of these quantities can be understood roughly with free electrons in a magnetic field.[118] The energy of free electron in a cubic box of side L has isotropic form,

$$E(k_x, k_y, k_z) = \frac{\hbar^2}{2m}\left(k_x^2 + k_y^2 + k_z^2\right)$$

where discrete **k** values are given by the periodic boundary condition; $k_x = 2\pi n_x/L$, and so on. In the presence of magnetic field (H$\|$z), however, the electrons traverse semi-classical contour in a plane perpendicular to the field and the in-plane energy is quantized in units

of cyclotron frequency:

$$E_\nu(k_z) = \frac{\hbar^2}{2m}k_z^2 + \left(\nu + \frac{1}{2}\right)\hbar\frac{eH}{mc}$$

Here $\nu$ is the index of the quantized Landau level, a very large number allowing the use of the correspondence principle. Then the energy difference between adjacent Landau levels is equal to the frequency of the orbital motion, inverse proportional to the energy derivative of the orbital area, times the Planck constant:

$$E_{\nu+1} - E_\nu = h\left[\frac{\hbar^2 c}{eH}\frac{\partial A}{\partial E}\right]^{-1} \cong \frac{2\pi eH}{\hbar c}\frac{E_{\nu+1} - E_\nu}{A_{\nu+1} - A_\nu}$$

where the last approximation is possible because the energy level difference is tiny compared to the energy itself. Hence the difference of the orbital area between the adjacent Landau levels at large $\nu$ is a constant proportional to the applied field only; or the area should be a discrete function of $\nu$ as in the following famous form by Onsager,

$$A(E_\nu, k_z) = (\nu + \lambda)\Delta A = (\nu + \lambda)\frac{2\pi e}{\hbar c}H$$

where $\lambda$ is a constant independent of $\nu$.

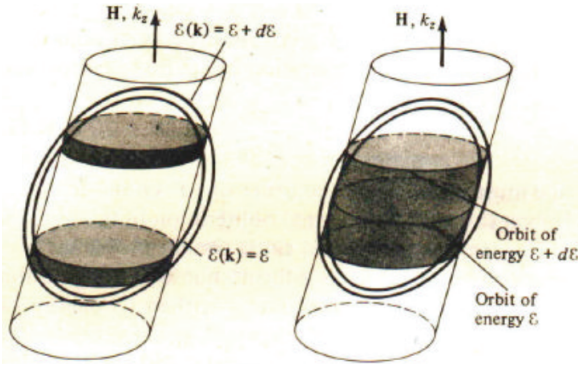


FIGURE 2.12: **Quantum Oscillation.**[118] Increasing the magnetic field expands the radius of the cylindrical shell. FS-dependent signal shows extrema when the portion of the shell intersecting with the Fermi surface shell has extremum volume, because the condition will give maximum available number of **k** space states.

This result implies that the set of the allowed k-space points are reduced from a sphere to a set of concentric cylindrical shells along the field whose cross section areas are given as

above (Fig. 2.12). Each shell is labeled by the index $\nu$, the radii of which increase with the external field. On each individual shell the energy increases with $|k_z|$.

Most electronic properties of materials strongly depend on the density of states (DOS) near the Fermi energy, $D(E_F)$, which is essentially the number of particle states available for the specific process. From the above derivation $D(E_F)$ should be proportional to the volume of the cylindrical shells contained within constant-energy surfaces of energies $E_F$ and $E_F + \delta E$. This volume will be at its extremum value whenever the semi-classical orbits find the extremum contour of the Fermi surface perpendicular to the field. Or, equivalently, the Fermi surface-dependent quantity will give repeated extremum at field intensities satisfying the above relation with constant area. Each peak (or dip) are associated with different $\nu$'s, so for adjacent peaks we find the following formula:

$$\Delta\left(\frac{1}{H}\right) = \frac{2\pi e}{\hbar c}\frac{1}{A(E_F)}.$$

This explains the origin of the oscillatory behavior observed in any quantity that depends on the Fermi surface and the density of state near the Fermi energy. It is also obvious that the oscillation appears in an *inverse* field plot, and that the frequency of oscillation (inverse of 1/H, thus in unit of field) is directly proportional to the area. And multiple oscillation frequencies can be observed on systems whose Fermi surface has multiple extrema, corresponding to each extremum.

As the quantum oscillation is closely associated with the closed Fermi surface pocket(s), the observation of the oscillation is a crucial evidence of the existence of the pocket itself. QO measurement alone, however, can not provide information on the exact position of them. As a consequence theoretical Fermi surface is proposed first and then compared with QO results in most cases.

Practically very strong magnetic fields are required in order to observe QO, because the cylindrical shells will be so close to each other at weak fields that individual peaks can not be resolved. QO behaviors in HTSC are generally observed above 40∼50T which is within the accessible range of the modern high-field equipments that can provide as high as 60T continuous or 100T pulsed magnetic fields.

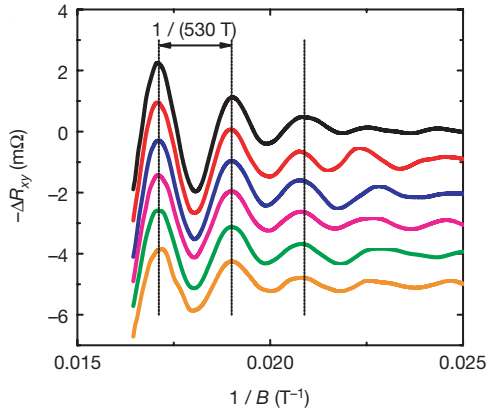


FIGURE 2.13: **Quantum oscillation revealed.** Hall resistance in underdoped YBCO after background subtraction clearly shows oscillation with inverse magnetic field.

In QO measurement, quality of the sample is critical as QO signal is extremely vulnerable to impurity. The seminal observation by Doiron-Leyraud *et al.* in 2007[74] were made possible with ultra-high-purity YBCO grown by researchers in University of British Columbia.[119] They observed oscillatory signal in the magneto-resistivity (SdH effect) of $YB_2C_3O_{6.5}$ above ∼45T at T=2K. In the inverse-field plot, as shown in Fig. 2.13, the period of the oscillation turned out to be 530±20T. This evidences the existence of the closed Fermi surface in the underdoped cuprates which is in stark contrast to the ARPES picture in which broken arc along Fermi surface exists near the node not in closed form. From the Onsager relation the corresponding k-space area was estimated to be as small as $A_k$=5.1nm$^{-2}$. Even more surprisingly, next measurement of the Hall coefficient with increasing temperature revealed sign reversal, implying the emergence of electron-like Fermi pocket out of hole-doped superconductor and subsequent reconstruction of the Fermi surface at low temperatures.[120]

QO signal alone cannot determine the k-space position of the closed Fermi surface. The exact location of the observed Fermi pocket(s) and the possible scenario of their emergence are thus still under debate.[121] In addition, QO signal does not have direct signature of pseudogap either. But the Fermi surface topology below $T_c$ should reflect the pseudogap profile at that temperature (at least according to the ARPES picture of the pseudogap). This is how QO is indirectly related with the understanding of the pseudogap.

## 2.8 Nernst effect

When a conducting sample is subjected to a temperature gradient, the charge carriers tend to diffuse from high to low temperature region due to the kinetic energy difference. Magnetic field applied perpendicular to the direction of their thermal motion will exert Lorentz force, and the accumulation of the deflected carriers will generate electric potential proportional to the thermal gradient and field strength. Being a thermal analogue of the Hall effect, the proportionality constant for this thermo-electro-magnetic effect (Nernst effect) can also be similarly defined as

$$\nu = E_y/(B_z \nabla T_x),$$

where subscripts indicate the orthogonality among $\nabla T$, **B** and **E**.

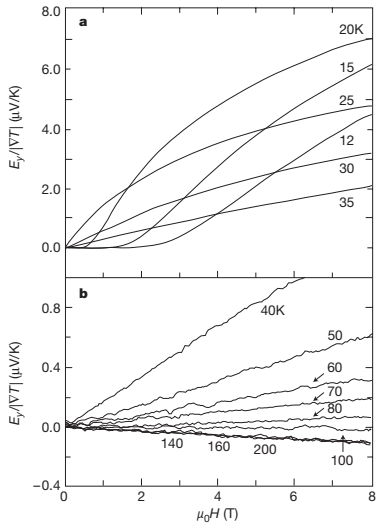


FIGURE 2.14: **Nernst effect measurement.** Hall resistance in underdoped LSCO after background subtraction clearly shows oscillation with inverse magnetic field.

Hole-doped cuprates are type-II superconductors; magnetic field greater than $H_{c1}(T)$ generates magnetic vortices of vanishing diamagnetism. As the induced vortices also diffuse under thermal gradient, the Nernst effect captures the dynamics of this vortex-like excitations as well as those of holes in the normal state. Phuan Ong and his colleagues measured the Nernst signal on underdoped $La_{2-x}Sr_xCuO_4$ at varying temperatures and magnetic fields (Fig. 2.14) to discover two important characteristics.[122] First, the maximum Nernst signal

is very large compared with the normal-state values $\nu_n$. Second, it does not fall to $\nu_n$ right at $T_c$. Substantial fraction of below-$T_c$ value remains above the critical temperature instead, gradually decreasing to the background level with increasing temperatures where the $T_{onset}$ is a few times of $T_c$. These observations imply that distinct vortex-like excitation persists well into the pseudogap regime, supporting the scenario proposed by Emery and Kivelson [123] that $T_c$ is associated with the phase coherence breaking, instead of vanishing superfluid density as in conventional superconductors. In other words, $T_c$ is the temperature where the vortices destroy the long-range phase coherence.

One thing to note is that the $T_{onset}$ is significantly lower than $T^*$ determined by other probes, so that the vortex-like excitation mode is not a direct signature of pseudogap. Nevertheless, Nernst effect measurement is an important probe to investigate the relation between superconductivity and pseudogap. Because the vortex-like excitation exist both above and below $T_c$. Evolution of the Nernst signal across $T_c$ will help find the similarity and/or the difference of the two states.

## 2.9 Other techniques

There are other probes of pseudogap which are measured and reported less frequently. A few of them are listed below.

- Muon spin rotation (uSR)

  When low-energy muons produced from pion decay are implanted into a sample, relaxation dynamics of the muon spin rotation depends on the interaction of the charge / spin of muon and its local environment, much like relaxation in NMR. [124]

- Polar Kerr effect

  Intensity and polarization of light can change upon reflection from a surface with magnetization. Polar Kerr effect is a special case in which the magnetization direction is perpendicular to the surface and in the plane of incidence. Finite Kerr angle, associated with the time-reversal symmetry breaking, is observed in YBCO below a transition temperature $T_s$ which traces $T^*$. [125] Smallness of the Kerr angle ($\sim \mu$rad),

also found in Pb-BSCCO, suggests that the broken symmetry phase may not be the primary order.[126]

- Time-resolved reflectivity

  Temporal evolution of relative reflectivity ($\Delta R/R$) reveals the quasiparticle dynamics. When pulse of energy higher than the superconducting gap energy breaks Cooper pairs into non-equilibrium state of two electrons, their relaxation into the equilibrium (through recombination of the two electrons) occurs on picosecond time scale. Using femto-second resolution perpendicular pump-probe pulses, distinction between the superconducting QP (Cooper pair) and pseudogap QP emerges most notably in the sign changes of the reflectivity. The sign of $\Delta R/R$ immediately after the pump pulse changes from positive (below $T_c$) to negative (between $T_c$ and $T^*$) back to positive (above $T^*$).[127]

# Chapter 3

# STM

The data presented in this thesis were taken with a Low-Temperature Spectroscopic-Imaging Scanning Tunneling Microscope (LT SI-STM). Each component, as contained in the name itself, will be described in the following order: Tunneling(T) - Scanning(S) - Microscope(M) - Spectroscopy(SI) - Cryogenics (LT). The STM used for much of this study was transported from Cornell (STM3) to Brookhaven National Laboratory (BNL STM1) in early 2010. In this chapter the description will be mainly on the technical aspects of BNL STM1 that are distinct from other two STMs. Readers are referred to the dissertations by previous graduate students for details that are in common with other Cornell STMs. [128,129]

## 3.1 Tunneling

### 3.1.1 Basics of electron tunneling

Tunneling of electrons between metal and superconductor was first experimentally realized by Ivar Giaever[130] when he fabricated thin alumina insulating barrier by partial oxidation of aluminum electrode and depositing lead on top which superconducts below $T_c$=7.2K. Instead of solving full Schrödinger equation, Bardeen described the tunneling process with time-dependent perturbation theory[131] where the matrix element M is given by, for electron

tunneling from state $m$ on one side to $n$ on the other side along $\hat{\mathbf{z}}$-direction,

$$M_{mn} = -\frac{\hbar^2}{2m}\oint_S dS\left(\psi_m\frac{\partial\psi_n}{\partial z} - \psi_n\frac{\partial\psi_m}{\partial z}\right)$$

over the surface of constant z that lies completely beyond the insulating barrier. The rate of electron transfer can be determined from the Fermi golden rule

$$w = \frac{2\pi}{\hbar}|M_{mn}|^2$$

in which elastic tunneling is implied.

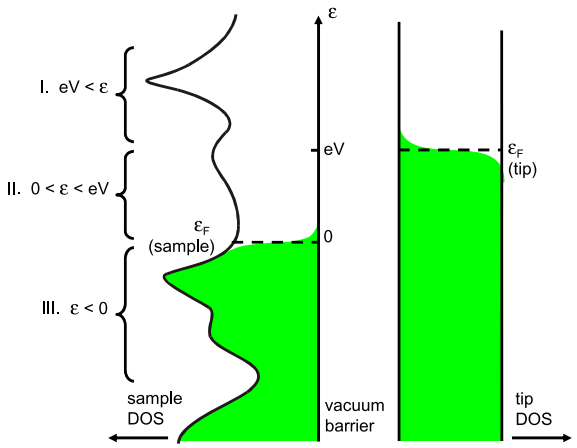


FIGURE 3.1: **Schematic of tunneling**.[132] The curve illustrates the sample density of states(DOS). Positive bias voltage on the sample lowers the sample Fermi energy, so that the electron can tunnel from the tip to the sample. Tunneling current will be roughly proportional to the integrated DOS between the Fermi energy on each side as the tip DOS is flat.

At finite temperatures, when positive bias eV is applied to the sample, the actual tip-to-sample tunneling current for states of energy $\varepsilon$ relative to the *sample* Fermi level is therefore (Fig. 3.1),

$$I_{t\to s} = (-2e)\cdot\frac{2\pi}{\hbar}|M|^2\cdot\rho_t(\varepsilon - eV)f_{FD}(\varepsilon - eV)\cdot\rho_s(\varepsilon)[1 - f_{FD}(\varepsilon)]$$

where

$$f_{FD}(\varepsilon) = \frac{1}{1 + \mathrm{e}^{\varepsilon/k_\mathrm{B}T}}$$

is the Fermi-Dirac distribution function,[1] and $\rho_s$ ($\rho_t$) denotes the density of states of the sample (tip).

Also present is small but finite reverse tunneling current

$$I_{s\to t} = (-2e)\cdot\frac{2\pi}{\hbar}|M|^2\cdot\rho_t(\varepsilon - eV)[1 - f_{FD}(\varepsilon - eV)]\cdot\rho_s(\varepsilon)f_{FD}(\varepsilon).$$

Subtracting the reverse from the forward current and integrating gives the net current

$$I_{t\to s} = -\frac{4\pi e}{\hbar}\int_{-\infty}^{\infty}|M|^2\cdot\rho_t(\varepsilon - eV)\rho_s(\varepsilon)[f_{FD}(\varepsilon - eV) - f_{FD}(\varepsilon)]d\varepsilon$$

which can be simplified owing to the step-like behavior of $f_{FD}(\varepsilon)$ at low temperatures:

$$I_{t\to s} \sim -\frac{4\pi e}{\hbar}\int_{0}^{eV}|M|^2\rho_t(\varepsilon - eV)\rho_s(\varepsilon)d\varepsilon$$

The first two terms of the integrand are taken out under the assumption that both the tip density of states $\rho_t$ and the matrix element $|M|^2$ are independent of the bias voltage, giving

$$I_{t\to s} \sim -\frac{4\pi e}{\hbar}|M|^2\rho_t\int_{0}^{eV}\rho_s(\varepsilon)d\varepsilon.$$

Approximating the tip apex with $s$-wave shape, Tersoff and Hamann calculated the matrix element[133] as $|M|^2 \propto \mathrm{e}^{-2\kappa d}$ with $\kappa = d\sqrt{2m\phi/\hbar^2}$ where $\phi$ is the work function and $d$ is the distance between the sample surface and the center of the approximated $s$-wave apex. The final form of the tunneling current is thus

$$I_{t\to s}(\mathbf{r}, E = eV) \sim -\frac{4\pi e}{\hbar}\mathrm{e}^{-d\sqrt{\frac{8m\phi}{\hbar^2}}}\rho_t\int_{0}^{eV}\rho_s(\mathbf{r},\varepsilon)d\varepsilon. \tag{3.1.1}$$

Thermal broadening at finite temperatures of the ideal step-like $f_{FD}(\varepsilon)$ distribution function limits the practical measurement resolution. As $k_\mathrm{B}T$ broadening on both sides of the Fermi energy occurs on the tip as well as sample, the overall energy resolution is roughly $4k_\mathrm{B}T$, which is about 1.4mV at 4K for example. However, the energy resolution is further limited by the lock-in technique, as will be discussed in later section.

[1] The orbital indices of M are dropped, as M is evaluated below to be independent of $m$ and $n$.

### 3.1.2 Matrix element effect in dSC experiment

The above formalism best describes the direct tunneling between the wavefunction of *s*-orbital tip apex and the wavefunctions at the sample surface nearest to the tip. STM experiments on cleaved cuprate surfaces, however, involve more complicated process for a few reasons.

At first, electron has to travel through many atoms. In the case of BSCCO, for example, quasi-two-dimensional superconductivity arises from the $CuO_2$ layer(s) while the sample cleaves mostly at the charge-neutral BiO layer. The electron that carries physical information of interest has to be carried from the $CuO_2$ plane to the tip through SrO and BiO layers as well as the vacuum insulating barrier. The primary conducting channel is modeled by some researchers as Cu $3d_{z^2} - p_z$ (of apical oxygen in SrO layer) $-p_z$ (of Bi atom in BiO layer).[134]

Another complicating factor is related with the orbital of the atom at the tip apex. *s*-wave approximation discussed above is not consistent with the experience of slight tip changes during scanning, which STM experimenters suspect to be coming from Bi atom attached to and/or detached from the tip. With Todorov-Pendry expression of differential conductance which takes into account the symmetry of the tip orbital beyond *s*-wave, Suominen *et al.* were able to show that the experimental topographic corrugations are consistent with either $s$ or $p_z$ orbital at the tip.[135] In their calculation the corrugation appears completely out-of-phase when the tip has *p*-orbital parallel to the *a*-*b* plane. The dominance of $s$ or $p_z$ orbital can also explain why the oxygen at the exposed BiO layer is invisible: $p_x$ or $p_y$ of oxygen has little overlap with $s$ or $p_z$ orbital of the tip, and the overlap between oxygen $p_z$ and underlying Sr $s$ orbital will be weaker than the overlap between $p_z$ of Bi atom and that of the apical oxygen.

## 3.2 Scanning

### 3.2.1 Tunneling current amplifier

Tip-sample tunneling current is typically as low as tens of pA. The extremely small current needs to be amplified for practical application, including coarse approach (walking), topography, spectroscopy, and field-treatment of the tip all alike. The current amplifier is in fact the first stage the raw tunneling current has to pass through.

It is a general rule of thumb in electronics that the amplifier is placed as close to the signal source as possible. For practical reasons such as space limitations and heat generation, however, the STM current amplifiers are usually located immediately outside the vacuum chamber.[2] A meter-long signal wire for the raw current is doubly protected against noise introduction until amplified, with the metallic shield of coaxial cable and the cryogenic vacuum chamber made of stainless steel. Amplifier is located immediately after the vacuum feedthrough, and should be inside grounded metallic enclosure for further shielding.

In usual STM experiment, trans-impedance amplifier of $10^9$ gain converts 1pA current input into 1mV voltage output. The essential building block for this function is the operational amplifier (Op-Amp) combined with 1GΩ negative feedback resistor as shown schematically in Fig. 3.2. One other crucial role of op-amp stage is providing actively-maintained voltage ground to the tip.

Field-emitting the tip against gold target (will be discussed in later section) requires bias voltage as high as 300V. Resulting tunneling current of up to a few $\mu$A will translate to a few kV by the 1GΩ resistor.[3] The excessive output voltage can be avoided by reducing the gain down to $10^6$. Unlike STM1 which uses separate amplifier for the field-emission,[128] BNL STM has two transimpedance (1GΩ and 1MΩ) resistors side by side. Operators can select appropriate resistance with a relay, effectively covering 6 orders of magnitude range of the tunneling current.

[2] Some STM have amplifier inside the chamber. Or the amplifier is split into two stages so that the first stage pre-amplifies with moderate gain and the outside second stage does the rest.

[3] In fact this cannot occur, because the output voltage of an Op-Amp cannot exceed the voltage supplied to the IC chip which is usually ±15V.

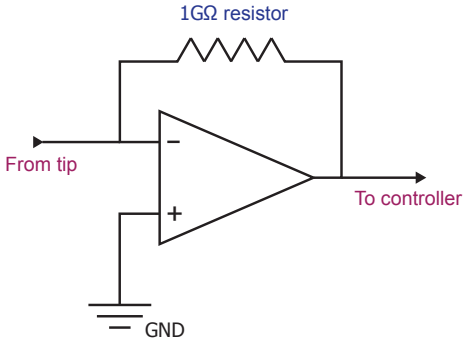


FIGURE 3.2: **Transimpedance amplifier.** Op-amp has negligible bias current; the tunneling current from the tip almost completely flows through the 1GΩ resistor. Output voltage is inverted (negative voltage for currents to the right, or out of the tip.) as the inverting input is at electrical ground.

### 3.2.2 Walker

Equipped with the tunneling current amplifier, the tip is ready to 'walk' toward the sample. Six shear piezo walker stacks generate vertical motion of the sapphire prism tip assembly. [136] Walking step size varies with temperature; with 240V at the base temperature ∼4K, one step moves the tip by about 20nm, which is only ∼1/5 of room temperature value. This coarse approach is a very rough process involving step-like voltage jumps of ΔV=300V tens of times per second. So the sapphire prism is first walked fast to 100$\mu$m tip-sample distance, and then very slow final approach accompanies. For the final approach, three steps are repeated - (1) piezo $z$-voltage ramps from -220V to +220V (2) $V_z$ returns to -220V (3) walk forward one step - until the tip senses the surface (Fig. 3.3).

### 3.2.3 Vertical position reading

Absolute vertical position of the tip at feedback distance should be roughly the same every time unless the tip is replaced. Knowledge of the tip height thus saves a few days of potential approach time. Capacitor made of two concentric cylindrical shells, with inner (outer) shell attached on the moving (fixed) parts, allows for determination of the tip height with high precision. [129] Inductor - capacitor (LC) bridge with lock-in read-out used for many years was recently replaced by a ultra high-precision capacitance bridge manufactured by

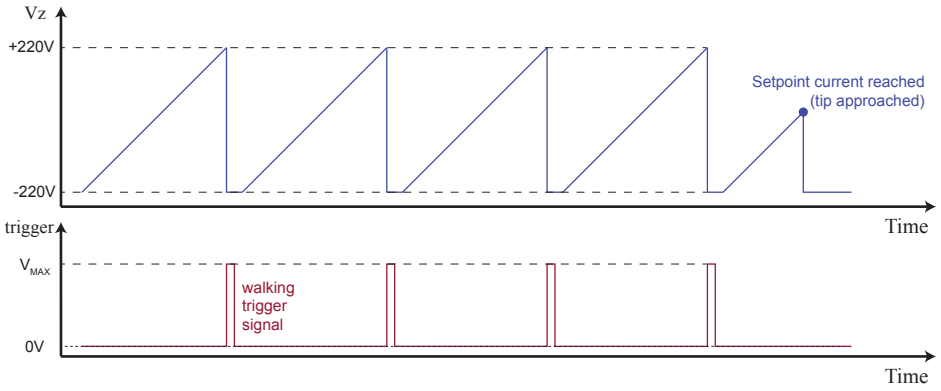


FIGURE 3.3: **Walking signal timing sequence.** First the piezo z-voltage ramps to +220V. If the tunneling current doesn't reach the target value, $V_z$ returns to -220V and trigger pulse is delivered to the walker for one step forward. Ramping stops and $V_z$ returns to -220V once the set point current is reached.

Andeen-Hagerling. This stand-alone apparatus replaces the entire (1) isolation transformer (2) lock-in amplifier (3) reference capacitor (4) preamplifier (for the weak response signal coming out of the cylindrical capacitor) required for the LC-bridge. The bridge can measure capacitance up to 7 digits below the decimal point in pF unit accessing sub-Femto-Farad range. We could see capacitance change even after a few steps of walking, improvement of 10∼20 times compared with the old scheme. Capacitance variations on a few instances are shown in Fig. 3.4.

### 3.2.4 Piezo scanner tube

Ferroelectric crystals exhibit piezoelectricity.[137] Due to its permanent electric polarization, mechanical stress applied parallel to the polarization induces electric potential between the ends. Inversely, external electric field will be converted to the internal structural stress which changes the dimension of the crystal.

PZT ($Pb[Zr_xTi_{1-x}]O_3$) ceramics has been widely used in STM from the beginning as an atomic-scale actuator. The inventors of the STM employed the tri-pod geometry,[138] but they are now mostly superseded by the tube type scanner which is a lot more compact.

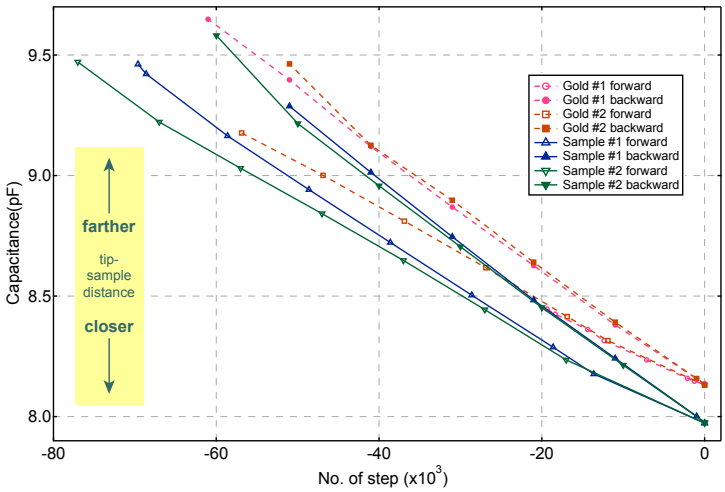


FIGURE 3.4: **Walker position measurement.** Evolution of the absolute capacitance values for approach to (open symbols) and withdrawal from (closed symbol) the field-emission target and the BSCCO samples are shown for two instances respectively. The closer the tip-sample distance, the smaller the capacitance. The final values at feedback are reproduced with high precision and the height difference of the two surfaces are clearly read. Note that the approach (forward) speed is $\sim 2/3$ of the withdrawal (backward) speed. Approach involves moving up the walker assembly in our STM, so the weight of the assembly accounts for the difference.

The tube scanner has piezoelectric material cut in cylindrical shape. Both inner and outer surfaces are coated with metallic electrode, and outer surface has 4 equally divided section. $z$ voltage applied inside stretches the tube along the axis, and $+/-$ X/Y voltages applied on the opposite electrodes bend the tube along X and Y direction as in Fig. 3.5

The tube scanner holds the tip immediately outside and below. Stability of the tube scanner is therefore critical in the overall vibration performance of the STM. Shorter scanner provides higher stability, but at the expense of the lateral as well as vertical range. Currently STM1 (STM2) uses L=1/4" (3/8") scanner tube. For a comparison, 1/2"-long tube scanner of BNL STM can be deflected over nominal range of about $1\mu m \times 1\mu m$.

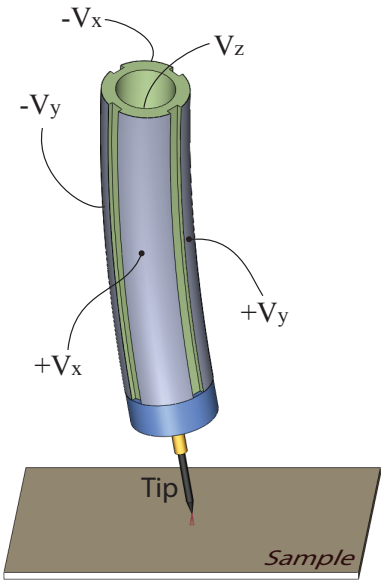


FIGURE 3.5: **Bent tube scanner** Tube scanner holding the tip at one end is bent with voltage applied on the quadrature pad. Here Y voltages bent the tip to the right side of the figure.

## 3.3 Microscope

### 3.3.1 Topography & Feedback loop

Topographic image of a surface can be obtained in two methods. In the simpler of the two, the constant height mode, tip scans the surface with $V_z$ fixed, or at a fixed absolute height. As the tunneling current will vary depending on the tip-sample distance, spatial map of the current itself directly shows the surface topography. This scheme does not require complicated feedback circuitry, but the tip can hit the sample or the tip can get too far away from the sample if the surface is very rough or the surface normal is at an angle with the vertical tip. Consequently topographic image is typically obtained with the second method, the constant current mode with feedback.

In constant current mode, the tunneling current is kept constant by feedback circuitry (Fig. 3.6). When the tunneling current exceeds the set value, the $z$-piezo voltage is reduced

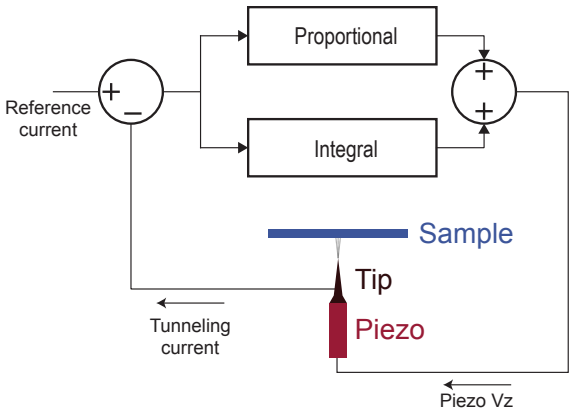


FIGURE 3.6: **Feedback scheme in STM** The difference between the tunneling current and the reference signal (set point current) is amplified according to the PID gain parameters. The amplified signal is fed back to the $z$-voltage which adjust tip-sample distance, consequently the tunneling current. Differential gain is not used usually so omitted here.

proportional to the difference, increasing the tip-sample distance to lower the current. Similarly, $z$ voltage is increased for the tip to get closer to the surface when the tunneling current is lower than the set value. Thus the tip will follow the surface at a fixed distance[4]. $z$ voltage variation recorded at all locations reproduces the topography.

The error signal $e(t)$, the difference between the target setpoint value and the actual input current, is amplified and converted to voltage through gain stage. There are three parameters that determine the feedback speed and efficiency: Proportional (P) / Integral (I) / Differential (D) gain. The PID gain control scheme can be put together into an equation

$$V_z(t) = K_p \cdot e(t) + K_i \int_0^t e(t')dt' + K_d \frac{d}{dt} e(t).$$

Here the coefficients $K_p, K_i, K_d$ represent P/I/D gain. Typical values are P=0, I=200, D=0.

Example of a topographic image obtained with the constant-current mode is shown in Fig. 3.7. Atomic-scale resolving power of STM is manifest, from the dollar-sign(\$)-like features as well as supermodulation.

[4] Constant current converts to constant tip-sample distance only when the LDOS is constant over the scanned area, which is not the case in practice. The discrepancy is a problem particularly when the LDOS considerably fluctuates. This issue will be discussed further in chapter 5 and 6.

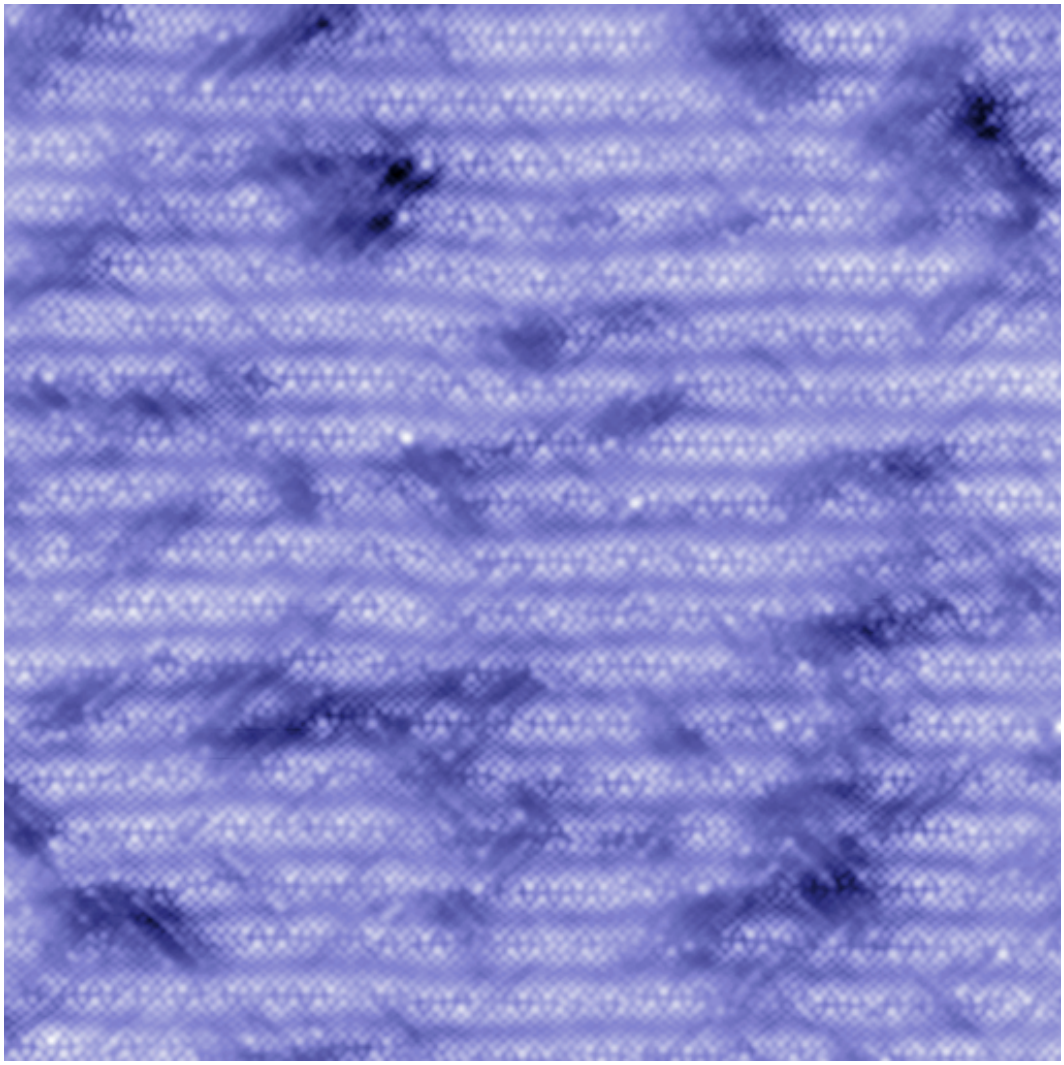

FIGURE 3.7: **Topographic Image** of $Bi_2Sr_2CaCu_2O_{8+\delta}$ obtained with BNL SI-STM (+200mV bias, 20pA setup current, 46nm×46nm nominal field of view, 512×512 pixel). The extremely underdoped sample ($T_c$=15K) was grown by Genda Gu of BNL.

### 3.3.2 Mechanical vibration isolation

Vibration isolation is a critical element of any ultra high-precision measurement. External mechanical vibration is attenuated in Cornell STMs with dual stages of air-spring. The first set of air-spring isolates 30 ton concrete block from the concrete foundation of the building basement. BNL STM1 has different setup. As the system is in a single-story building founded on a soft soil ground, much heavier 100 ton concrete block is buried directly on the ground, separated from the rest of the building (see Fig. 3.8).

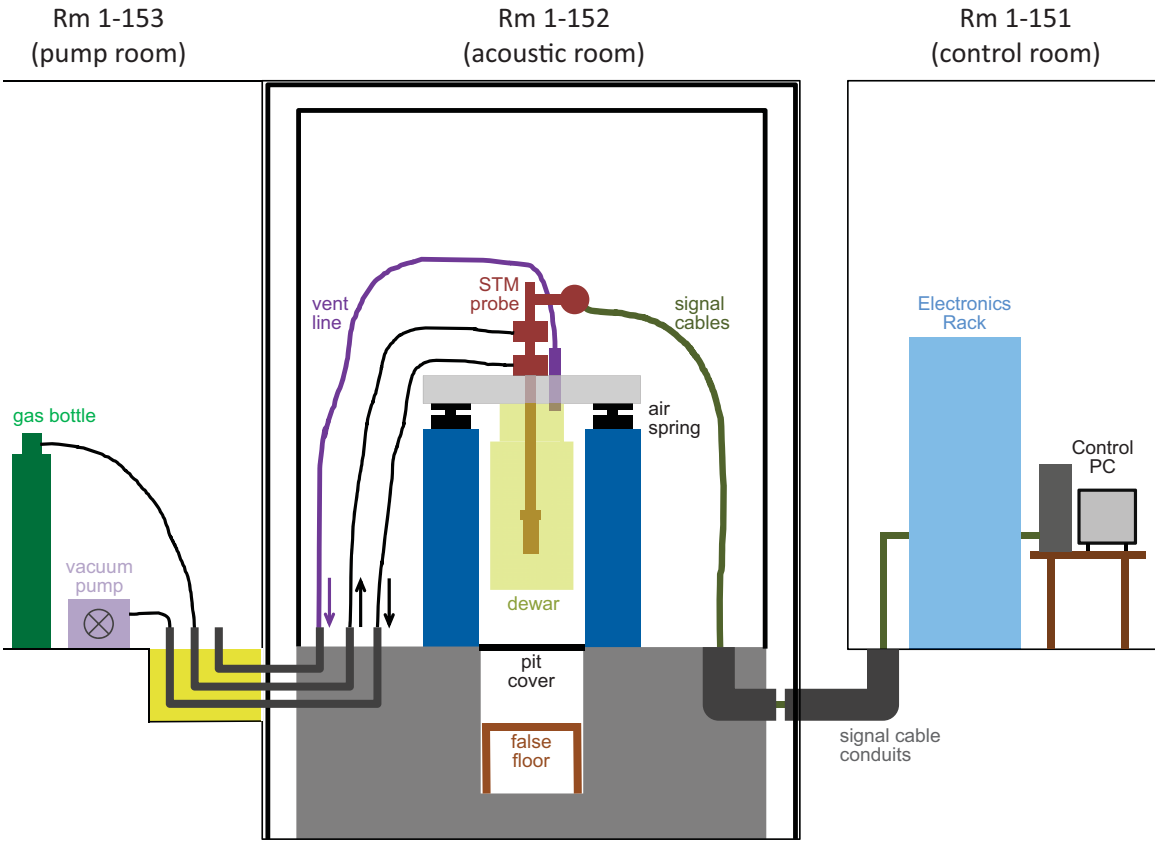


FIGURE 3.8: **Vibration isolation system of BNL SI-STM** Inner acoustic enclosure sits on the 100-ton concrete block buried in the base soil ground. Three-leg pedestals stand on the concrete block, which supports the cryostat plus top plate with three air springs. The concrete block is physically detached from the rest of the building.

The second isolation stage lying on top of the concrete block is almost identical to the Cornell STMs except for the leg height. Three cubic wooden pedestals filled with ∼600kg of #8 (0.09" diameter) lead shots are located at the vertices of equilateral triangle of ∼80"-long edges. On top of each pedestal is an air-spring manufactured by TMC that supports a triangular platform which holds the cryostat, cryogenic experimental dewar, pumps, gauges, and other peripheral apparatus.

Each air spring was designed for maximum support weight of 1000lbs. The acceleration transmissibility (ratio of the input and the transmitted acceleration) exhibits low-pass filter characteristic with peak at about 2Hz and steep decrease of -40dB/decade beyond so that the isolation efficiency is over 97% for both horizontal and vertical vibration at 10Hz. The total weight supported by the air springs is roughly estimated to be 1500lbs, which requires 58psi pressure supplied by Nitrogen gas.

Two sets of conduit connects the acoustically isolated chamber to the control room and the pump room. Unused gas conduits (on the left side of Fig. 3.8) are closed tight with KF cap flanges, and the large plastic signal conduits (on the right side) are filled with sponges to prevent acoustic noise from being introduced.

### 3.3.3 STM head

The core components of STM - tip, sample, piezo actuator - are housed in a compact Macor body (Fig. 3.9). Tube piezo scanner and the tip assembly are located in the center hole of the sapphire prism, and total of 6 shear piezo stacks press the polished sapphire prism; 4 against the inner wall of Macor body and 2 against Beryllium-Copper (BeCu) press plate. Capacitance position sensor is at the bottom of the head.

High voltage signals for the walker and the scanner are supplied by insulation-coated copper wires that run along the inner wall of the Macor body and through the prism hole, respectively. These wires are soldered at the inner end of the 9-pin receptacle array on the side. On the outer end, mating 9-pin connectors bring down coaxial cables corresponding to the individual signal. Tunneling current / sample bias / capacitance signal wires are connected through a vertical post fixed on the bottom plate. (Refer to appendix A for connection diagram in detail and pictures.)

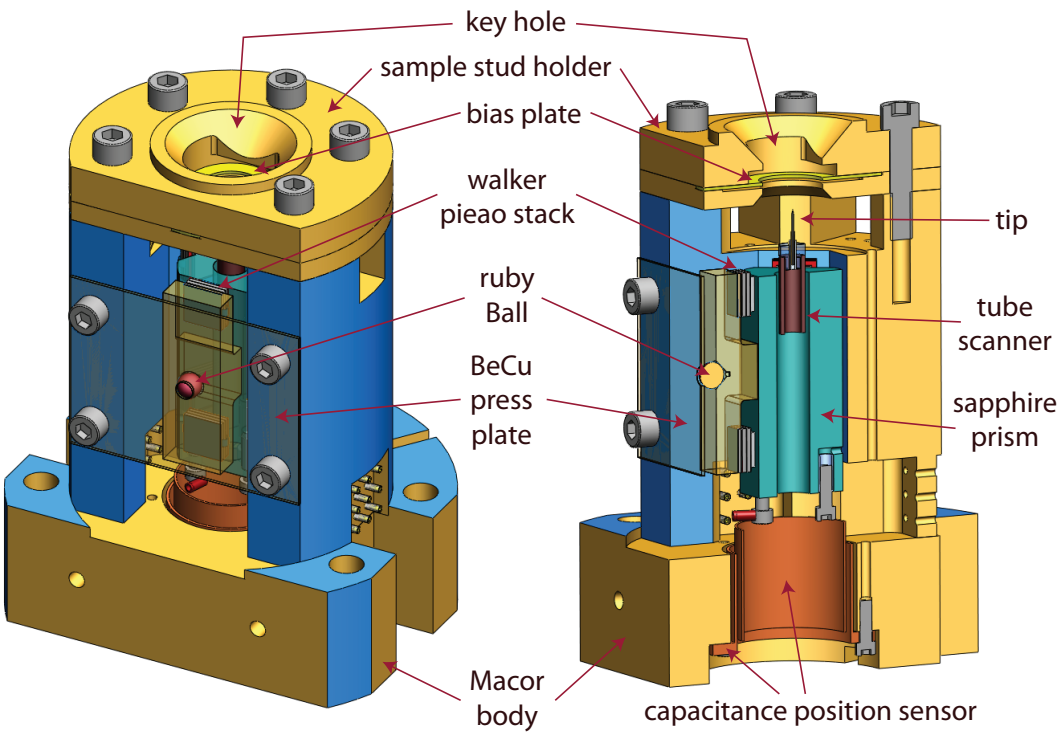


FIGURE 3.9: **BNL STM1 head.** (left) trimetric projection (right) cross-sectional view of the head design. Inverted T-shape tube scanner holder that fits into the sapphire prism center hole from the bottom is not drawn.

Sample studs are lowered with sample facing down (toward the tip). After the stud wing passes the locking key hole, stud is engaged into the sample stud holder by 90-degree rotation. Stud wings are in electrical contact with the bias plate once the sample stud is lowered all the way down. As the tip is at ground, potential difference is established between the tip and sample. Now the tip is ready for approach.

### 3.3.4 Electronic Control Unit (ECU)

Operation of STM requires communication of a number of different signal. A centralized control unit called ECU, analogous to the CPU of a computer, takes care of most of them.

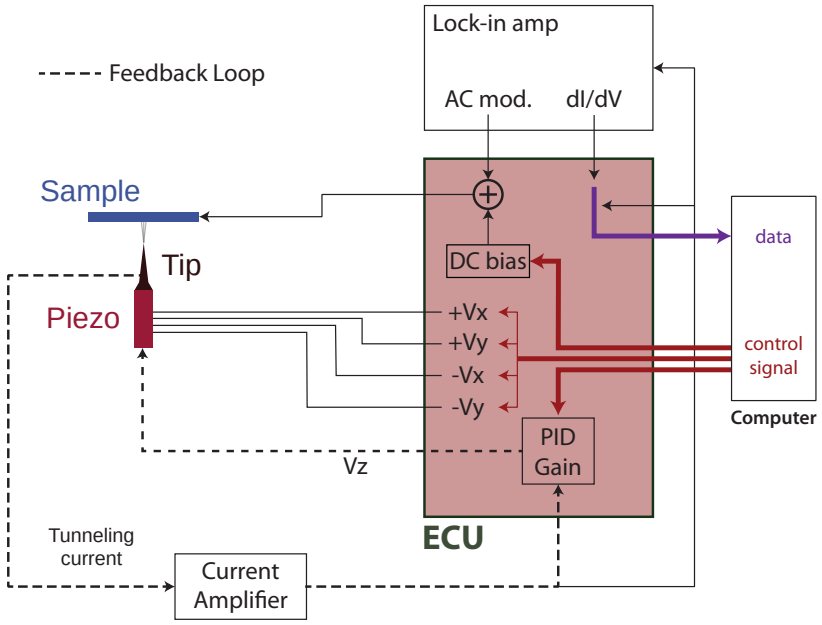


FIGURE 3.10: **ECU & signal flow.** Block diagram of core components including ECU and lock-in amp. Also shown are the signal flow between components. Thick dashed line represents the feedback loop.

Most importantly, ECU contains DSP(digital signal processor)-based PID gain stage for tunneling current feedback where the PID parameters are provided by the user input. Numerous other parameters as well as control signals are also supplied to the ECU from the PC such as the voltages for piezo lateral movement and the DC component of sample bias. PC sends small control signal only; they are converted to the actual voltage output up to a few hundred volts. In addition, sinusoidal modulation of a few mV amplitude from Lock-in amplifier (for spectroscopy measurement, discussed in the following section) is superposed to the DC bias inside the ECU and finally delivered to the sample. Not only receiving control signals from the computer, ECU also collects current and differential conductance data and send them to the computer for storage and analysis.

Most signals inside ECU are manipulated in 16-bit digital waveform. Analog-to-digital and digital-to-analog converters (ADC / DAC) are in place for transforming the input and output signals respectively. See Fig. 3.10 for control signal flow. BNL STM is equipped

with an ECU manufactured by Topometrix (now obsolete), and a software for overall control (TopoSPM) runs on Windows 95 operating system.

## 3.4 Spectroscopy

### 3.4.1 Lock-in technique

Numerous properties of a material are determined by its *electronic structure* near the Fermi energy. The power of STM lies in its capability of mapping LDOS at varying energies, allowing for the investigation of the electronic structure in real space both above and below the chemical potential.

LDOS($\mathbf{r}$, E=eV) is embedded in eq. 3.1.1 as the integrand $\rho_s$. Differentiation of the equation with respect to the bias voltage V gives $\rho(r, E)$ within a constant multiplicative factor when the tip-sample distance $d(\mathbf{r})$ does not vary with location:

$$\rho_s(\mathbf{r}, E) \propto \frac{dI(\mathbf{r}, E)}{dV} \equiv g(\mathbf{r}, E) \tag{3.4.1}$$

Differential conductance $dI/dV$ can be directly calculated from numerical differentiation of $I(\mathbf{r}, E)$. This method, however, will give true $dI/dV$ provided that the $I(\mathbf{r}, E)$ is measured at a very fine energy spacing. This is far from the case given the usual energy spacing of 2mV with measurement range of under 100mV. An alternative way is using a lock-in technique which is based on the Taylor series expansion of the tunneling current:

$$I(V) = I(V_0) + \frac{1}{1!}\frac{dI}{dV}\bigg|_{V=V_0}(V - V_0) + \frac{1}{2!}\frac{d^2I}{dV^2}\bigg|_{V=V_0}(V - V_0)^2 + \dots$$

When a sinusoidal modulation $A\sin\omega t$ superposed onto the DC bias $V_0$ drives the sample, the current response will have DC component plus harmonic signals with integer multiple frequencies of $\omega$:[5]

$$I(V) = I(V_0) + \frac{dI}{dV}\bigg|_{V=V_0} A\sin\omega t + \frac{1}{2}\frac{d^2I}{dV^2}\bigg|_{V=V_0} A^2\sin^2\omega t + \dots$$

[5] $\sin^2\omega t = (1 - \cos 2\omega t)/2$; frequency is doubled.

Lock-in amplifier can pick out only the component of the same frequency as the driving frequency with a very high Q, by multiplying the response current with the driving modulation as the reference signal and low-pass filtering the DC component of the product.[6] Noise present in the system can be rejected by selecting the driving frequency away from the noise band.

One caution in using lock-in technique is that the driving signal sweeps finite energy range about the DC bias due to the AC component. Density of states will be effectively averaged over the amplitude, thereby further reducing the overall energy resolution. Combined with thermal broadening, the ultimate energy resolution can be approximately expressed as[140]

$$\Delta E \simeq \sqrt{(3.3k_BT)^2 + (2.5eA)^2}.$$

The amplitude of the AC signal therefore needs to be reduced accordingly at lower temperatures in order not to overwhelm the thermal broadening.

### 3.4.2 STS - Scanning Tunnling Spectroscopy

Output of the lock-in amplifier(LIA) is first averaged over a duration longer than the time constant, which is a measure of the low-pass filtering time scale (filter cutoff frequency $\omega_c = 2\pi/T$). This constitutes one data point associated with two spatial and one energy indices. One obtains a point spectrum of differential conductance when the same operation is repeated over a finite energy range at a fixed location and height with feedback turned off. Feedback is temporarily restored until the STM is prepared to take another point spectrum. For that purpose the tip needs to be retracted because the conductance spectra are obtained with the tip closer to the surface for higher signal-to-noise ratio than moving distance, and also because the tip is much more likely to degrade if moved laterally very close to the surface. In practice the tip (1) is pulled away from the surface, (2) moves to the next location, (3) re-approaches closer to the surface (Woodpecker mode[128]). Then the feedback is turned off for next point spectrum measurement. The required sequence of signals is generated by the TopoSPM software, eventually converted to the appropriate piezo and bias voltages by ECU.

[6] Similarly, driving with modulation of frequency $\omega$ and demodulating with frequency $2\omega$ picks out the $d^2I/dV^2$ coefficient.[139]

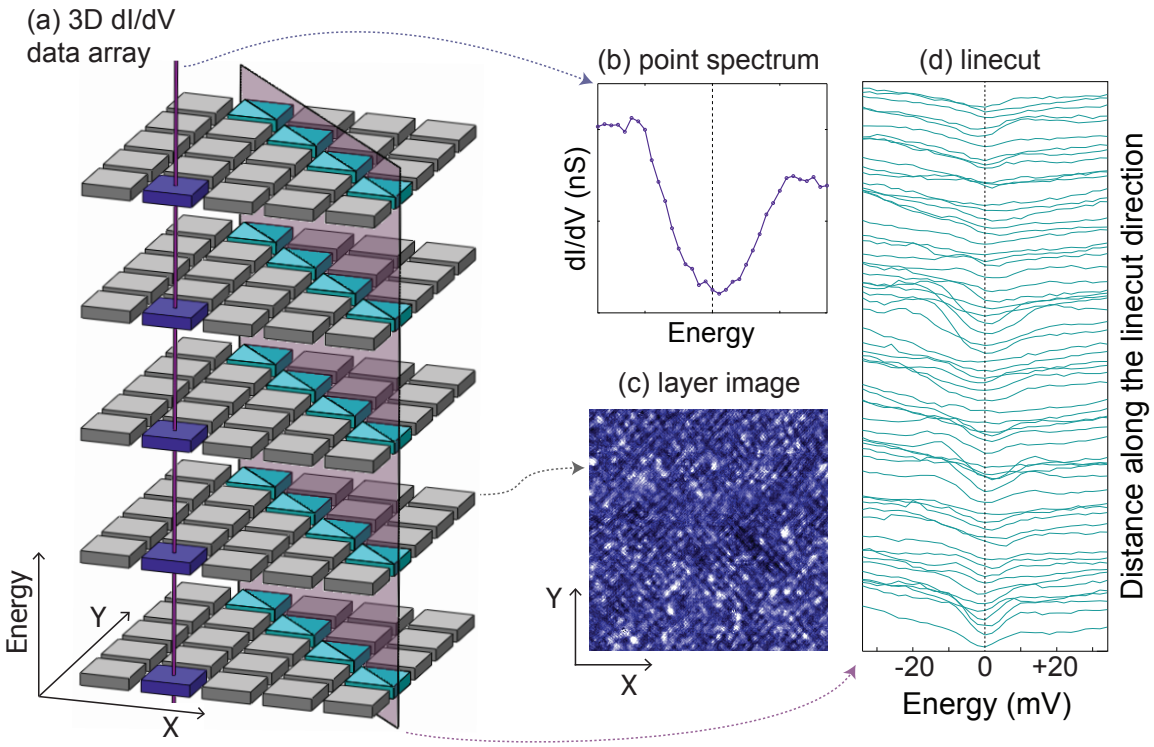


FIGURE 3.11: **Differential conductance data structure.** (a) Differential conductance spectrum acquired at each point is collected into a three dimensional data array with x / y / energy axes. Each cubic cell represents a data point with specific (x, y, E). The data can be analyzed in a number of ways including (but not limited to) (b) point spectrum in which (x, y) coordinates are fixed (represented by a vertical rod connecting all points with the same spatial coordinates) (c) layer image in which energy is fixed (d) linecut, or collection of the point spectra along an arbitrary line in (x, y) plane. The cyan cells and the vertical plane passing through them represent data points used for the linecut. Note that the coherence peaks are very weak because the actual data in (b)-(d) were taken from the strongly underdoped $Bi_2Sr_2CaCu_2O_{8+\delta}$ that will be discussed in detail in later chapters.

Collection of spectra obtained at evenly spaced two-dimensional lattice points make up a three-dimensional data structure as shown in Fig. 3.11 (a). Equivalently, the structure can be regarded as an energy-wise compilation of two-dimensional LDOS maps $g(\mathbf{r}, E = E_0)$ (see the definition in eq. 3.4.1), validating the name Spectroscopic-Imaging (SI)-STM.

Typical averaging time for each data cell is about 25ms. But the actual time interval between adjacent data cell is in fact longer, because it takes finite time to increase (the DC component of) the bias voltage to the next value as well as to move the tip to the

next location. A few types of delay are also interlaced for stability after any parameter is changed. These time fragments add up to about 40ms per each cell. When repeated for a typical 256 pixels × 256 pixels × 101 layers data array (∼$6\times10^6$ cells), this small time scale accumulates to 100+ hours in some cases. Longer measurement time is preferred as it will improve the signal quality. But the total available measurement duration is ultimately limited by LHe lead time (to be discussed in the next section) as well as piezo drift at elevated temperatures.

### 3.4.3 FT-STS: Scanning range issue

Since the discovery of the octet Quasi-Particle Interference (QPI) which directly reveals the $d$-wave superconducting order parameter,[141,142] Fourier-transforming the real-space $g(\mathbf{r}, E)$ map into the momentum-space counterpart $g(\mathbf{q}, E)$ has now become a standard method of studying the electronic structure. One immediate issue in transformation into the reciprocal space is the field of view (FOV) size in real space, because the resolution (defined as the coverage per pixel) in real space and momentum space are conjugated much like in the uncertainty principle. There is one additional restriction in this case: the Bragg peak must be retained in $g(\mathbf{q}, E)$ as it provides the unit length scale in momentum space. In this section, relevant parameters and FOV decision criteria will be discussed in more detail, expanding Dr. Hoffman's description.[143]

The basic rule relating the real space modulation and the associated momentum space feature in discrete Fourier transform (DFT) is that the number of repetition ($N_R$) contained in a 1D real space pixel array is represented by a momentum space peak at location $N_R$ away from the origin as in Fig. 3.12 (a) and (b). For a 4-pixel array with indices n=0∼3, a sinusoidal wave with 4-pixel period ($N_R$=1) corresponds to a peak at n=1 in momentum space. Similarly, a sinusoidal wave with 2-pixels period ($N_R$=2) gives a peak at n=2 in momentum space. Equivalently, the real-space wavelength in pixel unit (4 in Fig. 3.12 (a)) multiplied by the momentum-space peak position (1 in Fig. 3.12 (a)) gives the dimension of the pixel array, which is 4 here. The reciprocity of the real and momentum space resolution is readily verified, as the real(momentum) space resolution is higher in Fig. 3.12 (a)(Fig. 3.12 (b)).

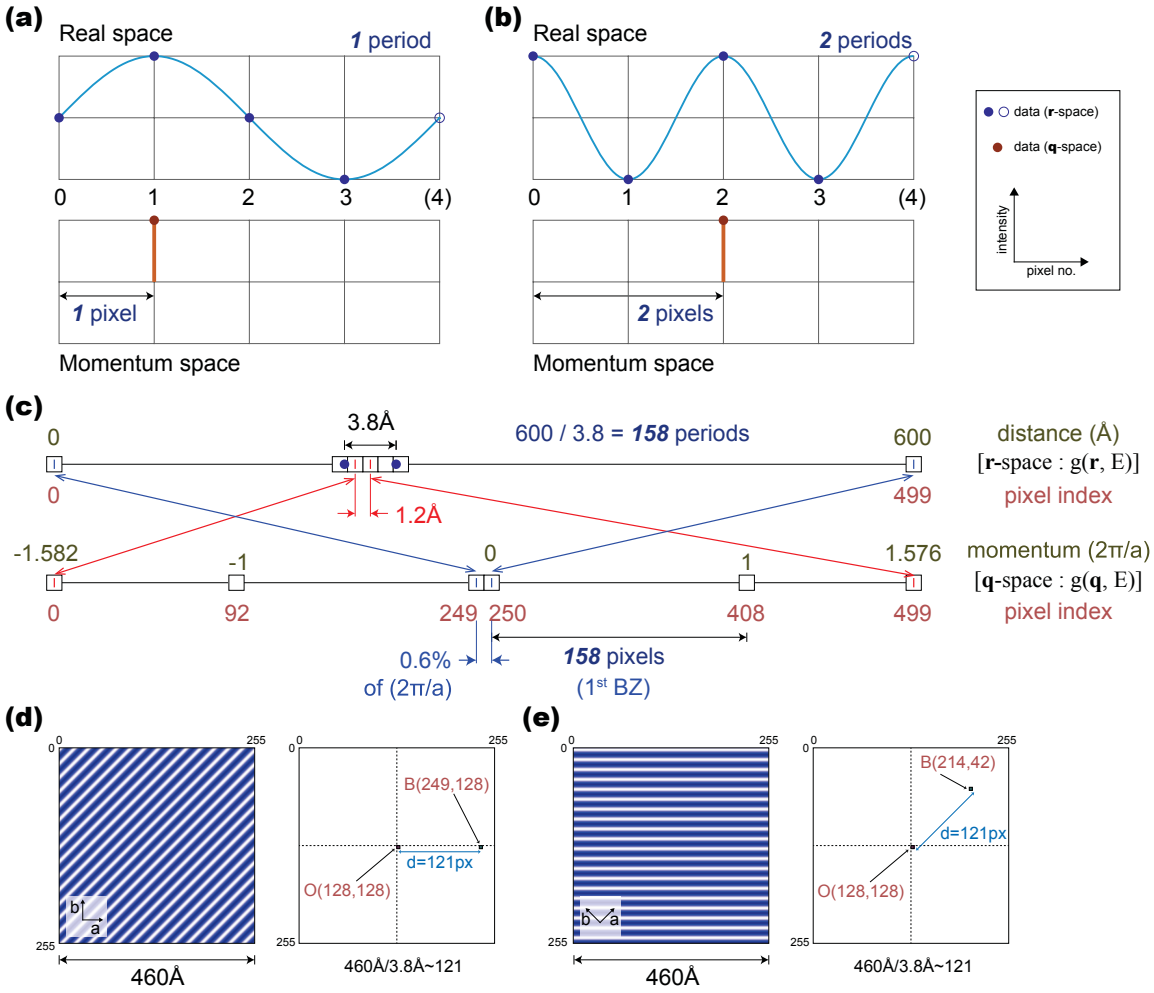


FIGURE 3.12: **Length scale and the field of view in real / momentum space.** (a)-(b) Real space modulation (top) and the corresponding momentum space peaks (bottom) in one-dimensional discrete Fourier transform. Open circles at the cell index in parenthesis reproduce the value at the origin (cyclic repetition). (c) The same relations with associated physical dimensions. Scales are reciprocal: full real space length is equivalent to one cell-spacing in momentum space and vice versa. Note that the origin is at the $250^{th}$ cell, not at the zeroth cell as in (a) and (b). See the text for detail. (d)-(e) Results of 2D FFT. Only the supermodulation is shown in the left image, which lies along the bond diagonal. Crystallographic a and b axes are indicated in the bottom left corner. Origin(O)-to-Bragg(B) peak distance doesn't change with 45° rotation. (e) is the typical orientation for QPI studies discussed in chapter 5 and 6. Note that the momentum space diagram in (d) and (e) has fine details that are visible with magnification. The brown and green cells represent the origin(O) and the Bragg peak (B), respectively.

The same relations can be applied to a more realistic instance, in which 600Å×600Å square FOV of $Bi_2Sr_2CaCu_2O_{8+\delta}$ topographic image is contained in a 2D array of 500×500 pixels with bond direction parallel to the horizontal and vertical axes of the image. $CuO_2$ square plaquette has $a_0$=3.8Å, so 500 pixel contains total of 600/3.8=158 periods. The corresponding Bragg peak (q=$2\pi/a_0$) will be at 158 pixels away from the origin located at the $250^{th}$ pixel, or at the $408^{th}$ pixel. Inverse of 158 pixels gives the momentum space resolution; one-pixel distance in momentum space covers 1/158=0.6% of the first Brillouin zone. On the other hand, a peak at the end-to-end momentum-space distance (500 pixels) is equivalent to the 500 times of repetition or identical pattern at every pixels in real-space. Therefore one-pixel distance in real space (600Å/500 pixels = 1.2Å/pixel in this case) corresponds to the full momentum-space range.

In a real experiment, where the image or map is obtained on a fixed 256×256 pixels two-dimensional array,[7] increasing (decreasing) the real-space FOV size moves the Bragg peaks toward the corner (center), thus increasing (decreasing) the momentum space resolution at the cost of (in favor of) real-space resolution. For the cases in which momentum space resolution is more important, one can increase the FOV to the extent that the Bragg peaks are located exactly at the corners. However, the Bragg peak is typically spread over a few pixels due to the thermal broadening and piezo drift. Reasonable locations for the Bragg peaks may therefore be the $11^{th}$ and $245^{th}$ pixel (10 pixels away from the end) of 256 pixel length along each axes, which gives 117 (=245-128) periods or 44.6nm nominal FOV (=117×3.8Å).

There are two other things to be noted. First, the actual FOV always turns out to be significantly bigger than the nominal FOV. On BNL STM1, 46nm nominal FOV translates to ∼52nm actual FOV, expansion of ∼13% lengthwise. Second, the differential conductance map is preferred to be taken in a rotated coordinates such that the Cu-O bond direction is parallel to the FOV *diagonal*. Then the Bragg peaks will be placed at the four corners of the image, FOV aligning with the anti-ferromagnetic zone boundary. Since pure rotation of FOV should not change the length scale in either real or momentum space, the momentum space image can be further 'zoomed-in' by a factor of $\sqrt{2}$, by moving the Bragg peaks more toward the corners.

[7] Pixel sizes are chosen to be exponents of 2, as it will maximally exploit the FFT algorithm.

As shown in Fig. 3.12 (e), topographic image taken on the 46nm FOV at 45 degree (so that the supermodulation appears horizontal) will give the Bragg peak at 121 pixel-distance away from the center in momentum space. The actual peak will be 13% farther, or 137 pixel-distance away. With 10 pixel margin for the width of the Bragg peak, the atomic peak can be as far to the corner as 198 (=$127\sqrt{2}$-10) pixel away, which corresponds to 75nm actual (66nm nominal) FOV. Combined with the minimum FOV requirement for the 1% momentum space resolution (100 pixels covering $2\pi$), the appropriate FOV range for 256×256 pixel image is between 38nm (33.6nm nominal, for non-rotated image) and 75nm (66.4nm nominal, for 45° rotated image).

## 3.5 Cryogenics

Fig. 3.13 is the schematic of the BNL STM cryostat. A triangular top platform supported by three air springs (see Fig. 3.8) holds the experimental dewar made by Kadel from the top. A dip-type vacuum chamber made of stainless steel (SS) is inserted into the cryogen space and fixed to the platform through the probe neck. The neck has access to the cryogen space for various purposes including pressurizing / evacuating the space.

The 4K flange, dissipation channel of heat inside the chamber, is slightly above the bottom of the dewar belly when the probe is in place. In order to keep the STM head at its base temperature ∼4.5K during normal operation, liquid helium is filled up to the 4K flange level at all times. The belly volume minus the probe volume and the amount of helium to maintain the minimum level is about 50 liters. With properly evacuated dewar vacuum jacket, the boil-off loss rate is approximately 5 liters/day or 1.2 inches/day (height of the helium is measured relative to the top surface of the 4K flange), providing maximum 10 days of lead time, or less at higher measurement temperatures. A SS pipe that runs all the way down is attached to the side of the probe for convenient access to the dewar bottom. (See Appendix B for detail.)

To reach the base temperature, the probe is pre-cooled to 77K with liquid nitrogen over a day, and further cooled with liquid helium in a few hours. Temperature drop also lowers the pressure. With the cryo-pumping in action, STM head area is in a strong UHV condition because the equilibrium pressure of the vacuum chamber top at room temperature is in the

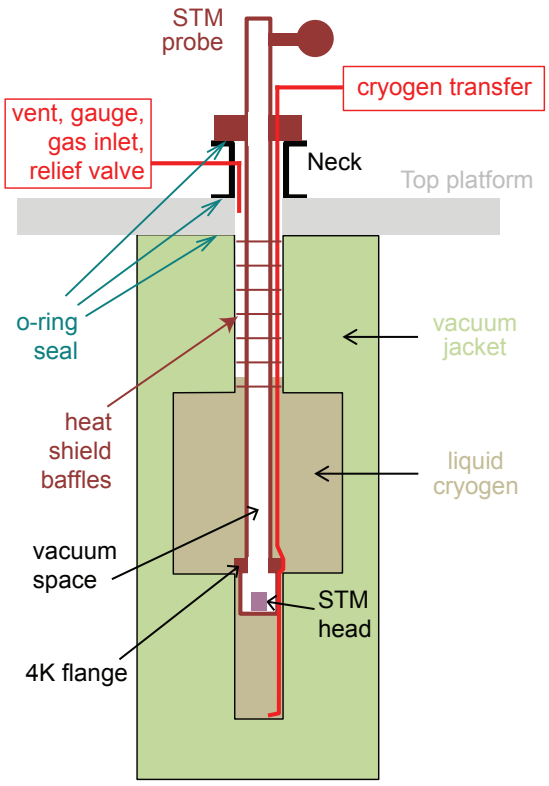


FIGURE 3.13: **Cryogenic dewar and probe.** Top platform holds the dewar and the dip-type STM probe that sits on a neck. O-rings seal the cryogen space for pressurization / evacuation of the space for various purposes. The STM head is lower than the dewar belly bottom, so that 4K flange and the portion below are always immersed in the liquid helium. A few thin SS disks are attached to the probe in the dewar neck height to minimize heat influx due to the temperature differences.

mid-$10^{-8}$ Torr range. Falling temperature and the subsequent thermal contraction affect other parameters as well. For example, at the base temperature, walking step size is reduced by a factor of 5 and the capacitance reading decreases by 0.1pF (implying smaller tip-sample distance).

In 2007, BNL STM (old Cornell STM3) was upgraded to a variable temperature system. A temperature feedback circuit was implemented with a heater at the base plate, the output current for which is regulated by a Lakeshore 340 controller for a stable higher temperature. Successful differential conductance map was obtained at up to 55K. (See Chapter 5 and Appendix A for detail.)

# Chapter 4

# Real Space: Intra-unit-cell electronic nematicity

## 4.1 Broken symmetries of the pseudogap

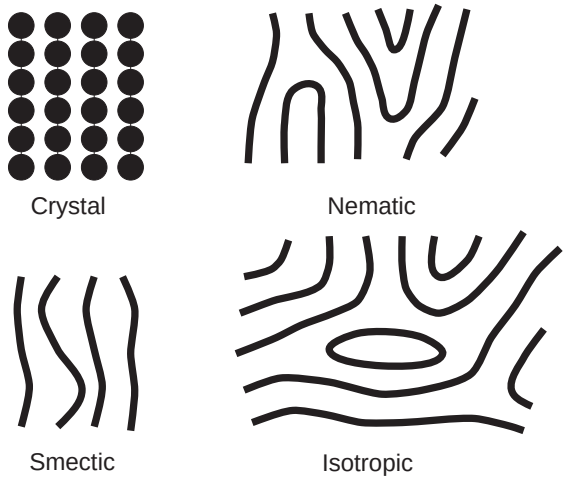


FIGURE 4.1: **Nematicity and smecticity**.[144] Schematic representations of various electronic states with broken symmetry. Nematic order arises when the four-fold rotational symmetry of a crystal are broken into two-fold. Further breaking of the translational symmetry induces transition to the smectic order.

A particular phase of matter is associated with specific symmetries. Transitions between the phases is understood to be the braking of one or more of the symmetry. In classical phase transitions states with higher symmetry transforms into those with lower symmetry upon cooling past the critical temperature. In some material the gas phase at high temperature undergoes sublimation into solid, but in other material intermediate liquid states like water exists in between.

An analogue can be made in quantum matter. In between the gas phase where entropy dominates and the solid phase where interaction energy dominates, there is an intermediate liquid phase in which neither dominates so both quantities should be taken into account. Moreover, additional states also form in between the liquid and solid, usually referred to as liquid-crystalline (LC) phase. The phase can flow unlike the crystal solid, but in a restricted geometry lacking isotropy of a liquid.

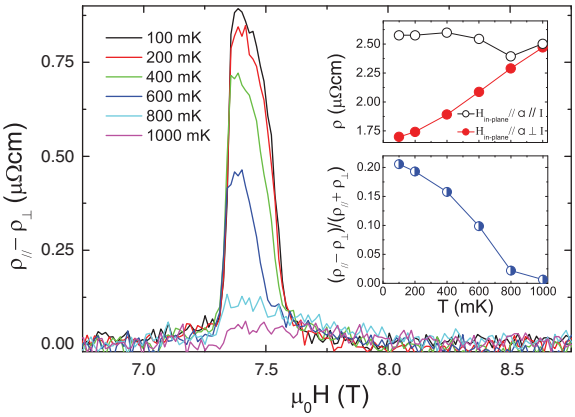


FIGURE 4.2: **Electronic nematicity in $Sr_3Ru_2O_7$.** The resistivities along two orthogonal directions show marked difference near the metamagnetic quantum critical point, consistent with the nematicity of the electronic fluid. Dots of the crystal represent lattice points, and the thick wavy curves represent stripes of electron flow.

Two types of LC phase can occur in a (quasi) two-dimensional system. In the first type, nematic phase, the four-fold rotational symmetry of the lattice is broken but the translation and reflection symmetries are retained; in essence a liquid with a preferred alignment orientation. The second type, smectic phase, forms when the translational invariance of the nematic phase is further broken in only one direction but moves freely in other direction. The smectic or stripe phase can be simply thought of as rivers running nearly parallel (or

within stacked layers in three-dimensional system where layer-crossing is forbidden). Transverse fluctuations of the charge and/or spin stripe due to strong interactions can melt the smectic phase into the nematic phase.

One of the question still in debate surrounding the pseudogap is if the characteristic temperature $T^*$ marks onset of a new phase with spontaneously broken symmetry[145,146] or is a cross-over temperature associated with the classical fluctuation of the superconducting order parameter.[123] Being a phase with broken symmetry, observation of either nematic or smectic order in the pseudogap phase strongly argues in favor of theories regarding $T^*$ as a phase-transition temperature. Indeed, there are experimental evidences for broken symmetries. ARPES measurements with circularly-polarized photon found that time-reversal symmetry is broken in Bi2212,[147] polarized neutron diffraction revealed magnetic order in YBCO,[82] SI-STM experiment showed nematic order in the parent compound of $Ca(Fe_{1-x}Co_x)_2As_2$,[148] the electron transport[149](Fig. 4.2) as well as thermal magneto-transport[150] observed anisotropy in the ultra-pure $Sr_3Ru_2O_7$, etc.

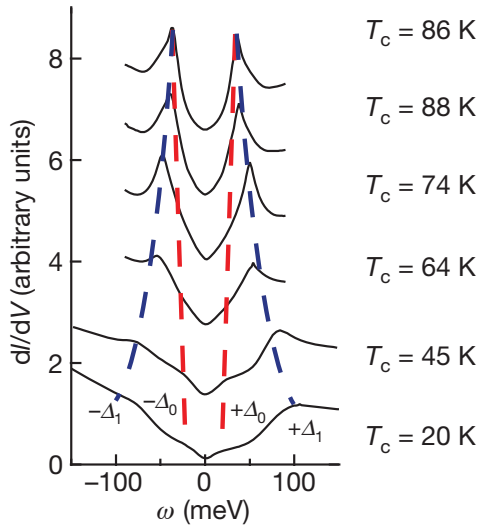


FIGURE 4.3: **Two energy scales.**[61] Evolution of the averaged point spectra with doping indicates two distinct energy scales. The smaller ($\Delta_0$) does not change significantly, whereas $\Delta_1$ has strong doping dependence. $\Delta_1$ scales roughly in accordance with $T^*$.

## 4.2 Pseudogap with STM

Owing to its unique capability of investigating local electronic structure both above and below the chemical potential, STM has become an increasingly important experimental probe to study the pseudogap. The local tunneling spectra, fundamental unit of STM measurement (Chapter 3), readily reveals a feature associated with the pseudogap coexisting with superconductivity without any post-processing. As in Figure 4.3, the spatially averaged differential conductance spectra have symmetric coherence peaks at $E = \pm\Delta_1$.[61] Moving toward the chemical potential and becoming sharper with increasing hole doping (Fig. 4.3), the coherence peak energy scale closely traces the pseudogap temperature $T^*$ with $\Delta_1/k_BT^* \sim 5$ when plotted on a $p$-$T$ phase diagram (Fig. 4.4). This high-energy branch is observed both above and below $T_c$. The nature of the electronic states at $E = \pm\Delta_1$ can thus be studied below $T_c$. In fact, the lowest measurement temperature is preferred for minimal thermal broadening. Consequently, all data presented in this chapter were obtained at $T \sim 4K$.

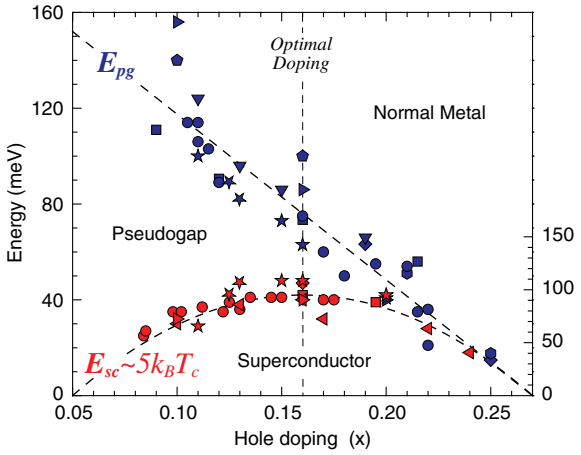


FIGURE 4.4: **Doping vs. Energy phase diagram**.[58] Superconducting ($E_{SC} \sim 5k_BT_c$) and pseudogap ($E_{PG} = 2\Delta_{PG}$) energy scales for HTSCs with various doping levels. The two dotted empirical curves, $E_{PG} = E_{PG}^{\max}(0.27-x)/0.22$ and $E_{SC} = E_{SC}^{\max}[1-82.6(0.16-x)^2]$ where $x$ is the hole concentration, represent universal energy scales independent of material.

The earliest attempts to understand the pseudogap with STM were by Fischer *et al.*[151] in 1998. In the doping-dependence study in 2005, McElroy *et al.* observed that the local tunneling spectra of the underdoped Bi2212 were universal such that the overall shape

depends only on the coherence peak energy regardless of the global hole doping level.[152] Based on the observation that the coherence peaks exist up to 65mV, they separately masked the field of view according to the existence of the peak. While the QPI for $\Delta <$ 65mV (peak present) regions lead to the Fermi arc of the $d$-wave superconductivity at low energy, the complementary region with $\Delta \not< 65$mV contained additional peak along the Cu-O bond direction at higher energies associated with the 'checkerboard' type modulation characteristic of the pseudogap phase (to be discussed in Chapter 6).

Further distinction between the low-energy $d$-wave supderconductivity and high-energy pseudogap, as well as the transformation of the former into the latter was provided by Kohsaka *et al.* From high-resolution QPI data over samples with wide doping range covering most of the underdoping regime, the Bogoliubov QPs were observed to disappear where the normal state Fermi surface crosses the anti-ferromagnetic zone boundary.[153] Beyond the extinction points, the spectral weight of the delocalized **k**-space states are transferred to the high-energy real-space excitations, which locally break the translational and rotational symmetry.

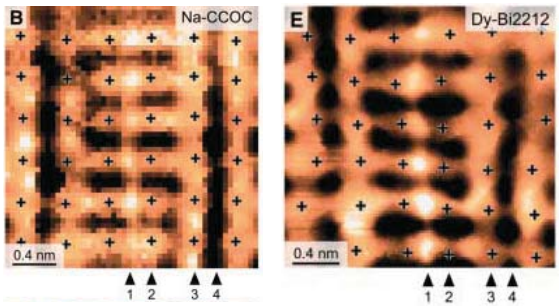


FIGURE 4.5: **Tunneling asymmetry map**.[87] Cu-O bond-centered electronic cluster glass (ECG) patterns are commonly observed in the tunneling asymmetry map of (left) Na-CCOC and (right) Bi2212 compounds, which share little except for the $CuO_2$ planes. Blue crosses denote the location of Cu atoms determined from the topographic map. The LDOS within unit cells has strong intensity anisotropy at the perpendicular oxygen sites. Note that the Cu atoms are significantly displaced off the ideal locations in Bi2212.

The definitive hint for C4 rotational symmetry breaking within unit cell was provided in real space by Kohsaka *et al.*[87] Tunneling asymmetry map ($R(\mathbf{r}, |E|) = I(\mathbf{r}, +E)/I(\mathbf{r}, -E)$) at high energy ($\sim$150mV), which later turned out to be maximally revealing the real-space electronic structure of the pseudogap (Fig. 4.6 (e) and (f)), clearly shows LDOS anisotropy

at two perpendicular oxygen sites neighboring a Cu atom. (Fig. 4.5) How can we quantify the inequivalence of the two oxygen sites? How large will the real-space nematic domain be? How does the nematicity relate with broken symmetry of the pseudogap phase observed by other probes? This chapter will be centered about these questions.

## 4.3 Prerequisites

### 4.3.1 Ratio map in reduced energy scale

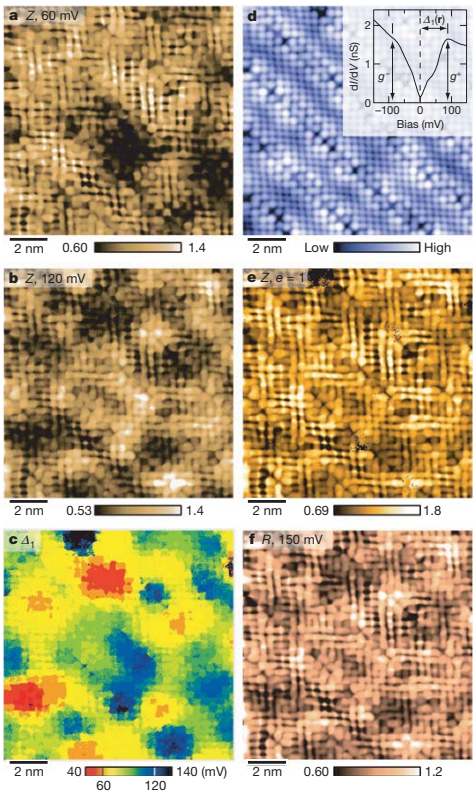


FIGURE 4.6: **Reduced energy scale.**[153] (a-b) the ratio(Z) maps in real-space for E=60mV and 120mV. The intensity modulation patterns of the local electronic structure are markedly distinct at different energies. The variation can be normalized by rescaling the energy of individual point spectra with local pseudogap $\Delta_1(r)$ (c) determined from the simultaneous topograph (d) such that the pseudogap energy is spatially uniform. (e), normalized Z($\mathbf{r}$, $e$=E/$\Delta_1(\mathbf{r})$=1) map, almost identical to the R-map (f). Thus the R-map directly visualizes the electronic structure of the pseudogap with rescaled energies.

Two spatial inhomogeneities complicate the interpretation of the STM data. The first of them, the strong spatial variation of the tip-sample distance (setup effect, see chapter 3) can be eliminated by taking ratio between layers of opposite bias.

The second spatial variation is due to the inhomogeneity of the pseudogap magnitude. Resembling the spatial variation of the superconducting gap magnitude $\Delta_0$,[154] the pseudogap energy scale $\Delta_1$ also varies with location. This effect can be normalized by rescaling the energy of the individual $dI/dV$ spectra with local pseudogap $\Delta_1(\mathbf{r})$. With the reduced energy scale

$$e = \frac{E(\mathbf{r})}{\Delta_1(\mathbf{r})},$$

the pseudogap phenomena can be investigated in a location-independent manner. The unified energy scale was exploited previously in real-space visualization of the pseudogap [153] as shown in Figure 4.6.

### 4.3.2 Pico-meter adjustment of the distorted lattice

The $CuO_2$ unit cell of $Bi_2Sr_2CaCu_2O_{8+\delta}$ has lattice parameters $a = b \sim 4$Å along the Cu-O bond direction, which is close to the lateral resolution of STM. Investigation of sub-unit-cell phenomena as a result requires minimizing any extrinsic distortion. One minute but sizable effect in STM is the deviation of atomic positions from the perfect crystallographic locations (Fig. 4.5), introduced primarily by the continual mechanical / thermal piezo drift during 100+ hours of mapping. These shifts can be corrected to the lattice parameters precisely determined with scattering experiments. After removing distortion due to the drift but not the inhomogeneity such as impurity, modulations due to the $CuO_2$ unit cell and supermodulation that runs diagonal to the Cu-O bond direction can be extracted.

Distortions can be removed with a computational lock-in technique which is a real-space analogue of the lock-in amplification in time domain. Lock-in amplifier extracts a Fourier component of a specified frequency from a time-varying signal with very high Q factors, by multiplying the input signal by a reference sinusoidal wave and low-pass filtering the product. Similarly, a component wave of a specified wavenumber can be extracted from a real-space modulation, where the latter is the actual measurement and the target wavenumber represents the un-distorted tetragonal lattice. Multiplication of the source modulation

with two reference waves with phases differing by 90° enables one to determine the phase difference between the reference and the source signal, a direct measure of the distortion.

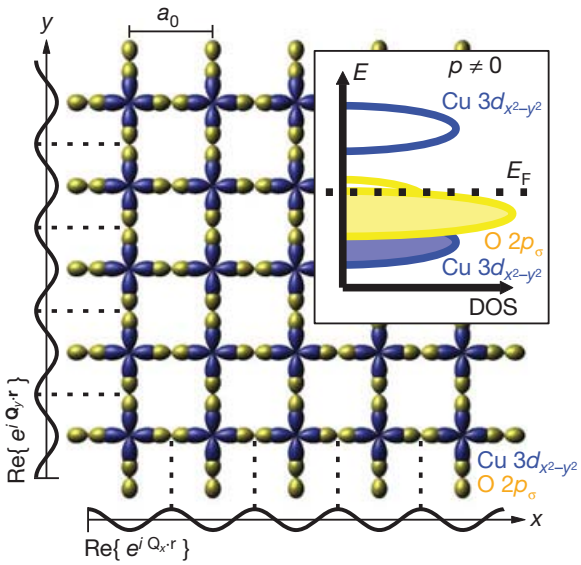


FIGURE 4.7: **Ideal lattice of the $CuO_2$ layer**. The origin of the real space coordinate is defined to be at the ideal Cu sites throughout this chapter. Any q-space modulation at the Bragg wavevector will thus have only the real part non-vanishing with even symmetry about the Cu locations, and the imaginary part vanishing identically. The inset shows the energy band diagram of the charge-transfer Mott insulator, in which the electrons are partially removed (hole-doped) from the oxygen $2p_\sigma$ orbital.

In practice, implementation of this scheme starts with multiplying the topographic image $T(\mathbf{r})$ as measured by reference cosine and sine functions with ideal Bragg wavevectors $\boldsymbol{Q}_a = (Q_{ax}, Q_{ay})$ and $\boldsymbol{Q}_b = (Q_{bx}, Q_{by})$. Each product is low-pass filtered such that the contribution from narrow regions within a radius $\delta q = 1/\lambda$ about $\boldsymbol{Q}_a$ and $\boldsymbol{Q}_b$ are retained only. $\lambda$ should be large compared with the lattice periodicity as well as the supermodulation as both are not to be filtered out. This procedure results in four maps that contain both the amplitude and phase of component wave with wavevectors sharply centered at $\boldsymbol{Q}_a$ and $\boldsymbol{Q}_b$

$$X_a(\mathbf{r}) = R_a(\mathbf{r}) \cos\theta_a(\mathbf{r}), \quad Y_a(\mathbf{r}) = R_a(\mathbf{r}) \sin\theta_a(\mathbf{r}),$$
$$X_b(\mathbf{r}) = R_b(\mathbf{r}) \cos\theta_b(\mathbf{r}), \quad Y_a(\mathbf{r}) = R_b(\mathbf{r}) \sin\theta_b(\mathbf{r}),$$

from which the additional phases due to the drift

$$\begin{aligned}\theta_a(\mathbf{r}) = &\quad \tan^{-1}[Y_a(\mathbf{r})/X_a(\mathbf{r})] \\ \theta_b(\mathbf{r}) = &\quad \tan^{-1}[Y_b(\mathbf{r})/X_b(\mathbf{r})]\end{aligned}$$

can be determined immediately.

In a perfect lattice the $\theta_a$ and $\theta_b$ should both be a constant independent of $\mathbf{r}$, representing the displacement between the ideal periodic array and two-dimensional reference wave along the two directions. In real $T(\mathbf{r})$, however, the ideal undistorted lattice at position $\mathbf{r}$ is shifted by $\mathbf{u}(\mathbf{r})$, with an identical shift occurring in the LDOS map $g(\mathbf{r}, E)$. The topographic image $T(\mathbf{r})$ with the shift can be written as

$$\begin{aligned}T(\mathbf{r}) &= T_0[\cos(\mathbf{Q}_a \cdot (\mathbf{r} - \mathbf{u}(\mathbf{r}) - \mathbf{d})) + \cos(\mathbf{Q}_b \cdot (\mathbf{r} - \mathbf{u}(\mathbf{r}) - \mathbf{d}))] \\ &= T_0[\cos(\mathbf{Q}_a \cdot \mathbf{r} + \theta_a(\mathbf{r}) + \bar{\theta}_a) + \cos(\mathbf{Q}_b \cdot \mathbf{r} + \theta_b(\mathbf{r}) + \bar{\theta}_b)].\end{aligned}$$

These expressions derive from the understanding that (1) the computational lock-in formalism determines the phase differences between the actual modulation and the reference modulation ($\theta_a(\mathbf{r})$ and $\theta_b(\mathbf{r})$) and that (2) the arbitrary choice of the origin of the reference waves introduces another constant phases along each direction ($\bar{\theta}_a$ and $\bar{\theta}_b$). The latter can be set to zero for convenience by placing the origin of the reference cosine waves at the copper site (Fig. 4.7), eliminating the contribution of sine waves.

The displacement due to the drift $\mathbf{u}(\mathbf{r})$ can be determined now from the $\theta_a(\mathbf{r})$ and $\theta_b(\mathbf{r})$ maps, as they are related by $\theta_i(\mathbf{r}) = -\mathbf{Q}_i \cdot \mathbf{u}(\mathbf{r})$ ($i$=a, b), or in a tensor form,

$$\begin{pmatrix} \theta_a(\mathbf{r}) \\ \theta_b(\mathbf{r}) \end{pmatrix} = -\overleftrightarrow{\mathbf{Q}} \cdot \mathbf{u}(\mathbf{r}) = -\begin{pmatrix} Q_{ax} & Q_{ay} \\ Q_{bx} & Q_{by} \end{pmatrix} \begin{pmatrix} u_x(\mathbf{r}) \\ u_y(\mathbf{r}) \end{pmatrix}.$$

Because $\mathbf{Q}_a$ and $\mathbf{Q}_b$ are orthogonal, $\overleftrightarrow{\mathbf{Q}}$ can be inverted[1] to yield

$$\mathbf{u}(\mathbf{r}) = \overleftrightarrow{\mathbf{Q}}^{-1} \begin{pmatrix} \theta_a(\mathbf{r}) \\ \theta_b(\mathbf{r}) \end{pmatrix}.$$

[1]Both $Q_{bx}$ and $Q_{by}$ should be identically zero in order for the determinant of $\mathbf{Q}$ to vanish under the orthogonality condition $Q_{ax}Q_{bx} + Q_{ay}Q_{by} = 0$. This is not the case, so $\mathbf{Q}$ is invertible.

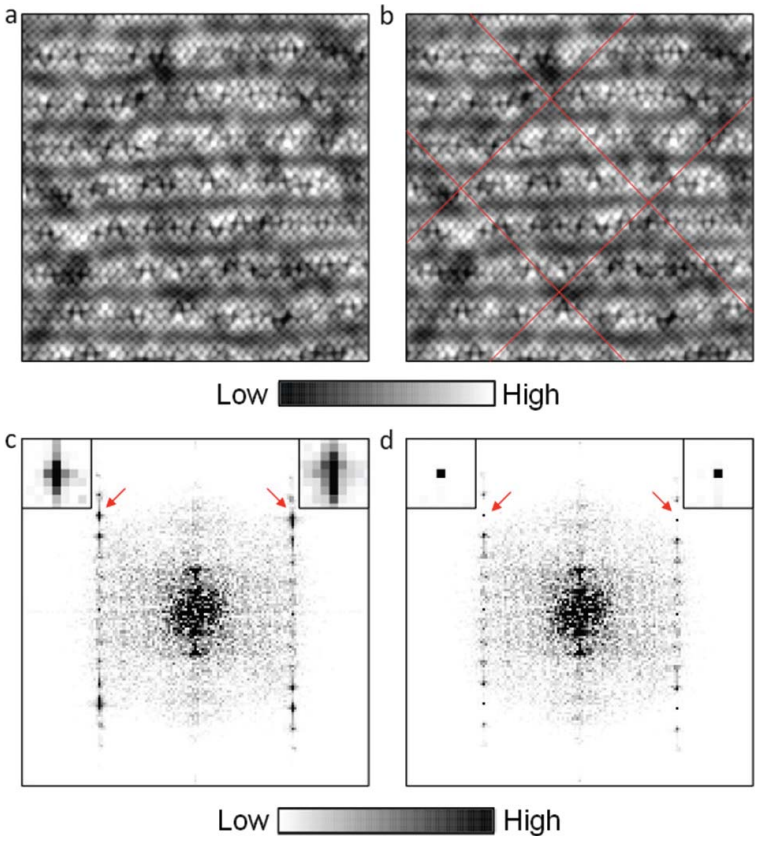


FIGURE 4.8: **Piezo-drift compensation**. (left column) before correction (right column) after correction. The effect of the compensation is hard to recognize from the real-space images, but obvious in the momentum-space maps: the width of the Bragg peaks are reduced from ∼10 pixel to the minimum 1 pixel.

Once $\mathbf{u}(\mathbf{r})$ is determined, any data measured at position $\mathbf{r}$ can be associated with new position $\mathbf{r} - \mathbf{u}(\mathbf{r})$. This applies to both topographic image and the layered LDOS map $g(\mathbf{r}, E)$ simultaneously acquired.

One should note that this scheme is a first-order approximation because of a few reasons. First of all, in this scheme the undistorted positions of each pixel $\tilde{\mathbf{r}}$ is estimated with $\tilde{\mathbf{r}}+\mathbf{u}(\tilde{\mathbf{r}})$ on hand. Removing the effect of the drift requires exact knowledge of

$$\mathbf{u}(\tilde{\mathbf{r}}) = \mathbf{u}(\mathbf{r} - \mathbf{u}(\tilde{\mathbf{r}})) = \mathbf{u}(\mathbf{r} - \mathbf{u}(\mathbf{r} - \mathbf{u}(\tilde{\mathbf{r}}))) = ...$$

which can be precisely determined only if all higher-order terms are included. However, the piezo drift is small compared to the atomic resolution of STM. Therefore

$$\mathbf{u}(\tilde{\mathbf{r}}) \simeq \mathbf{u}(\mathbf{r})$$

in the first order.

Another problem is that the distortion may locally shift the periodicity of the measured lattice whereas the correction scheme above uses reference waves with ideal wavenumbers. But the associated error should be negligibly small up to the first order along with the same reasoning as above.

One example of the distortion compensation procedure is shown in Fig. 4.8. The effect of compensation is not obvious in the real space topographic image, but very clear in the Fourier transformed images. The blurry atomic peaks in Fig. 4.8 (c) marked by the red arrows are transformed into sharp features of single-pixel width.

### 4.3.3 Potential misleading errors

The present analysis reveals the intra-unit-cell anisotropy of a few percent. Any spurious signal or effect that could potentially prefer one direction over the other must be either verified to be absent or systematically removed if present. Potential errors excluded are as follows.

(i) Anisotropic tip - if the shape of the tip apex has a preferred direction, the topography as well as the $Z(\mathbf{r}, e)$ map should have uniform C2 symmetry at all energies. But the topographic images retain C4 symmetry and the strength of the C2 symmetry grows with energy at all four data. Shape of the tip must not have affected the data.

(ii) Scan direction - the raster scanning pattern of STM is a potential source of the C2 symmetry. However, the pseudogap images acquired with R-map at the same area with different scan directions do not show orientation-dependence as shown in Figure 4.9. The scan direction dependence is far less likely to be a problem in $dI/dV$ maps with tens of layers than topography. Because the tip stays for a few seconds at individual measurement

locations such that the average lateral scanning speed is order of $10^{-2}$nm/sec, while order of 10nm/sec in topographic image.

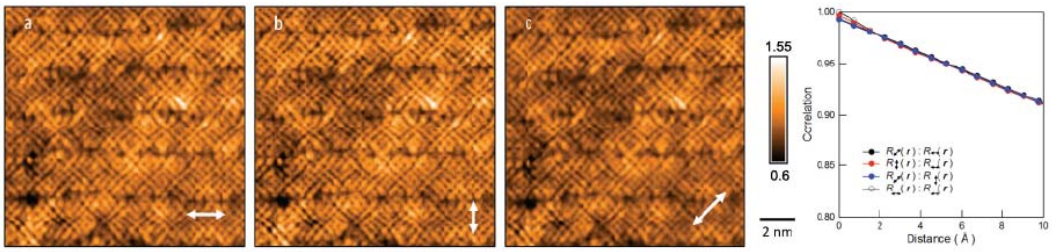


FIGURE 4.9: **Testing the scan direction dependence**. Images of the pseudogap states ($e \sim 1$) with different raster-scan directions (indicated by white arrows) are almost indistinguishable. Identical cross-correlations of the images further confirm the scan direction independence.

(iii) head structure - there are a few parts inside the STM head assembly with C4-symmetry, such as the macor scanner holder and the piezo scanner itself. For some mechanical reason the assumed C4 symmetry of them can be broken. However there are more reasons to refute suspicion. First of all, two different STMs were used to obtain the four data. It is unreasonable to expect that the two STMs have identical head anistropies. Moreover, the BSCCO sample are inserted into the head with no prior knowledge of $a/b$ axes orientation relative to the STM head. Even if the head has a preferred direction, it can hardly break the C4 symmetry of all the four samples uniformly.

(iv) drift compensation error - after the piezo drift is corrected, the atomic registry between $T(\mathbf{r})$ and $Z(\mathbf{r})$ could have been distorted along a specific direction introducing artefact C2 symmetry. However, cross-correlation between every $T(\mathbf{r})$ and $Z(\mathbf{r})$ pairs turned out to be peaked at (0,0).

## 4.4 Broken symmetries

### 4.4.1 Nematic order parameter

Nematic ordering breaks C4 rotational symmetry into C2 making two perpendicular Cu-O bond directions inequivalent. To quantify such inequivalence, one can define an order

parameter which evaluates the differences of modulation intensity with specific wavevectors:

$$\begin{aligned} O_{\rm n}[M] &= \frac{1}{2}[\tilde{\mathbf{M}}(\mathrm{Q}_y) + \tilde{\mathbf{M}}(-\mathrm{Q}_y) - \tilde{\mathbf{M}}(\mathrm{Q}_x) - \tilde{\mathbf{M}}(-\mathrm{Q}_x)] \\ &= \mathrm{Re}\tilde{\mathbf{M}}(\mathrm{Q}_y) - \mathrm{Re}\tilde{\mathbf{M}}(\mathrm{Q}_x) \end{aligned} \tag{4.4.1}$$

where

$$\tilde{\mathbf{M}}(\mathbf{q}) = \mathrm{Re}\tilde{\mathbf{M}}(\mathbf{q}) + i\mathrm{Im}\tilde{\mathbf{M}}(\mathbf{q})$$

is a complex-valued Fourier transform of any $M(\mathbf{r})$ at wave vector $\mathbf{q}$. Here $O_n[M]$ is evaluated at inequivalent Bragg peaks $Q_x = (2\pi/a_0)\hat{\mathbf{x}}$ and $Q_y = (2\pi/a_0)\hat{\mathbf{y}}$ (red circles in Figure 4.10) with Cu sites defined as the origin so that only the real part survives in the above equation. Being calculated at Bragg peaks, this generic order parameter in essence captures the axial inequivalence of the electronic structure at the same spatial periodicity as the underlying crystal lattice.

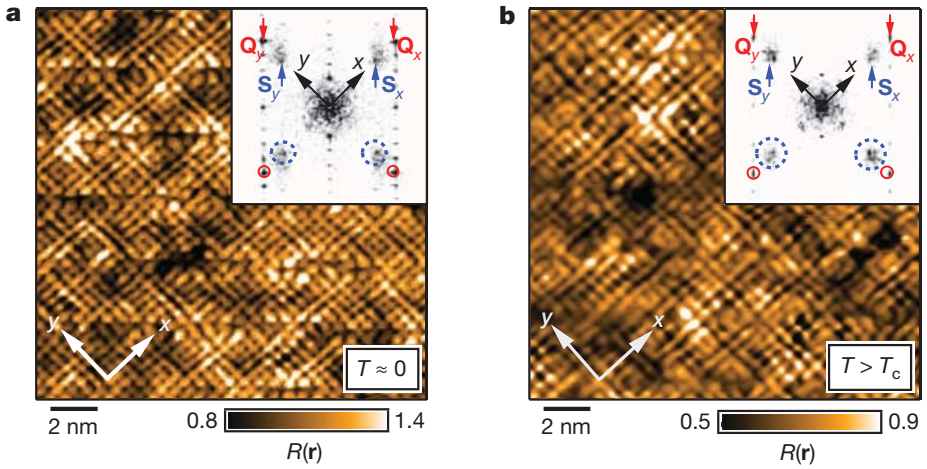


FIGURE 4.10: **Pseudogap in real-space**. Real-space images (R-map) of the pseudogap states $E \approx \Delta_1$ at 4.3K(a) and 55K(b). The broken symmetry is manifest at 55K although the image is not as sharp as at 4.3K due to thermal broadening. Insets show the Fourier-transform where the inequivalent Bragg wavevectors are identified by red arrows and circles. Blue arrows and circles represent the inequivalent 3/4-peaks which turn out to be associated with the possibly smectic ordering. The sizes of the circle is a measure of the coarsening length-scale $1/\Lambda$.

In a simplified ideal lattice in which oxygen atoms lie in the middle of the nearest-neighbor pairs of Cu located on a perfect square grid, it is readily seen that the contribution of Cu

vanishes and only the inequivalence of oxygen atoms are retained, because

$$\tilde{\mathbf{M}}_{\mathrm{Cu}}(\mathbf{Q}_x) = \tilde{\mathbf{M}}_{\mathrm{Cu}}(\mathbf{Q}_y) = \tilde{\mathbf{M}}_{\mathrm{Cu}}$$

and therefore

$$\begin{aligned} \tilde{\mathbf{M}}_{\mathrm{Cu}}(\mathbf{Q}_x) &= \bar{\mathbf{M}}_{\mathrm{Cu}} - \bar{\mathbf{M}}_{\mathrm{O}_x} + \bar{\mathbf{M}}_{\mathrm{O}_y} \\ \tilde{\mathbf{M}}_{\mathrm{Cu}}(\mathbf{Q}_x) &= \bar{\mathbf{M}}_{\mathrm{Cu}} + \bar{\mathbf{M}}_{\mathrm{O}_x} - \bar{\mathbf{M}}_{\mathrm{O}_y} \\ O_{\mathrm{n}}[\mathbf{M}] &= 2(\bar{\mathbf{M}}_{\mathrm{O}_x} - \bar{\mathbf{M}}_{\mathrm{O}_y}). \end{aligned} \tag{4.4.2}$$

The oxygen contribution has plus sign if they come in phase with the Cu, and minus sign if out of phase by 180°. The $\bar{M}$ denotes the average over unit cells. The last line reads that finite order parameter implies inequivalence in the electronic structures at the oxygen sites as depicted in Figure 4.11.

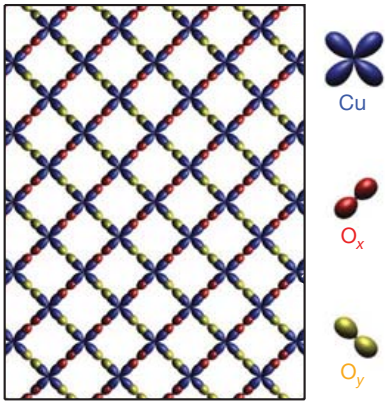


FIGURE 4.11: **Inequivalent oxygen**. In a modified schematic view with C2 symmetry, the two inequivalent oxygen sites within a unit cell leading to a global nematicity are grouped with different colors depending on the relative locations from the Cu sites.

### 4.4.2 Electronic nematicity

In search of the nematic ordering in the underdoped cuprates, atomic resolution topographic images and Z-map with atomic registry were obtained from four $Bi_2Sr_2CaCu_2O_{8+\delta}$ samples of $T_c$ = 20K, 35K, 40K, 55K. The lattice distortion was corrected simultaneously in

both $T(\mathbf{r})$ and $Z(\mathbf{r}, e)$ in reduced energy scale. Then the following momentum-space order parameter normalized by $\bar{Z}(e)$ was evaluated.

$$O_n^Q(e) \equiv \frac{Re\tilde{Z}(Q_y, e) - Re\tilde{Z}(Q_x, e)}{\bar{Z}(e)} \tag{4.4.3}$$

One spectacular contrast immediately follows when the above definition is applied to simultaneous $T$ and $Z$ maps: $O_n^Q$ is negligible in $T$, whereas substantial in $Z$ map. (Figure 4.12 (a) and (b)) In other words, $T$ map does *not* break C4 symmetry while Z map does, or the nematicity is present in the electronic structure in ideal square lattice. More importantly, the nematicity weak at low energy grows monotonously toward the pseudogap energy $\Delta_1$. (Figure 4.12 (c)) This energy evolution demonstrates that the C4 symmetry breaking is a characteristic of the pseudogap phase.

What is the origin of this intra-unit-cell electronic nematicity? Equation 4.4.2 hints at oxygen atoms as one candidate. The inequivalence of the oxygen atoms can be directly investigated with a real-space order parameter:

$$O_n^R(e) \equiv \sum_R \frac{Z_x(R, e) - Z_y(R, e)}{\bar{Z}(e)N} \tag{4.4.4}$$

Here the differences of $Z(\mathbf{r})$ between the oxygen atoms $a_0/2$ away from the Cu atoms along $x$ and $y$ directions are calculated within individual unit cells and averaged over the entire field of view (summation index $R$ denotes Bravais lattice vector). Locations of the oxygen atoms are precisely determined from the distortion-corrected $T(\mathbf{r})$, and the denominator contains the number of unit cell for a FOV size-independent measure.

The $O_n^R(e)$ due to the oxygen thus calculated is almost identical to $O_n^Q(e)$, while the $O_n^R(e)$ by the Cu sites does not change significantly over the entire $0 < e < 1$ range. (Figure 4.12 (f)) This coincidence confirms that $O_n^Q(e)$, thus the reduction of C4 symmetry into C2, primarily stems from the inequivalent oxygen atoms within unit cell, and that the Cu lattice do not break C4 symmetry as assumed in equation 4.4.2. Moreover, the entire observations up to this point is observed universally in all samples with different doping, further corroborating the link between the C4 symmetry breaking and the high-energy pseudogap at 4K.

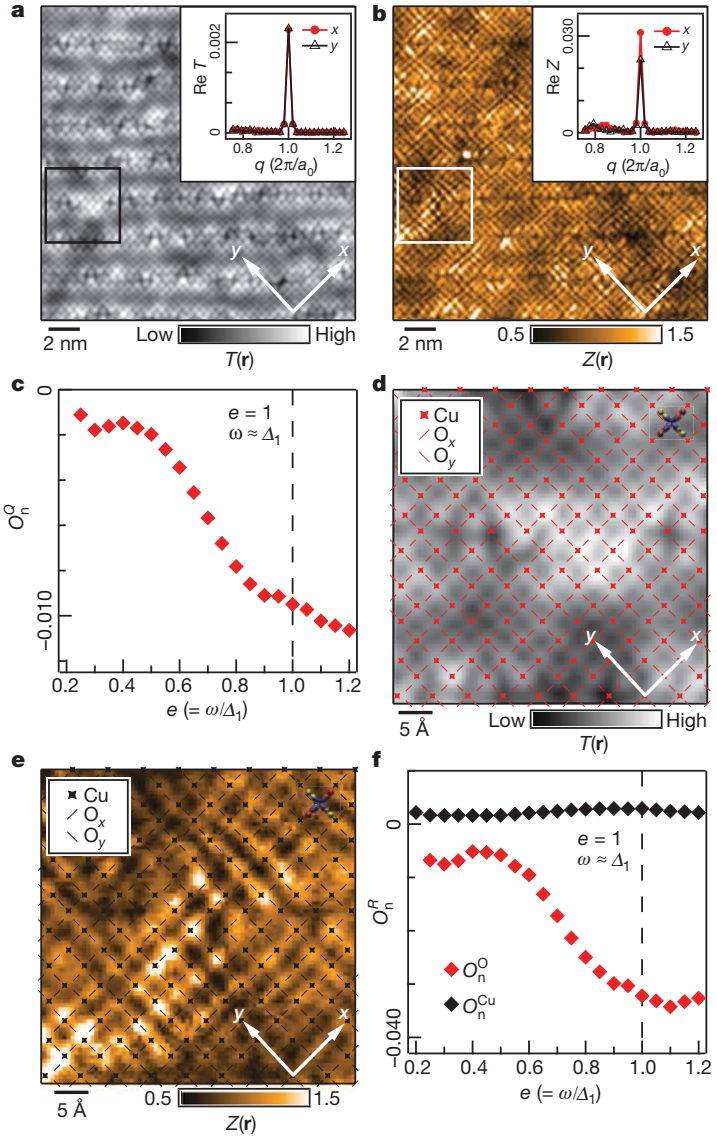


FIGURE 4.12: **Signature of the intra-unit-cell nematicity**. (a) Topographic image $T(\mathbf{r})$ of the $Bi_2Sr_2CaCu_2O_{8+\delta}$ surface. The inset shows that the real parts of the Fourier-transformed image $T(\mathbf{q})$ have comparable magnitude at Bragg points $Q_x$ and $Q_y$ consistent with C4 symmetry. (b) In the $Z(\mathbf{r}, e = 1)$ image, however, the Bragg peaks have different intensity characteristic of the reduced C2 symmetry. (c) The anisotropy of the inequivalent Bragg peaks, or the strength of the nematicity grows with $e$. (d) $T(\mathbf{r})$ in the black square region in (a) is zoomed in. The Cu and O sites are marked by dot and line, respectively. (e) $Z(\mathbf{r})$ in white square region in (b) zoomed in with the same marking scheme for Cu and O sites. (f) $O_n$ by the oxygen sites has energy evolution identical to (c), but $O_n$ due to the Cu sites vanishes independent of the rescaled energy.

### 4.4.3 Smectic structure

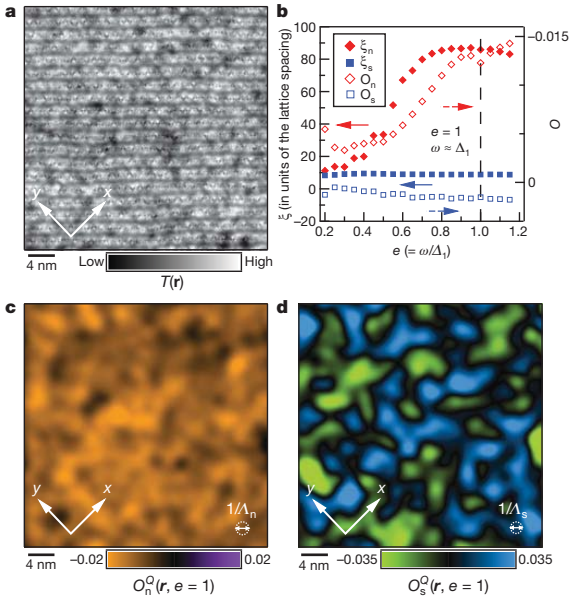


FIGURE 4.13: **Comparison between nematic and smectic arrangements**. (a) Real-space distribution of the nematic ($O_n$) and the smectic ($O_s$) order parameters in the large FOV. The $O_n$ has negative values in the entire FOV (c) implying C2 anisotropy, whereas $O_s$ varies with nearly equal fractions of positive and negative-valued area (d) indicating weak or negligible ordering. Correlation length evolution of the two orders with the reduced energy scale are such that the nematicity becomes more uniform with the $e$, while the smecticity is independent of energy.

Elucidation of intra-unit-cell electronic nematicity evokes search for a close relatives, smectic spatial organization. Because the smectic structure of stripy LDOS modulations sitting exactly on the Cu-O bond (Fig. 4.5) can melt into nematicity according to a number of theoretical proposals.[155,156]

The stripe-like structure evident in the R-map has three intensity peaks over 4-unit-cell distance. This charge ordering could either be associated with $q \sim 3/4(2\pi/a_0)$ or Umklapp-folded $q \sim 1/4$. It must be the former, because the $q \sim 1/4$ wavevectors are from dispersive Bogoliubov QPI at low energy and vanishes at $\Delta_1$ energy scale. We can thus analyze the smectic structure with the following vectors, shown as blue circles in Fig. 4.10:

$$\mathbf{S}_x \equiv (\sim 3/4, 0), \mathbf{S}_y \equiv (0, \sim 3/4)$$

The appropriate measure of the inequivalence between $\mathbf{S}_x$ and $\mathbf{S}_y$ can be defined in a similar manner to the case of nematicity:

$$O_s^Q(e) \equiv \frac{Re\tilde{Z}(S_y, e) - Re\tilde{Z}(S_x, e)}{\bar{Z}(e)} \tag{4.4.5}$$

In a stark contrast to $O_n^Q(e)$, $O_s^Q(e)$ are very small (nearly disordered) with no energy evolution as in Fig. 4.13 (b).

The different characters of the two broken-symmetry phases can be better compared by mapping their spatial fluctuations as in Fig. 4.13 (c) and (d). $O_n^Q(e)$ prefers a direction almost over the entire field of view so that the nematic ising domain is larger than the FOV size. Meanwhile, $O_s^Q(e)$ distribution is almost disordered containing equal proportion of positive and negative regions, implying the absence of (or negligibly weak) ordering in the length scale of the intra-unit-cell nematicity. Plots of the correlation lengths $\xi$ also provide quantitative measure of the spatial fluctuations. $\xi_n(e)$ diverges to the FOV size at $e \approx 1$ while $\xi_s(e)$ does not vary with energy, the latter being consistent with the coexistence of two regions with opposite sign of $O_s^Q(e)$ as big as the order of 10 unit cell.

## 4.5 Concluding remarks

The gradual breaking of the higher C4 into the lower C2 symmetry with reduced energy scale as summarized in Fig. 4.12 (c) can also be visualized in an intuitive real space representation. Based on the precisely determined Cu lattice coordinates, individual unit cell can be sliced and $Z(\mathbf{r})$ within each cell averaged as in Fig. 4.14 in a repeated zone scheme. It is a vivid demonstration of how the C4 electronic structure at low energy breaks symmetry evolving into C2 structure. The existence of the electronic nematicity (and the absence of the smectic contribution) at $E \sim \Delta_1$ in the pseudogap phase is confirmed once again.

This result may provide a new framework that could combine the experimental results by other spectroscopic probes, such as spontaneous circular dichroism by ARPES[147] setting in at $T^*$, magnetic order at the Bragg peaks by polarized neutron diffraction.[82] Many similar C2-type characteristics suggest that all three spectroscopic probes including STM

are observing the same excitation with the same broken symmetries. If that is the case, one can conclude that the C2 rotational symmetry of the pseudogap phase derives from the weak magnetism developed at the inequivalent oxygen sites within $CuO_2$ unit cell.

Unlike the Bragg peaks, the incommensurate modulations associated with the 3/4 peaks do not show significant anisotropy between the two perpendicular bond directions. The smectic structure along each direction will thus be similar to each other and can be separately investigated. In a subsequent study, Mesaros *et al.* discovered that the topological defects present in the smectic modulation for both directions lies at the boundary where the nematic order parameter changes sign.[157] The coexistence of, and the coupling between the nematic and smectic structure in the underdoped cuprates will be an important route to understanding the diverse electronic phases in the HTS and their interplay.

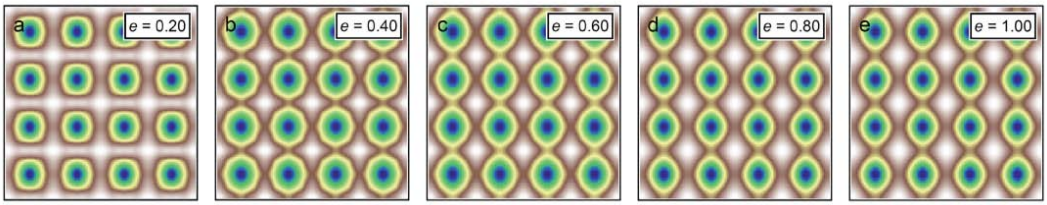


FIGURE 4.14: **C4→C2 evolution of the averaged unit-cell electronic structure**. Distortion-corrected $Z(\mathbf{r}, e)$ is sliced into square patches, averaged over the unit cells, and repeated in 4x4 array for better visualization. The intra-unit-cell Z-distribution exhibits C4 symmetry at small e but evolves toward C2 at higher $e$.

# Chapter 5

# Momentum Space I: Phase-incoherent d-wave superconductivity

## 5.1 Phase fluctuating superconductivity

### 5.1.1 $T_c$ and phase coherence

Superconductivity is a macroscoic phenomenon in which wavefunctions of electron pairs with zero center-of-mass momentum align to form a phase-coherent quantum state. Cooper pairs of electrons are the elementary building blocks, but the existence of pairs alone cannot produce superconductivity until the pairs lock into a single complex macroscopic wavefunction (superconducting order parameter).

The phase stiffness, which is a measure of the energy cost for spatial variation of the phase, is proportional to the density of the paired electron:[158]

$$k_B T_\theta = N_s \hbar^2 / m^*$$

At low temperatures in conventional superconductors, $N_s$ is large and $k_B T_\theta$ is thus a lot higher than the pair-breaking energy. $N_s$ decreases with increasing temperature toward $T_c$, so that the Cooper-pair dissociation and the loss of phase coherence occur at nearly the same temperature.

On the contrary, HTS is characterized by low superfluid density and relatively weak screening permitting greater degree of classical and quantum phase fluctuation, respectively. Strength of the dominating classical fluctuation, proportional to the zero-temperature phase stiffness

$$V_0 = \frac{(\hbar c)^2 a}{16\pi e^2 \lambda^2(0)}$$

of HTS turns out to be orders of magnitude smaller than that of the conventional superconductors. $T_\theta$ is accordingly very small and comparable to $T_c$.[123] As a consequence electron pairs exist above $T_c$ without coherent phase relation, and the superconducting transition is associated with the establishment of phase coherence in the underdoped side of the $p$-$T$ phase diagram.

Order parameter strongly fluctuates near the phase transition in general. For instance, in HTS where $T_\theta$ determines $T_c$, the *phase* fluctuation will be strong near the transition region. The existence of the phase-fluctuating region is evidenced by numerous experimental probes, despite notable disagreement on the designated range.

### 5.1.2 Phase-fluctuating region above the superconducting dome

In this section experimental results that provide evidence in favor of the phase-fluctuation destroying superconductivity are summarized. It should be noted that all data indicate phase-fluctuating region lying just above the $T_c$ curve but well below the pseudogap onset temperature $T^*$ (Fig. 5.1).

1. THz conductivity

   Above $T_c$, the long range phase coherence disappears and its correlation is retained over a small region with strong temporal fluctuation. If the system is driven with oscillating electric field of frequency higher than the inverse of the phase correlation time,

however, the response is not qualitatively different from that of the true superconducting state.[158] The associated phase stiffness temperature decreases with increasing temperatures due to the smaller superfluid density and due to the frequency-dependent dissipation of normal state fluid (in two-fluid model), but is finite up to 25K over $T_c$ implying the existence of the phase-fluctuating state.

2. Nernst effect

   Due to the phase singularity of $2\pi$ at the core, the vortex excitation and its thermally induced motion at finite temperature disturb the phase relation of superconductor. Nernst signal $e_N$ is a measure of the vorticity resulting from both vortices and antivortices. Hence the observation of large Nernst effect well above $T_c$[159] implies that the phase rigidity is unlikely to be retained near $T_c$, so that the superconducting transition occurs due to the loss of phase coherence, rather than due to the loss of superfluid density.

3. Diamagnetism

   The reduction of long-range phase rigidity into local coherence above $T_c$ can be verified with diamagnetism, a signature of superconductivity. With simple and straightforward setup in which torque on a cantilever with HTS mounted at the end at an angle with external magnetic field is measured, Wang *et al.* claims the existence of finite amplitude of superconducting order parameter without bulk phase order over a region above the superconducting dome.[160]

4. Josephson tunneling

   One of the most direct evidence of the existence of the Cooper pair comes from the measurement of the pair tunneling through Josephson junction. By sandwiching $PrBa_2Cu_{2.8}Ga_{0.2}O_7$ weak insulator between $YBa_2Cu_{2.8}Co_{0.2}O_7$ (optimally doped) and $NdBa_2Cu_3O_7$ (underdoped HTS) thin films, Bergeal *et al.* measured pair susceptibility and observed excess conductance 14K above $T_c$ of the underdoped material, indicative of pair remnants.[161]

## 5.2 Experiment

### 5.2.1 Doping level and sample issues

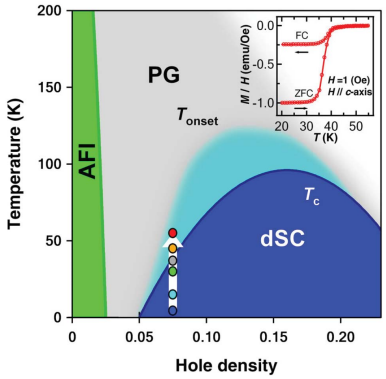


FIGURE 5.1: **Phase diagram**. Pseudogap shows up at intermediate dopings or high temperatures(gray), with phase-fluctuating region above the superconducting dome(light blue). The white vertical arrow and dots indicate the doping level and measurement temperatures for this experiment. (inset) Magnetization curve of the sample with field-cooling(FC) as well as zero-field-cooling(ZFC).

Pseudogap covers very wide region of the doping($p$)-temperature($T$) phase diagram. It spans from near the Mott insulator to the superconducting dome, and from absolute zero to near room temperature depending on hole concentration. Diverse combinations of doping level and the temperature therefore allow access to the pseudogap. In light of numerous efforts to understand the nature of the pseudogap through its relation to the superconductivity, however, it is preferred to measure underdoped cuprates which exhibit both pseudogap and the superconducting state distinctively above and below $T_c$.

In underdoped regime, the superconductivity disappears and only the pseudogap is accessible if samples are heated over $T_c$. But at higher temperatures the thermal stability of STM required for high-resolution momentum-space image is progressively reduced. Moreover, $\sim 4k_BT$ thermal broadening (see Chapter 3) further deteriorates the data quality. Thus the samples with sufficiently low doping level are inevitable choices. All data presented in this chapter were acquired on Dy-Bi2212 (20% of Ca substituted with Dy.) of $T_c$=37K (corresponding to doping level ~7%).

BSCCO samples usually grows to optimal doping (∼16% hole concentration). Once grown, the hole concentration can be increased (decreased) by adding (removing) oxygen with annealing at high (low) pressure oxygen ambience. Much of the superconducting doping levels are achieved this way. But very-low doping requires special technique.

There are at least two methods. One is to extract oxygen from the optimally-doped as-grown samples in the presence of Titanium as catalyst, and the other method is elemental substitution. The former procedure, employed by Genda Gu in Brookhaven National Laboratory, is simpler in that it does not suffer from complication by additional elements introduced. The sample $T_c$ drops to ∼15K from 90K, but the superconducting volume fraction is very small (<10%). This implies that only a small portion of the cleaved surface will be superconducting. The STM tip is very likely to land onto non-superconducting regions. Even worse, there is no knowledge so far about the size of the superconducting region. Good things about the BSCCO samples by Genda Gu are that (i) superconducting area is strongly mixed with non-superconducting area so that we can study the boundary between the two domain as well as the bad metal phase, and (ii) the samples have peculiar cross-shaped dark stripe regions. The latter is interesting in itself, but also helpful in quantifying the thermal drift of the piezo actuator (discussed below).

On the other hand, Prof. Uchida group in Tokyo University uses elemental substitution to reduce $T_c$ further. For the samples used for this thesis 20% of Calcium was substituted with Dysprosium which helps pull electrons out of the two adjacent $CuO_2$ layers. Substitution has proved to reduce $T_c$ down to 20K.[153] Although the introduction of foreign element may complicate the theoretical calculation and understanding, this method does not require oxygen annealing and the superconducting volume fractions are nearly 100%.

### 5.2.2 Modification of STM for high-temperature experiment

The STM, with which all measurements in this thesis were carried out, was previously a dip-in type cryostat with no heating capability. In order to study the pseudogap physics along with the superconductivity the STM had to be upgraded in many ways. Major modifications include the following.

1. Heating unit and thermal feedback

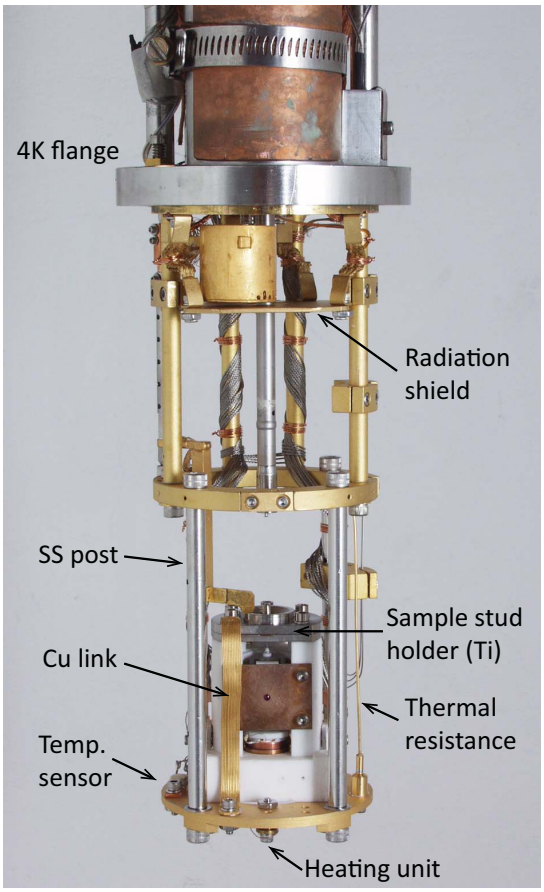


FIGURE 5.2: **Modified STM**. Front view of the STM head assembly after modification for high-temperature measurement. Parts made of OFHC copper were gold-coated.

The first and the immediate component was the heater added at the bottom face of the STM base plate to raise the temperature. (see figure 5.2.) The temperature of the base plate is monitored through a Cernox$^{TM}$4-probe thermometer installed at the plate top, and fed back to the Lakeshore 336 temperature controller which supplies calculated amount of heater output current necessary to maintain the desired temperature.

2. Copper thermal link between the base plate & sample stud holder

   During actual measurement the sample plus sample stud is held tight in a titanium holder. Critical to the experiment is the temperature of this holder, not the base plate where the heater and thermometer are attached. Thus a flexible copper conducting

path is added between the holder and the base plate to match the temperatures. It should be noted that the thermal conductivity of titanium is smaller than that of copper, so that the temperature of the titanium holder could be slightly different from the value on the controller screen. It is thus a best practice to wait for a few hours even after the base plate temperature is stabilized.

It is also of importance to allow thermal conduction only but not electronic conduction, as the base plate and the sample must be at different electric potential. A square sapphire piece is glued at one end of the copper conducting path for this task.

3. SS posts for thermal isolation

   All structural posts below 4K plate of the original STM were made of copper to secure maximal heat conductance from the STM head to liquid helium bath, in order to keep the base temperature as low as possible. The thermal conduction capability had to be reduced for high-temperature measurements because larger heater current is required for maintaining the temperature otherwise. This in turn means that the heat dissipated into the liquid helium bath will be greater, increasing the helium boil-off rate and reducing the available measurement time. Also the larger heater current itself introduces more joule heat to the STM head, which also needs to be minimized.

4. Thermal resistance

   SS posts thermally isolate the STM head stage from the upper structure. This decoupling helps retain the heat for high-temperature measurement, but at the same time delays cooling. As a compromise a narrow conducting channel is added with varying resistance with temperature.

5. Miscellaneous

   The STM base plate was redesigned to thinner version with bigger center hole to reduce thermal mass. It would speed up the response of the system to heating / cooling. And all the coaxial signal cables were tightly wound on the upper copper posts in direct contact with the 4K plate. This will minimize heat introduction through them. A radiation shield baffle was also added just below the cleaving bucket to block heat influx from above the 4K plate.

### 5.2.3 Piezo drift at elevated temperatures

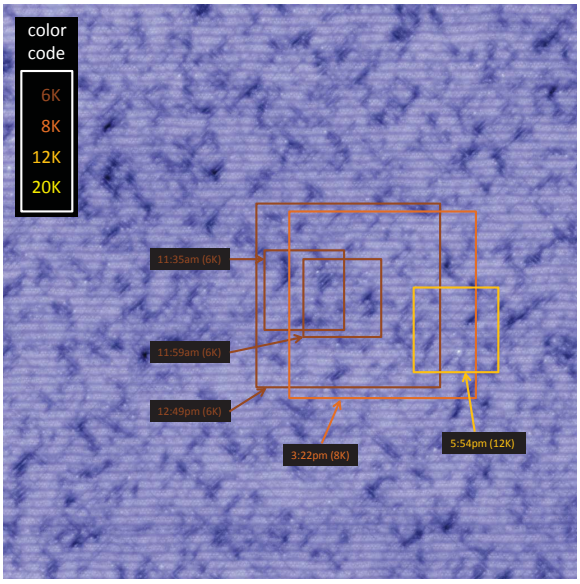


FIGURE 5.3: **Thermal drift of piezo**. Consecutive topographs acquired during the heating test are compared with a very large topographic map to trace how the piezo translates the field-of-view center with temperature. Brighter color indicates higher temperatures - brown rectangles for 6K, orange for 8K, amber for 12K.

Even with all these preparation for measurements at high-temperature, there is an inherent problem left: piezo drift. As a material with ferroelectric property, piezoelectric ceramics exhibit hysteresis and remnant response. Due to the latter phenomena, commonly referred to as drift or creep, the piezo keeps displacing even after the applied voltage stops changing. The piezo creep logarithmically increases with time; slowing down gradually but keeps increasing. The creep rate also increases with temperature; it takes longer for the piezo drift to stabilize within acceptable tolerance at higher temperatures.

On the other hand, obtaining high-quality $dI/dV$ map demands maximum measurement duration of over 100 hours. As the experimental dewar has about 8 days of liquid helium lead time, the maximum temperature was to be set by the requirement that the piezo creep should stabilize within 4∼5 days. It turned out that 55K was the practical maximum. The heater could raise the temperature further, but at the expense of thermal stability. It was

customary to refill the liquid helium, wait for 4∼5 days and then start $dI/dV$ map during measurement above $T_c$.

Figure 5.3 is an example of piezo drift tracing. At first the background topography was obtained over 150nm field of view for a reference map at 4K. An hour after raising the temperature to 6K a few topographs were acquired and placed against the large FOV map. Next the temperature was increased to 8K and 12K. Topos at 8K and 12K were obtained 2.5 hours after the STM temperature stabilized. By following the center of each rectangle, it is evident that the piezo drift occurs along a straight line and that the drift rate is higher at higher temperatures. (The rectangle sizes correspond to the FOV of individual topo; smaller ones over 20nm, larger ones over 46nm nominal.) It should be noted that the dark regions with random sizes and positions characteristic of BSCCO samples provided by Genda Gu were indispensable in following the drift. Being able to trace the direction and speed of the piezo drift suggests the possibility of taking topo and $dI/dV$ map on exactly the same FOV at different temperatures, particularly above and below $T_c$.

## 5.3 Analysis

### 5.3.1 Quasi-particle interference (QPI)

STM measures the spatial variation of local density of state (LDOS), which is proportional to the square of the Bloch wavefunction of Landau quasiparticle characterized by energy E and wave vector **k**:

$$LDOS(\mathbf{r}, E) \propto \sum_k |\Psi_k(\mathbf{r})|^2 \delta[E - \epsilon(\mathbf{k})]$$

In an ideal crystal with no scattering source such as impurity or defects, LDOS is spatially uniform so that STM will see no real-space modulation. In contrast, in the presence of impurities or crystal defects, elastic scattering of the quasiparticles off the imperfection mixes eigenstates of the same energy but of different momenta. This mixing produces standing-wave interference pattern with wave vector given by the difference of the two momenta. Simple superposition principle of elementary quantum mechanics explains the effect:

$$|\Psi|^2 \sim |e^{i\mathbf{k}_1\cdot\mathbf{r}} + e^{i\mathbf{k}_2\cdot\mathbf{r}}|^2 = const + \cos[(\mathbf{k}_1 - \mathbf{k}_2)\cdot\mathbf{r}]$$

Therefore, the Fourier transform of $|\Psi|^2$ or $LDOS(\mathbf{q}, E)$ will give peaks at $\mathbf{q} = \pm|\mathbf{k}_1 - \mathbf{k}_2|$ in the momentum-*transfer*($=\mathbf{q}$) space. FT-STS can resolve only up to the momentum difference, not the momenta of individual QPs.

### 5.3.2 Electronic band structure with d-wave gap

According to the BCS theory, superconductivity sets in the Fermi liquid when the material is cooled below $T_c$. The emergence of the new order modifies the underlying electronic structure of the system: superconducting gap opens in the normal state band near the Fermi energy. Bogoliubov quasiparticle(BG QP) properly describes the fundamental excitations of the superconducting ground state in the presence of the gap. The dispersion of the BG QPs accordingly incorporates both the normal state band and the energy gap $\Delta(\mathbf{k})$

$$E_{\pm}(\mathbf{k}) = \pm\sqrt{\epsilon(\mathbf{k})^2 + \Delta(\mathbf{k})^2}.$$

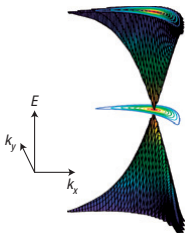


FIGURE 5.4: **Quasiparticle excitation near Fermi energy**. Below $T_c$, the modified low-energy QP excitations due to the $d$-wave superconducting gap is centered at the nodal direction and the chemical potential.

The BCS theory was developed for and successfully describes conventional superconductivity. It is now widely accepted, however, that the BCS theory can be extended to HTS by using the anisotropic $d$-wave gap. When a gap of $\Delta(\mathbf{k}) \sim [\cos(k_x) - \cos(k_y)]$ form opens in a single hole-like band about the BZ corners,[126,162,163] the electronic band structure turns into a sombrero shape as in Fig. 5.4.

Slices of the above dispersion at different energies give banana-shaped contour of constant energy (CCE) where QPs are well-defined. Wavevectors connecting any two points on the CCE should appear on the FT-LDOS map in principle. A great deal of simplification

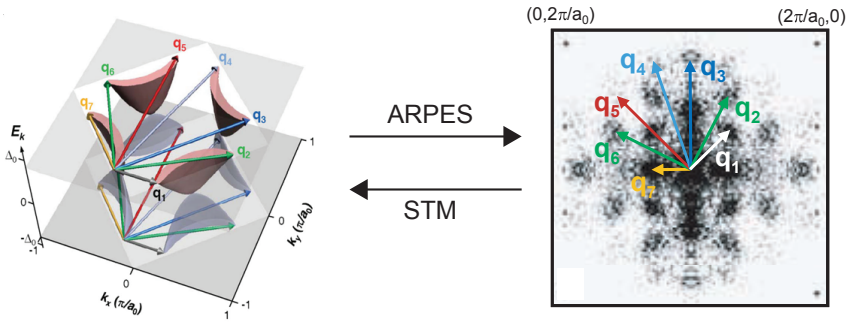


FIGURE 5.5: **QPI vectors connecting banana tips**. (left) Arrows represent distinct wavevectors connecting the tips of banana-shaped CCE, corresponding to the peaks in Fourier-transformed LDOS map (right). In reverse, single electron band dispersion can be determined from the $g(\mathbf{q}, E)$. ARPES measurement obtains the left structure which translates to the right, whereas STM data yields the right structure that can be converted to the left. Note that the 45° rotated crystallographic axes.

comes in, however, from the fact that the QP density of state is inversely proportional to the gradient of the dispersion:

$$\frac{dE}{dk} \sim \frac{1}{|\nabla E(\mathbf{k})|}$$

As a consequence the QPs are concentrated near the tip of the banana. From the 8 symmetric banana tips ('octet' structure) only 7 distinct QPI vectors are defined. (see Fig. 5.5)

If one of the octet banana tips have momentum $\mathbf{k}_B(E) = (k_x(E), k_y(E))$, momentum space location of the other seven symmetric tips as well as the seven wavevectors connecting them are determined from simple geometric relations:

$$\begin{aligned}
\mathbf{q}_1 &= (2k_x, 0) \\
\mathbf{q}_2 &= (k_x + k_y, k_y - k_x) \\
\mathbf{q}_3 &= (k_x + k_y, k_y + k_x) \\
\mathbf{q}_4 &= (2k_x, 2k_y) \\
\mathbf{q}_5 &= (0, 2k_y) \\
\mathbf{q}_6 &= (k_x - k_y, k_y + k_x) \\
\mathbf{q}_7 &= (k_x - k_y, k_y - k_x)
\end{aligned}$$

In practice the relations are inverted; $(k_x(E), k_y(E))$ are determined from the locations of the q-vectors.

The strength of individual QPI peaks depends on the scattering rate between the two QP states given by the Fermi golden rule:

$$W_{i,f} = \frac{2\pi}{\hbar}|\langle\psi_{\mathbf{k},i}|V|\psi_{\mathbf{k},f}\rangle|n_f(E)$$

Because QPI peak intensity is proportional to the initial state DOS times the scattering rate, and because the latter is proportional to the final state DOS, QPI map essentially shows the distribution of the joint density of states (JDOS) in momentum-transfer space. The JDOS can be directly compared with auto-correlation of the spectral weight distribution A(**k**, w) obtained by ARPES, which match very well to each other.[164,165] This octet QPI framework proved to be successful in understanding HTS.[148,153]

### 5.3.3 Data processing

A number of post-processing steps are required to extract high-quality QPI dispersion from the raw LDOS(**r**, E) map, in the following order.

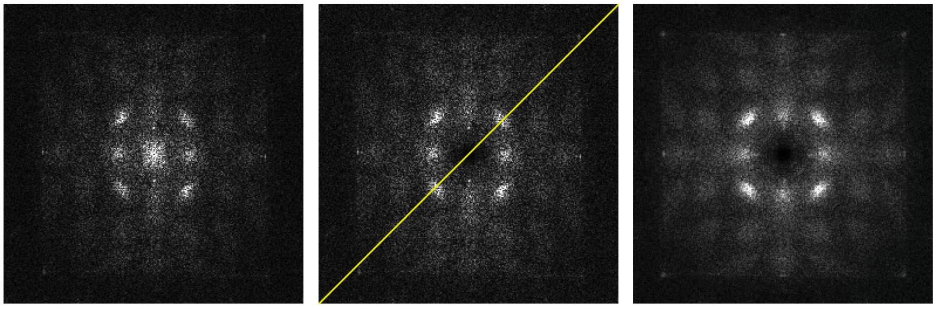

FIGURE 5.6: **Post-processing**. White blobs represent QPI vectors. LDOS(**q**, E) maps are shown before (left) and (middle) after core removal. The atomic peaks in the middle image are slightly off the yellow diagonal line. (right) after unwarping the data into a square shape and symmetrization operation.

1. Ratio map[87,129,166]

Tunneling currents of STM are determined by two factors: tip-sample distance and integrated density of states. (see Chapter 3) In the constant-current mode, the latter must be location-independent for the differential conductance to purely represent the LDOS. In HTS such as BSCCO this requirement does not hold. The spatial variation of the tip-sample distance affects the measured $dI/dV$ data. Taking the ratio of either the differential conductance at opposite biases reduce the 'set-point effect', and therefore should be the first step in post-processing:

$$Z(\mathbf{r}, V) = \frac{g(\mathbf{r}, +V)}{g(\mathbf{r}, -V)}$$

The ratio map suppresses the checkerboard-like modulation, amplifying the particle-hole symmetric BG QP component.

2. Core removal

   The strongest feature in the Fourier-transformed Z-map is the peak at the center ($q \sim 0$) representing the long-wavelength variation, or averaged background of the real-space data. The center peak needs to be removed if the weaker QPI peaks are to be better resolved. In practice, core can be removed by multiplying the FTed-$Z$ maps with inverted 2D-Gaussian, or equivalently, subtracting Gaussian average in the real space.

3. FFT

   The energy of quasiparticle excitations disperses in momentum space. Converting the real-space map into momentum-space counterpart with (Fast) Fourier Transform is thus a crucial step. 46nm nominal FOV usually gives reasonable resolution in both real and momentum space (see Chapter 3).

4. Squarize

   Due to the C4 symmetry of the underlying crystal structure, the four Bragg peaks associated with the atomic array are ideally expected to form a square. $Z(\mathbf{q}, \mathrm{E})$ map readily shows that this is not true primarily because of the continual piezo drift during 100+ hours of measurement. Mixed with raster-scanning motion of the tip, the aspect ratio of the $Z(\mathbf{q}, E)$ map turns out to be slightly off unity. ImageInterpolate operation

in Igor adjust the FTed image so that the four Bragg peaks lies exactly on the q-space diagonal in a square shape.

5. Symmetrize

   Squarization stretches the map into square shape but is not sufficient to impose true 4-fold symmetry to the data. Folding the map horizontally (or vertically) and diagonally turns all data point C4-symmetric as well as increases signal-to-noise ratio.

6. Bad pixel removal

   Each QPI peak position is to be determined with Gaussian fitting, for which artifact outliers can be detrimental. It is therefore helpful to remove data points that lies far away from the average.

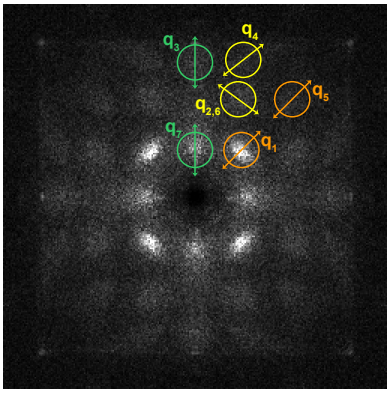


FIGURE 5.7: **QPI movement direction**. $q_1$ and $q_5$ ($q_3$ and $q_7$) move along the vertical (diagonal) direction, while $q_2$, $q_4$ and $q_6$ do not have such restricted geometry. The former four can be best fitted with 1D Gaussian, but 2D Gaussian fitting is the only option for the latter three.

7. Extracting QPI peaks

   Momentum-space position of a QPI peak can be determined with either 1D or 2D Gaussian. When using 1D Gaussian, the 2D peak data are first projected and integrated into 1D distribution, and then the 1D profile is fitted with 1D Gaussian. The two methods are to give the same results for the ideal case where the peak is isotropic about the center.

In actual $Z(\mathbf{q}, E)$ map, after all the post-processing described above, QPI peaks are usually elliptical, far from isotropic. For $q_1$, $q_3$, $q_5$, and $q_7$ peaks that disperse along the axes of crystal symmetry (Fig. 5.7), the choice of projection line is straightforward and 1D Gaussian determines the peak position along the axes. The other peaks with dispersion not along a straight line are traced with 2D Gaussian (Fig. 5.8). The heights of the individual Gaussian peak are interpreted as the intensity of the peak.

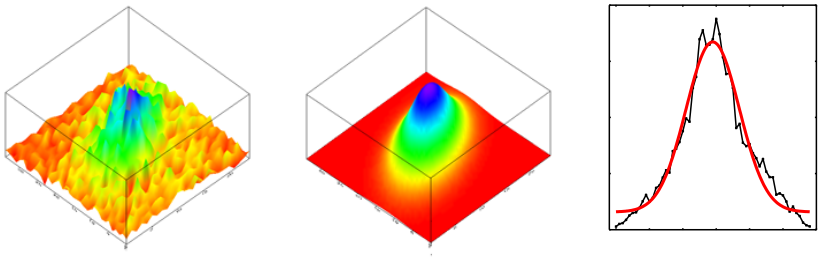

FIGURE 5.8: **1D vs. 2D Gaussian**. A QPI peak (left) is fitted with 2D Gaussian (middle). Or the data points can be projected onto a high-symmetry direction (diagonal for $q_1$, for instance) and then summed. The integrated data can be fitted with 1D Gaussian function.

## 5.4 Results

The present experiment was carried out on $Bi_2Sr_2Ca_{0.8}Dy_{0.2}CuO_{8+\delta}$ ($T_c$=37±3K) sample grown by floating-zone scheme. Sample is inserted into STM and cleaved in-situ under cryogenic UHV environment to reveal atomically flat BiO surface. Differential conductance maps were taken at six temperatures from 4.5K to 55K (∼1.5$T_c$), individually over 100+ hour duration. All maps were taken on the same sample for three months span except for 45K. 46nm square nominal FOV (actual size 50∼55nm) are resolved into 256×256 real space data points over -34mV to +34mV energy range.

Representative differential conductance maps for six temperatures after post-processing are shown in Figure 5.9. It is apparent that the QPI peak dispersion at the lowest temperature is maintained qualitatively when the temperature increases past $T_c$ up to 1.5$T_c$. The validity and the internal consistency of the octet model extending into the pseudogap regime is

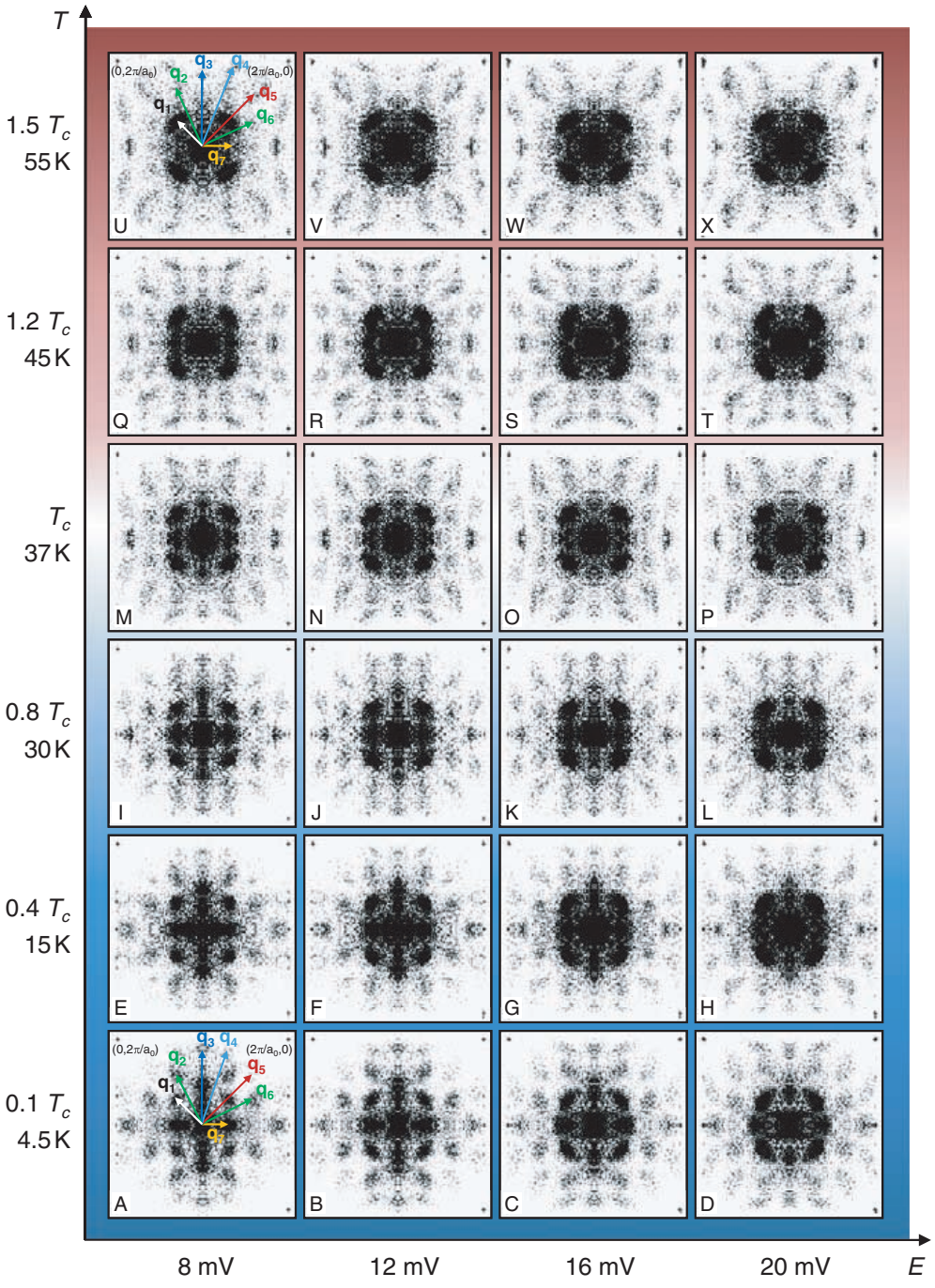


FIGURE 5.9: **Temperature evolution of $Z(\mathbf{q}, E)$.** The Fourier-transformed LDOS ratio map is shown in energy-temperature grid array. The QPI patterns between $T_c$ and $1.5T_c$ are indistinguishable from those below $T_c$.

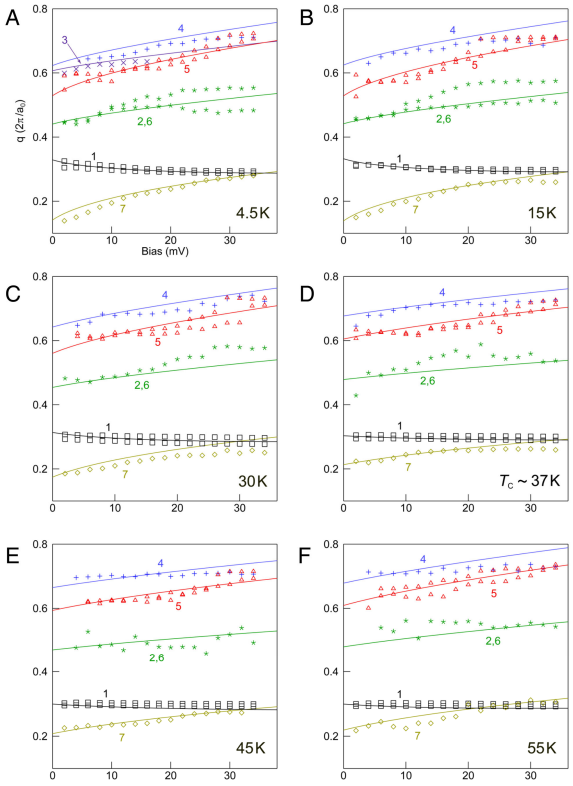


FIGURE 5.10: **Validity of the octet model**. The actual dispersion of QPI peaks (symbols) is compared with those predicted by octet model (solid curves). The validity of the octet model is further confirmed at all measurement temperatures.

further confirmed at each temperatures against the combination of quarter-circle Fermi surface and a model $d$-wave gap function (Fig. 5.10)

$$A(T)\cos(2\theta_k) + B(T)\cos(6\theta_k).$$

Owing to the consistency of the octet model and the QPI dispersions up to $T \sim 1.5T_c$, the k-space position of the banana tip $\mathbf{k}_B(E)$ and the $d$-wave gap function $|\Delta(\mathbf{k})|$ can be determined at different temperatures. Figure 5.11 shows the $\mathbf{k}_B(E)$ profiles projected onto the quarter-circle Fermi surface. The low-energy dispersion can be clearly divided into two distinct regions: (i) sizeable Fermi arc around the node even at the lowest temperature,

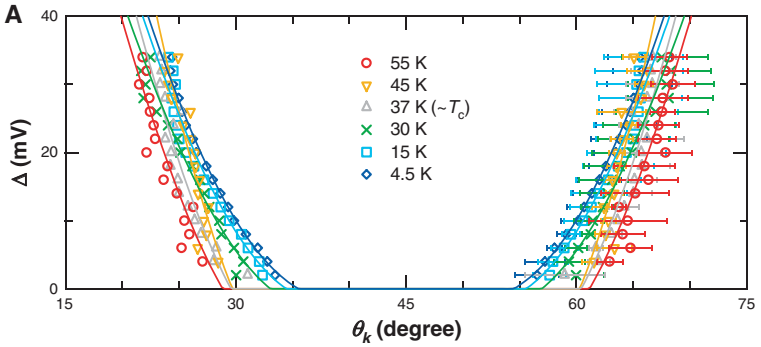


FIGURE 5.11: **The electronic excitation structure**. The positions of $\mathbf{k}_B(E)$ deduced from the QPI peaks are plotted on a Fermi-surface angle vs. Energy plane. Sizable zero-energy excitation (Fermi arc) is observed, accompanied by d-wave gap on both sides.

whose length grows with temperature (ii) $d$-wave gap which does not converge to a single (nodal) point.

One very important point is that the above characteristics are common to all temperatures reported; the electronic excitation structure for $T_c < T < 1.5T_c$ is not qualitatively different from that below $T_c$. Both observations are in stark contrast with ARPES measurement which states that the superconducting order parameter converges to the nodal point at all temperature below $T_c$, with zero-energy excitations available only at the node.

One of the immediate consequences of the finite length of the Fermi arc is that the zero-bias (differential) conductance should be finite. The point $dI/dV$ averaged over the entire FOV readily confirms the relation. (Fig. 5.12) The differential conductance at zero bias is finite even at the lowest temperature, linearly increasing with temperature, consistent with the growth of the Fermi arc length as in Fig. 5.11.

Tracking the magnitude variation only of the QPI vectors with energy greatly advanced our understanding on the cuprate electronic structures by showing that swath of PG region close to the superconducting dome evolves from superconductivity without pronounced change with temperature. Analysis of the intensity of the individual peak reveals, in contrast, that the energy and temperature evolution of QPI peaks can be divided into two subgroups depending on the relative signs of the order parameters of the initial and final state as in Figure 5.13. Intensity variations of $q_2$, $q_6$, $q_7$ which connect regions of opposite sign

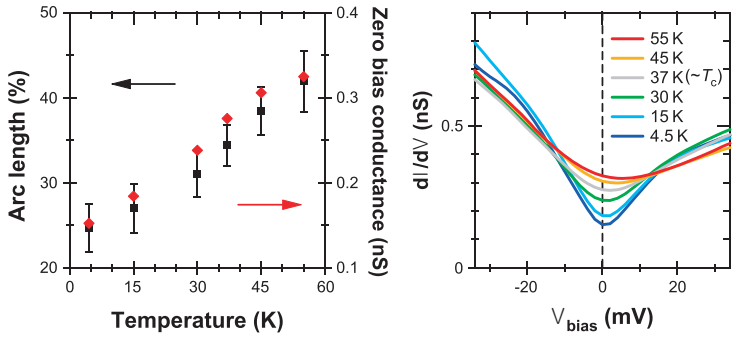


FIGURE 5.12: **Zero-bias conductance**. (left) Fermi arc representing zero-energy excitations is substantially long even at the lowest temperature. The length of the arc grows linearly with increasing temperature. (right) Zero-bias conductance and its linear growth is also evident in the tunneling spectra averaged over all data point.

gradually decreases with increasing temperatures, while those of $q_1$, $q_4$, $q_5$ which involve no sign flip do not show significant temperature evolution. This distinction is believed to come from the difference of the scattering mechanism.[167]

## 5.5 Conclusion

The above experimental observations elucidate the electronic structure of of the pseudogap regime of the strongly underdoped cuprate in the vicinity of the superconducting transition. First, octet QPI, a definite spectroscopic signature of the *d*-wave superconductivity, remains to be valid up to $1.5T_c$ with no qualitative change in superconducting transition. Thus the region just above the superconducting dome on the underdoped side is most likely to represent an extension of the properties below $T_c$, in support of the phase-fluctuation scenario in which the Cooper pairs exist without long-range phase coherence.

In fact, the fluctuating superconductivity immediately above $T_c$ seems to be a generic characteristics common to HTS. The signature of the remnant superconductivity is observed virtually at all doping in diverse compounds such as underdoped Hg1201,[168] overdoped LSCO,[169] YBCO in both under and over doping regime,[170] single-layered Bi2201,[171] and also in Fe-based superconductors.[172] No less diverse experimental probes also report evidence

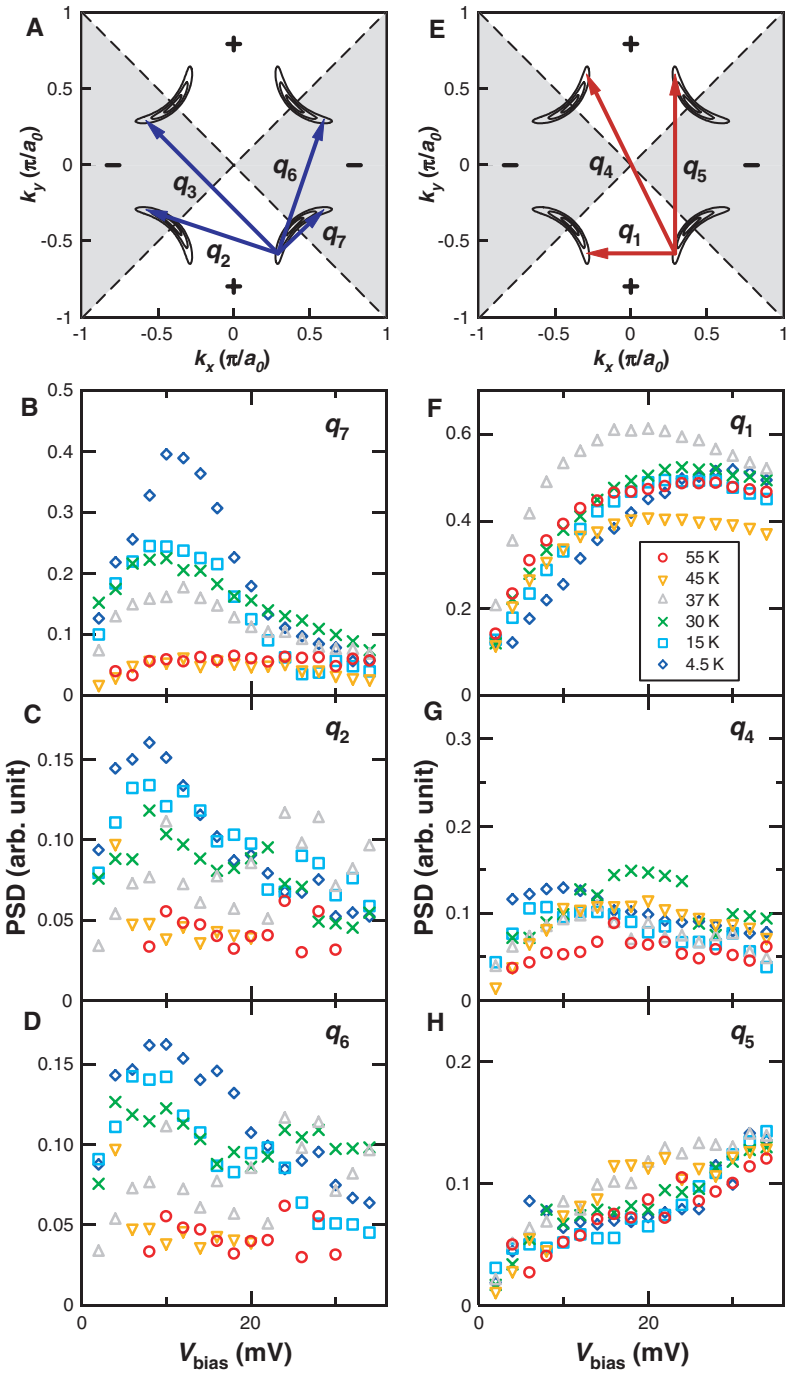


FIGURE 5.13: **Order parameter sign combination**. QPI peaks are divided into two groups, depending on whether the scattering connects regions of the same sign of the superconducting order parameter or opposite sign. Energy dispersion of the former peaks has strong temperature dependence gradually diminishing with temperature, whereas the other peaks do not vary significantly.

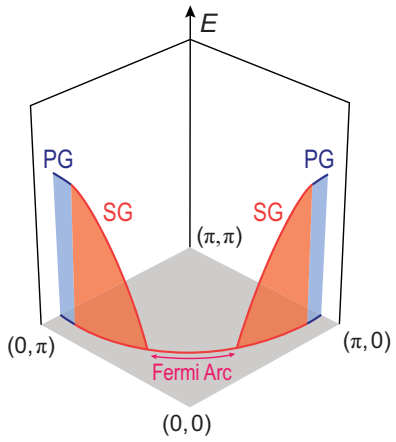


FIGURE 5.14: **Schematic electronic structure**. The electronic structure of the strongly underdoped cuprate system are composed of three distinct regions : (1) the finite and evolving Fermi arc around the nodal direction (2) *d*-wave superconducting gap (3) symmetry-broken pseudogap state at high energy.

for the phase fluctuation above $T_c$, such as Raman spectroscopy,[168] magneto-transport,[169] microwave absorption,[170] ARPES,[171] Andreev reflection measurement,[172] and intrinsic Josephson tunneling.[173]

Secondly, the current QPI($T$) study reveals that the pseudogap regime of strongly underdoped cuprate contains three, not two, elements : (i) Fermi arc, (ii) particle-hole symmetric d-wave gap opening near the node, (iii) non-dispersive and symmetry-breaking excitations at higher energies as summarized in Fig. 5.14.

# Chapter 6

# Momentum Space II: Dispersive Checkerboard

In cuprate HTS, the *checkerboard* refers to the real-space grid-like electronic density of states modulation of 4∼6 unit cell period. Although observed universally in STM/ARPES-friendly cuprate compounds such as BSCCO and Na-CCOC, the checkerboard modulation (CBM) oriented along the Cu-O bond direction has been studied so far not as intensively as the superconducting order parameter. With growing research interest on elucidating the nature of the pseudogap as well as its relation with the *d*-wave superconductivity, understanding the CBM will be an important key as it is believed to originate from the anti-node.

## 6.1 Battle on the checkerboard

The checkerboard structure of quasi-particle states was first observed inside the vortex core of OD89K Bi2212 under 5T magnetic field[174] and subsequently claimed in OD86K Bi2212 at zero field.[175] Both STM measurements were, however, carried out below 10K, deep inside the superconducting dome. Soon afterwards similar local ordering was also observed in UD80K Bi2212 with 100K measurements, in the absence of magnetic field, implying its pseudogap origin.[176]

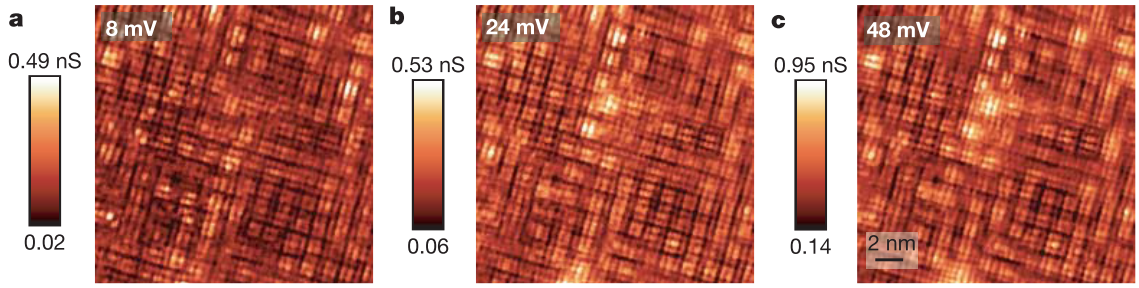


FIGURE 6.1: **Checkerboard modulation.** Bias-independent inhomogeneous periodic real-space pattern is clearly observed in the DOS maps of $x$=0.10 $Ca_{2-x}Na_xCuO_2Cl_2$ obtained in the same field of view.[88]

In the following year the CBM was reported in lightly-doped Na-CCOC[88] (Fig. 6.1). Momentum-resolved investigation found that weak anti-nodal states can give rise to the local ordering,[177] providing potential evidence of their pseudogap origin. Both studies point toward almost non-dispersive charge ordering at low energy.

Subsequent experiments not only expanded the portion of the phase diagram and material in which CBM and/or anti-nodal charge order is sought after but also provided conflicting results, as summarized below in the order of publication.

1. McElroy *et al.* discovered CBM at high energy in ZTPG(Zero Temperature PG)-masked regions[152] of UD65K Bi2212, emergence of which coincides with the decoherence of the anti-nodal states. The CBM-related $q^*$ weakly disperses, although the authors describe it as nondispersive.

2. Chatterjee *et al.* reported non-dispersive $q^*$ wavevector by auto-correlating ARPES data from UD76K Bi2212 obtained at 90K.[164] By comparing with the auto-correlation of the center-cropped data, the authors suggest that $q^*$ comes from the Fermi arc tip, instead of the anti-node. They also claim the absence of charge order based on the absence of the expected shadow band.

3. Hanaguri *et al.* observed CBM in Na-CCOC near optimal doping ($T_c$=25∼28K),[166] while the main focus was to suppress the CBM in favor of the BG QPI.

4. Wise *et al.* reported CBM in Pb-Bi2201 compound.[178] Variation of the associated wavevector with doping but not with energy or temperature is interpreted as evidence for CDW origin of pseudogap. However, only positive-side data were presented.

5. Ma *et al.* probed La-Bi2201 with both ARPES and STM. They claim "nondispersing" charge order wavevector,[179] but do not provide data for their conclusion.

6. Parker *et al.* has shown that the near quarter peak in q-space below $T_c$ in UD35K Dy-Bi2212 does disperse, and is equally strong above $T_c$ surviving substantially up to $3.5T_c$.[69] The authors also present dispersive $q^*$ obtained from UD84K Bi2212, in direct contradiction with their previous result.[176]

7. Meng *et al.* traced the doping evolution of the anti-nodal Fermi surface nesting vector with ARPES measurements on UD18K / UD21K / OP27K / OD20K NCCOC, covering most doping range including overdoped side.[180] The authors claim weak dispersion near optimal doping but no dispersion in the underdoped side. But the data in the underdoped regime shows finite dispersion as discussed later.

Apparently there is no consensus on the CBM-related investigation; whether the q-vector associated with CBM disperses or not, and which part of k-space it comes from are not clear, both of which may help determine whether there is charge ordering in the anti-node or not. Even worse, the doping / temperature range in which CBM exists is not clearly determined. In this chapter I present experimental data of Bi2212 at different doping and temperature which can provide answers to these questions as well as new perspectives in the CBM study.

## 6.2 Raw vs. Ratio map

Quantum interference of Bogoliubov quasi-particles has proved to be a legitimate window to investigate the cuprate superconductivity. In nearly optimally doped Bi2212, Fourier-transformed LDOS map $g(\mathbf{q}, E)$ readily reveals seven distinct dispersive QPI peaks consistent with $d$-wave excitation gap. In contrast, in cuprate compounds of relatively low $T_c$ such as strongly underdoped Bi2212[181] or Na-CCOC,[166] the octet BG QPI is revealed clearly

in opposite-bias ratio map $Z(\mathbf{q}, |E|) = g(\mathbf{q}, +E)/g(\mathbf{q}, -E)$ where the CBM is strongly suppressed. Understanding the CBM therefore requires analysis on non-ratio $g(\mathbf{q}, E)$ instead, at the expense of the setpoint effect elimination described in the previous chapters. Numerous theoretical attempts to remove the setup effect *a posteri* without taking ratio of any quantities have all failed, but a few of them are summarized in Appendix C for future reference. It should thus be noted that the data presented in this chapter are not free from the setup effect.

## 6.3 Near-quarter diagonal peaks in q-space

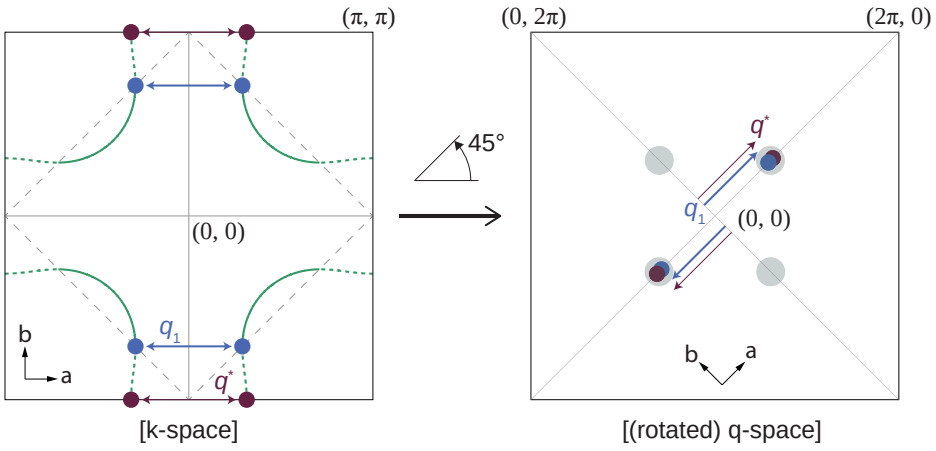


FIGURE 6.2: **Merging peaks.** The $q_1$ wave vector from the superconducting octet QPI (blue) and the $q^*$ connecting the anti-nodal states (brown) merge into a single large peak (grey) in rotated q-space, as both are parallel to the Cu-O bond direction marked with perpendicular arrows. Note that equivalent peaks should be present on the other diagonal.

In real-space, distinguishing the CBM from spatial modulation associated with BG QPI is almost trivial. CBM is recognized by definition with square lattice of tens of nm length scale, while BG QPI modulation has much less ordered modulations. However, the distinction is less clear in momentum space because the primary wavevector for CBM almost coincides with $q_1$ of the BG QPI.

QPI geometry demands that the momentum-trasnfer wavevectors along the Cu-O bond direction contribute to a peak lying on the diagonal in 45° rotated $q$-space. In other words,

the broad peak about one quarter Bragg peak magnitude away from the center should reflect not only the superconducting $q_1$ connecting the octet banana tips (Fig. 5.5) but also $q^*$ that could be coming from the anti-nodal states (see Fig. 6.2). Therefore one needs to examine the diagonal cut of $g(\mathbf{q}, E)$ to see how the strengths of $q_1$ and $q^*$ compare. Note that the $q^*$, not to be confused with $q_1$, is the primary focus in the discussion below.

## 6.4 Dominance reversal with doping at low energy

An interesting aspect of the CBM found in the literature is that the CBM dominates the non-ratio $g(\mathbf{r}, E)$ map in the entire doping, in HTS of low maximum $T_c$ such as NCCOC / Bi2201.[88,166,178] One hypothesis is that the dominance of CBM is due to the weaker superconductivity in these compound. In materials with higher $T_c$ such as Bi2212, the CBM may dominate the low-doping side only, giving way to superconductivity in the higher doping regime. This section investigates how the relative strengths of the CBM and superconductivity compare at different doping.

Diagonal cut of raw $g(\mathbf{q}, E)$ obtained from strongly underdoped to slightly overdoped Bi2212 is collected in Fig. 6.3. $T_c$ higher than 65K were achieved by post-annealing the as-grown samples under different oxygen concentrations, whereas underdoped single crystals with $T_c$ below 65K were grown with Dy substituting 20% of Ca. Differential conductance maps were all obtained at 4K, and diagonal cuts were extracted with identical procedures and parameters: (1) core suppression with 10-pixel width 2D Gaussian (2) unskewing and squarization so that the Bragg peaks are located at (10, 10) and (246, 246) of 256×256 pixel array (3) 15-pixel width integration perpendicular to the diagonal.

From the bias symmetry about the Fermi energy (horizontal bisector of each image panel), it is evident that *p-h* symmetric $q_1$ dispersion in accordance with the *d*-wave gap dominates the low energy spectra of samples with the highest $T_c$ as observed in Fig. 6.3 (d) and (e). In this doping range, the magnitude of the $q_1$ vector disperses very rapidly over narrow energy range, consistent with smaller $\Delta_0$ and longer Fermi arc length,[153] whereas $q^*$ beyond $\Delta_0$ disperses much less as previously reported by McElroy *et al.*[152] for $T_c$=65K Bi2212.

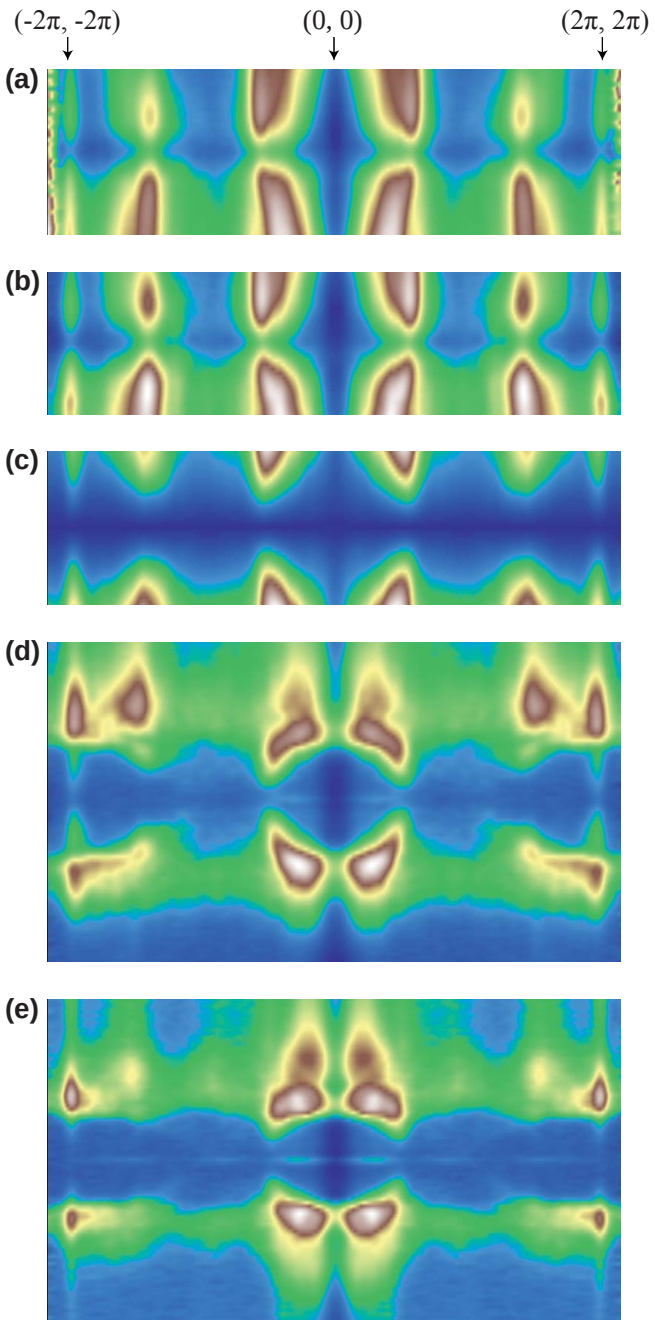


FIGURE 6.3: **Diagonal cut of Bi2212 $g(\mathbf{q}, E)$ at different doping.** Horizontal (vertical) axis is for momentum (energy). $T_c$ and energy ranges (to scale) are (a) UD20K, ±40mV (b) UD37K, ±34mV (c) UD45K, ±36mV (d) UD74K, ±90mV (e) OD86K, ±90mV. All data were obtained at 4K.

In contrast, Fig. 6.3 (a) and (b) reveal that a weakly dispersive asymmetric branch $q^*(E)$ dominates the central region of the diagonal cut in strongly underdoped samples, taking the place of $q_1$ at low energy. $T_c$=45K data in Fig. 6.3 (c) is hard to tell because the dispersion slope is similar to the lower doping side but the energy range is too narrow to decide symmetry or asymmetry. The crossover at this doping seems to correlate with the suppression of the anti-nodal coherence peak[115,182] which occurs between $T_c$ of 40K and 50K (Fig. 2.9), and the lower doping boundary ($p \sim 0.076$, $T_c \sim 40$K) of the tri-sected superconducting dome[183] reported very recently.

Dominance of the $q^*$ and its distinction from $q_1$ is quantitatively verified in Fig. 6.4 (I) which compares the dispersion of asymmetric $q^*$ against symmetric $\mathbf{q}_1$ obtained from the $Z$-map in $T_c$=37K sample. The two branches almost converge at high positive bias, but $|\mathbf{q}^*|$ gradually deviates off the symmetric $q_1$ with decreasing bias. It should be noted that the dominant $q^*$ in strongly underdoped compounds exhibits asymmetry in that it weakly disperses mostly below the Fermi energy, while barely dispersive above. This aspect will be further discussed later.

## 6.5 Anti-nodal origin

Fourier-transformed LDOS map $g(\mathbf{q}, E)$ is a momentum-auto-correlated data.[164] It compiles all pairs of momentum eigenstates with fixed difference into one data point representing the difference vector. QPI signals originating from different part of the Brillouin zone can't be disentangled, provided that each pair has the same difference. Due to this *partial* momentum resolvability of FT-STS, determining the **k**-space location for a QPI peak is a delicate task except for some cases such as $d$-wave octet QPI as discussed in Chapter 5. For asymmetric dispersion $q^*$ dominant in strongly underdoped regime, fortunately, there are a few experimental clues in favor of anti-nodal origin:

1. The real-space CBM in lightly doped NCCOC[88] is shown by ARPES to be originating from the anti-nodal states.[177]

2. Vershinin *et al.* has observed the $\sim 5a_0$ periodic charge ordering in the pseudogap phase of slightly underdoped Bi2212.[176] Parker *et al.* further reported charge ordering

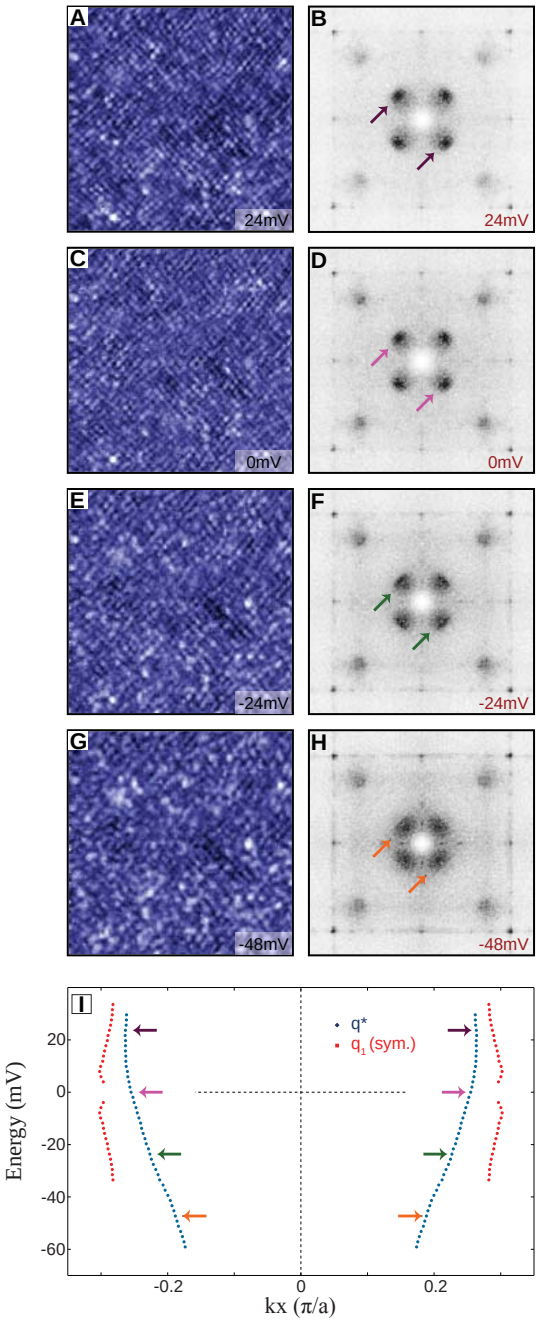


FIGURE 6.4: **Asymmetric anti-nodal dispersion in pseudogap phase.** Differential conductance map in real space (left column) and their respective Fourier transform (right column) in the pseudogap phase of strongly underdoped Dy-Bi2212 ($T_c$=37K) at 55K ($\sim 1.5T_c$). Anti-nodal QPI ($q^*$) dominates the real-space LDOS. The momentum space peaks monotonously disperse through the Fermi energy (blue), a few of which are indicated by arrows of matching colors. Symmetric dispersion of octet $q_1$ at 4K [181] is plotted in red for comparison.

peak $q \sim 1/4$ (in unit of $2\pi$) below $T_c$ in strongly underdoped Bi2212 surviving up to $\sim 3.5T_c$.[69] As pseudogap forms near the anti-node, the presence of these peaks above $T_c$ implies that the antinodal states account for the charge ordering.

3. Wise *et al.* demonstrated that the doping evolution of the charge ordering wave vector is qualitatively consistent with that of the anti-nodal nesting vector of the theoretical Fermi surface.[178]

4. McElroy *et al.* observed that the emergence of $q^*$ associated with CBM at low doping coincides with the decoherence of anti-nodal states.[152]

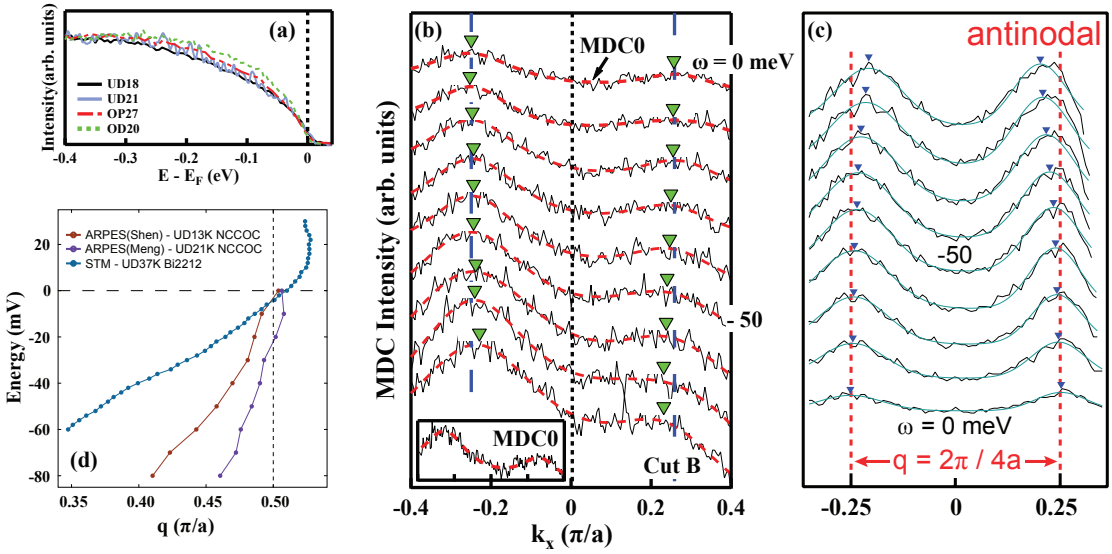


FIGURE 6.5: **Anti-nodal quasiparticle dispersion.** (a) ARPES Energy Distribution Curve (EDC) cuts of underdoped NCCOC near antinode has broad peak extending to 0.4eV binding energy at all doping. Spectral weight at the Fermi energy is order of magnitude smaller than at high energy. But the MDC cuts reveal finite peaks starting from zero binding energy as in (b)[180] and (c).[177] Green curves and blue inverted triangles indicating peaks were overlaid in (c). Note that the binding energy increases in opposite directions - downward in (b) and upward in (c). (d) $q^*$ expected from the ARPES MDC peaks in (b) and (c) are plotted against that determined with FT-STM (see Fig. 6.4 (I)). MDC peak positions from both sides of center line ($k_x$=0) were averaged for (d).

One immediate issue in claiming anti-nodal origin of $q^*$ in underdoped regime is potential conflict with ARPES measurements. As apparent in EDC cuts near the anti-node, spectral

gap develops below $T^*$ such that the low-energy anti-nodal QP spectral weight is very small (see Fig. 6.5 (a)) to account for the $q^*$ dispersion. However, MDC cuts present different view. Despite spectral weights an order of magnitude smaller at low compared to high energy, anti-nodal MDC cuts parallel to the zone face reveal definite peaks mirror-symmetric about $k_x$=0[177,180] (see Fig. 6.5) with k-space separation very close to the $q^*$.

It could be that these weak peaks and its dispersion cannot be resolved with collection of EDC, or were not of interest in the anti-nodal ARPES study. As a matter of fact, anti-nodal ARPES analyses in the literature strongly prefer EDC with major focus on primary features such as broad peaks (high-energy pseudogap) or leading edge midpoints (low-energy pseudogap). The two data reproduced in Fig. 6.5 were essentially all anti-nodal MDC cuts published so far.

Shen *et al.* state "insensitivity to $\omega$ below 50mV", but quantitative re-analysis of the MDC cut shows definite anti-nodal dispersion starting from zero binding energy and becoming less steeper (smaller $dE/dk$) below 30mV as in Fig. 6.5 (c) and (d). This interpretation is more consistent with the asymmetric $q^*$, less consistent with the energy-independence of earlier STM data.[88] The slope of the dispersion is different from that of $q^*$ in Bi2212 (Fig. 6.5 (d)), maybe due to the difference in the band structure of the two material, but it is interesting to observe that the wavevectors at zero energy nearly coincide at 1/4.

It should be noted that these ARPES data were all obtained from NCCOC; more direct comparison can only be made with either higher-resolution $g(\mathbf{q}, E)$ map on NCCOC[1] or anti-nodal MDC cut on strongly underdoped Bi2212.

## 6.6 Temperature evolution of the $q^*$

The real-space LDOS modulation in strongly underdoped Bi2212 is seen to be dominated by charge ordering associated with dispersing anti-nodal states. What about the temperature dependence of the $q^*$? To answer to this question, the same data set as those used in Chapter 5 are revisited, this time without taking opposite-bias ratio. Diagonal cuts for

[1] Note that the near quarter peaks in Hanaguri *et al.*[166] are not sharply defined, because of the real-space field of view size is not sufficiently big to guarantee momentum space resolution.

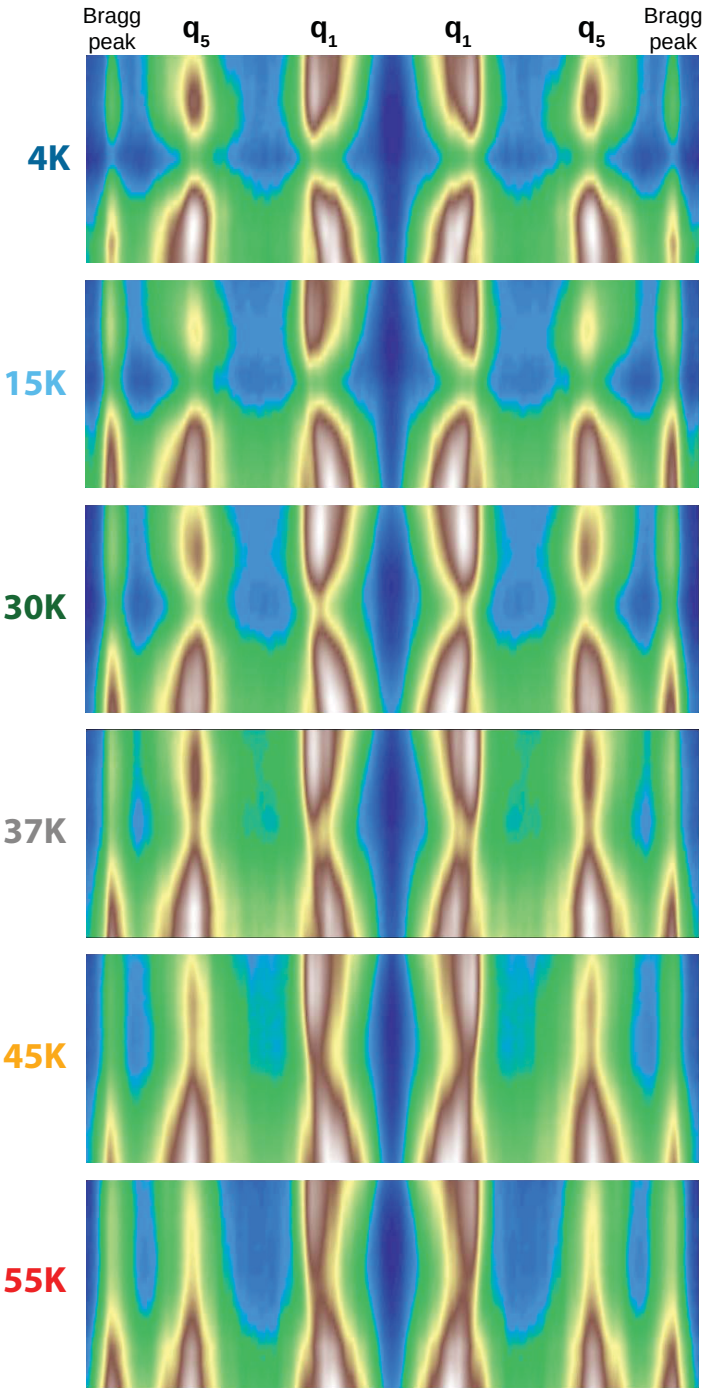


FIGURE 6.6: **Temperature evolution of the CBM.** Diagonal cut of $g(\mathbf{q}, E)$ for $|E|$ <34mV of UD37K Bi2212. Measurement temperature labels are consistently color-coded.

4K to 55K measurement on UD37K Bi2212 are shown in Fig. 6.6. The procedures and paremeters for the cuts are identical to those for Fig. 6.3.

In Fig. 6.7, the magnitude dispersion and the height variation of the anti-nodal charge ordering peak $q^*$ contained in Fig. 6.6 are plotted. The magnitude dispersion shows little temperature variation, pretty much in line with the weak temperature dependence of $\Delta(\mathbf{k})$ determined with Z-map.[181] In other words, $q^*$ above $T_c$ can't be distinguished from below $T_c$ only with magnitude. Meanwhile, the peak height variation shows qualitative difference between above and below $T_c$ unlike that of $q_1$ in $Z$ map (Fig. 4F of Lee *et al.*[181]). The V-shaped gap of $d$-wave superconductivity about the chemical potential below $T_c$ is significantly attenuated above $T_c$, resulting in nearly flat spectral weight distribution. In addition, the temperature independence of the $q^*$ dispersion past $T_c$ is another evidence that $q^*$ is associated with the pseudogap, implying its anti-nodal origin.

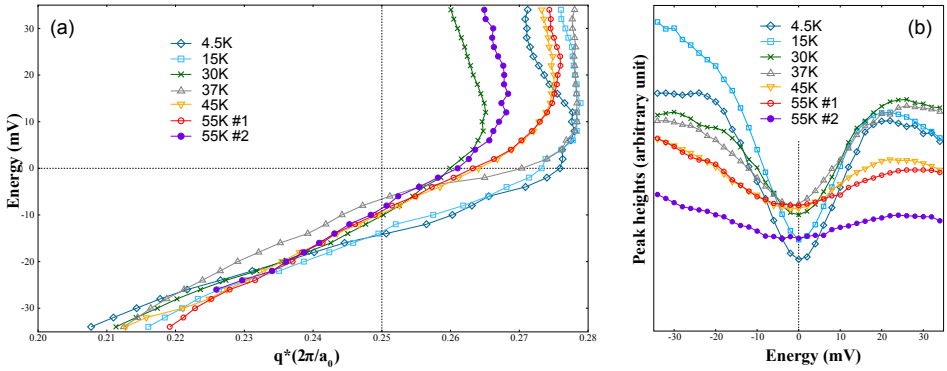


FIGURE 6.7: $q^*$ **of UD37K Bi2212 from 4K to 1.5$T_c$.** (a) Magnitude dispersion and (b) Intensity variation of the anti-nodal charge ordering peak $q^*$ in Fig. 6.6 is summarized. Note the narrow horizontal scale in (a).

One other interesting temperature-independent trait is that $q^*$ disperses linearly mostly below $E_F$, while barely dispersive or bent slightly to smaller $|\mathbf{q}|$ values. This asymmetric dispersion through $E_F$ is also observed in the diagonal cut of $T_c$=20K data (Fig. 6.3). In higher doping, the low-energy dispersion is dominated by $q_1$ BG QPI peak so that the shape or even the presence of $q^*$ cannot be readily determined.

Yazdani group's data[69] show similar doping and temperature dependence of near-quarter peak as ours (see Fig. 6.8). The peak dispersion becomes linear well above $T_c$ at all doping,

but the dispersions near or below $T_c$ show marked difference between lightly-doped and near-optimally-doped regime. At the lowest temperatures, symmetric $q_1$ dominates UD84K and OD91K data but asymmetric dispersion is clear in UD35K, consistent with our results. In all three cases, the QPI above $E_F$ undergoes more rapid change (from negative to positive dE/dk) than below $E_F$. Note that the transition past $T_c$ is gradual, not abrupt.

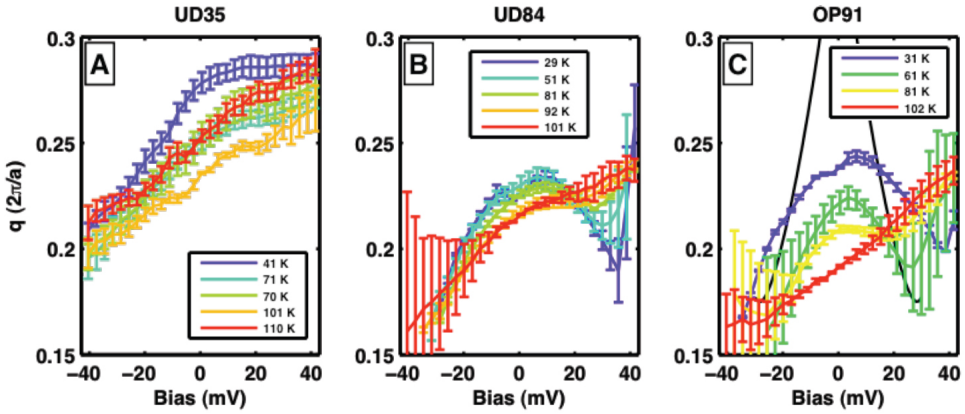


FIGURE 6.8: **Near-quarter peak in Bi2212 by Parker *et al.*** (A) Asymmetric $q^*$ dispersion dominant near $T_c$ evolves into linear dispersion. (B and C) Near optimal doping, symmetric $q_1$ below $T_c$ gradually evolves into linear $q^*$ with increasing temperature.

Temperature evolution in their UD35K data can be directly compared with that of our UD37K data. According to Fig. 1 (a)/(d)/(g) of their paper they must have data below $T_c$ but do not show the dispersion. It could be that the dispersion is identical below 41K as ours. The only overlap, 41K data, however, definitely exhibits asymmetric dispersion closely matching our data in terms of both the slope and the wavevector at the Fermi energy. In short, the two measurements with STM of different group, on Bi2212 samples grown by different people produces identical results.

## 6.7 Dispersive checkerboard

Compilation of the LDOS data in Bi2212 with those in Bi2201 and NCCOC suggests that the dominance of CBM correlates with $T_c$ independent of chemical composition: the low-energy electronic structure of the compounds with low $T_c$ (say, below ∼40K) is dominated

by CBM, while those with higher $T_c$ (above ∼60K) is dominated by the BG QPI. The superconductivity in the former group is probably not strong enough to overcome the CBM. Evidently, the CBM can be best studied with deeply underdoped Bi2212 of sufficiently low $T_c$.

The *p-h* asymmetric dispersion of the $q^*$ near $E_F$ uniformly observed up to $1.5T_c$ is of particular importance, because it is in stark contrast with other experiments mostly revealing non-dispersive $q^*$ which are interpreted in the perspective of charge density wave (CDW). Before disproving the CDW origin in the next section, revisiting literature for $q^*$ is in order.

First of all, Vershinin's report on the non-dispersive wavevector[176] is incorrect. It is superseded by the dispersive one (red curve in Fig. 6.8 (B)) obtained by the same group, with similar sample $T_c$ and measurement temperature.

Two other STM experiments report non-dispersive near-quarter wavevector. The older one by Hanaguri *et al.*,[88] however, shows peaks not sufficiently sharp for fitting due to the limited momentum space resolution. The more recent report by Wise *et al.* shows definitely non-dispersive[178] peaks. But both papers present data above $E_F$ only. Non-dispersive peak above chemical potential agrees well with $q^*$ from UD37K Bi2212 as shown in section 6.6.

On the other hand, the ARPES measurements on NCCOC at the anti-node show definite dispersion as presented in Fig. 6.5 (d). Slopes mismatch between NCCOC and UD37K Bi2212 data, but ARPES data do reveal dispersion that corresponds to the occupied state portion of $q^*(E)$. Both the nearly non-dispersive STM data above $E_F$ and the weakly dispersive ARPES data below $E_F$ are consistent with the *p-h* asymmetric dispersion. In other words, the two data sets nicely consolidate into the the *p-h* asymmetric dispersion in Fig. .

Incidentally, the dominance of BG QPI, and / or the absence of anti-nodal charge ordering of Bi2212 near optimal doping, refutes the interpretation of Howald *et al.*[175] claiming the observation of CBM. As the octet-QPI dominates real space LDOS in those doping regime, Gaussian filtering around near-quarter peak will only reveal $4a_0$ Fourier component of BG QPI, not the CBM.

## 6.8 Invalidating the CDW origin of the pseudogap

When significant portion of the Fermi surface are parallel, 1D or 2D metallic system are unstable against the formation of a periodic modulation of both electron density and ionic lattice below a certain temperature.[184] This instability introduces energy gap at momenta where the original metallic band crosses its shadow translated by the wave vectors of the super structure, lowering the total energy of the system. The effect of the 2D checkerboard-like CDW on the normal state can thus be examined with band mixing by the near-quarter wave vector of the $T_c$=37K Bi2212 along both bond directions, based on the attempt by Li *et al.*[185]

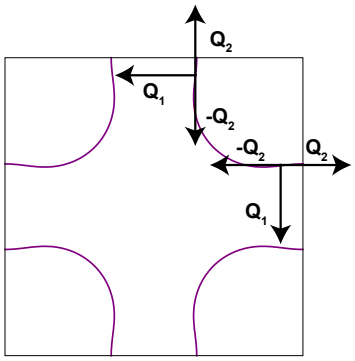


FIGURE 6.9: **Band-mixing CDW vectors.** Wavevectors associated with checkerboard CDW, which are responsible for band shift and mixing. Initial states in the first quadrant is shown only.

With CDW vectors for the first quadrant of the Brillouin zone (Fig. 6.9)

$$\mathbf{Q}_1 = -(2\pi/4, 0), \quad \mathbf{Q}_2 = (0, 2\pi/4) \quad \text{for} \quad k_x < k_y$$
$$\mathbf{Q}_1 = -(0, 2\pi/4), \quad \mathbf{Q}_2 = (2\pi/4, 0) \quad \text{for} \quad k_x > k_y,$$

the system can be described by the Hamiltonian

$$\hat{H} = \sum_{\mathbf{k},\sigma} \Psi^{\dagger}_{\sigma}(\mathbf{k}) \hat{A}(\mathbf{k}) \Psi_{\sigma}(\mathbf{k})$$

where

$$\Psi^{\dagger}_{\sigma}(\mathbf{k}) = (c^{\dagger}_{\mathbf{k},\sigma}, c^{\dagger}_{\mathbf{k+Q}_1,\sigma}, c^{\dagger}_{\mathbf{k+Q}_2,\sigma}, c^{\dagger}_{\mathbf{k\text{-}Q}_2,\sigma})$$

and

$$\hat{A}(\mathbf{k}) = \begin{pmatrix} \epsilon_{\mathbf{k}} & S_0 f_0(\mathbf{k}) & S_1 f_0(\mathbf{k}) & S_2 f_0(\mathbf{k}) \\ S_0 f_0(\mathbf{k}) & \epsilon_{\mathbf{k+Q}_1} & 0 & 0 \\ S_1 f_0(\mathbf{k}) & 0 & \epsilon_{\mathbf{k+Q}_2} & 0 \\ S_2 f_0(\mathbf{k}) & 0 & 0 & \epsilon_{\mathbf{k\text{-}Q}_2} \end{pmatrix}.$$

The normal state band is given by $\epsilon_{\mathbf{k}} = t_0 + (t_1/2)[\cos(k_x) + \cos(k_y)] + t_2[\cos(k_x)\cos(k_y)] + (t_3/2)[\cos(2k_x) + \cos(2k_y)] + (t_4/2)[\cos(2k_x)\cos(k_y) + \cos(k_x)\cos(2k_y)] + t_5[\cos(2k_x)\cos(2k_y)]$ with hopping parameters (in unit of eV) $(t_1, ..., t_5)$ = (-0.5951, 0.1636, 0.0519, 0.1117, 0.0510)[162] and $t_0$=0.002 adjusted for the Fermi surface of $T_c$=37K Bi2212. CDW order parameters $S_0 = \Delta_c, S_1 = s\Delta_c, S_2 = s\Delta_c$ with $\Delta_c$=30meV and s=0.2 ($\mathbf{Q}_2$ coupling weaker than $\mathbf{Q}_1$ nesting) were used, along with the form factor $f_0(\mathbf{k}) = \cos(k_x) - \cos(k_y)$. The electronic structure modified by the presence of CDW can be traced with the requirement $\mathrm{Det}[\omega I - A(\mathbf{k})] = 0$, or equivalently,

$$A(\mathbf{k},\omega) = -\frac{1}{\pi} G_{11}(\mathbf{k},\omega) = -\frac{1}{\pi}\left[(\omega + i\Gamma)I - A(\mathbf{k})\right]^{-1}\Big|_{11}$$

in which $\Gamma$ represents energy broadening of 10meV. Joint density-of-states (JDOS), calculated by the auto-correlation (AC) of the quasi-particle spectral weight $A(\mathbf{k},\omega)$ can be compared with the actual $g(\mathbf{q}, E)$ QPI data.[165]

Fig. 6.10 illustrates how the checkerboard-like 2D CDW modifies the QPI pattern, particularly along the Cu-O bond directions. It is evident that the electronic structure is strongly distorted by the presence of CDW. The parabolic inner branch (panel A) is affected in such a way that the dispersion is replaced by a non-dispersive flat vertical part characteristic of CDW (panel D), about the energy in which the momenta of the original dispersion is about the expected $2\pi/4a_0$. As a consequence, the energy range for the dispersion distortion, which turns out here to be roughly between $E_F$ and $E_F$-80mV, is determined solely by the energy location of the van Hove singularity (vHs), for the same CDW wavevector, or equivalently by the doping level in the rigid band picture.[186] More importantly, the energy range

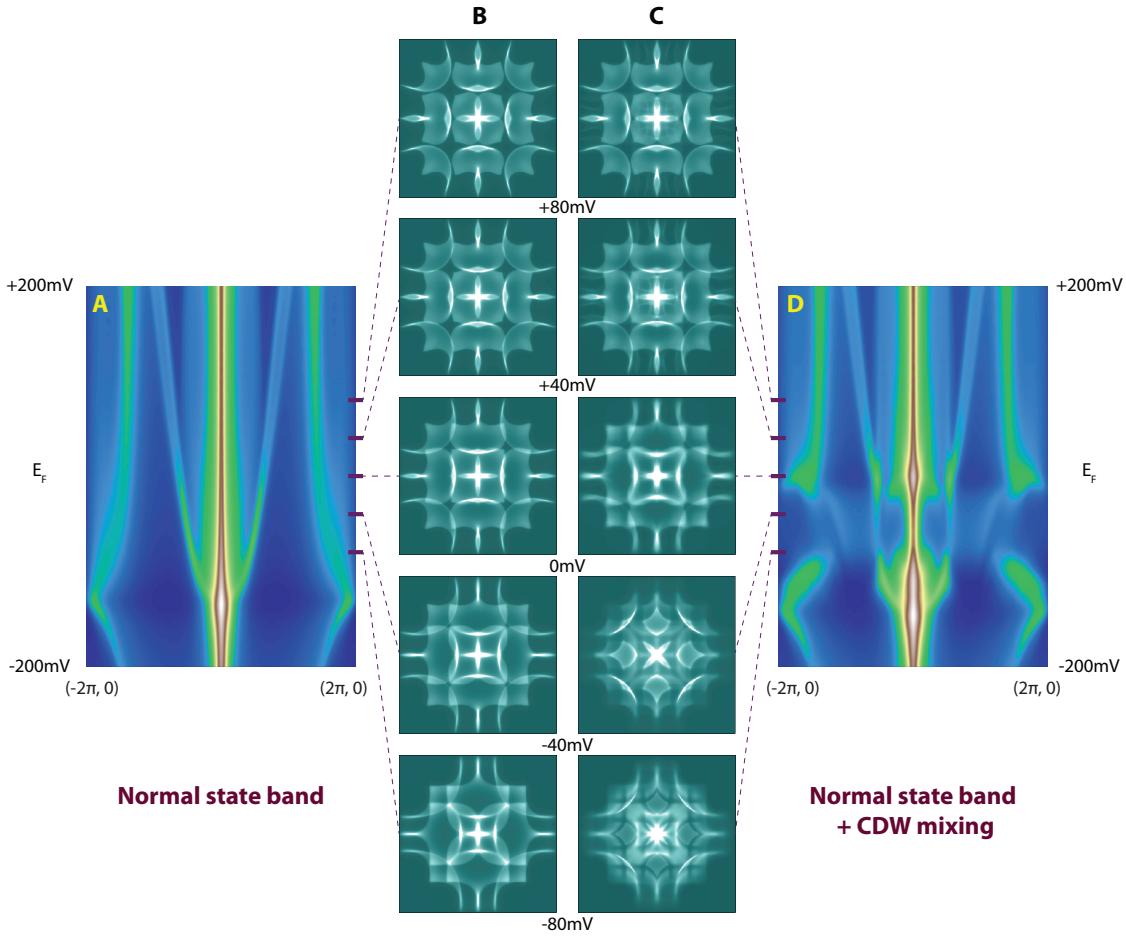


FIGURE 6.10: **Effect of CDW on QPI.** Joint-DOS (JDOS) evaluated from the auto-correlation of the theoretical QP spectral weight $A(\mathbf{k}, \omega)$ are compared between with (C, D) and without (A, B) the presence of CDW on top of normal state band. Column B and C are JDOS slices at different energies spanning from $-2\pi$ to $2\pi$ for both axes. A and D are the linecuts of JDOS along $(-2\pi,\ 0)$ to $(2\pi,\ 0)$. Van Hove singularity is evident near -130mV in A. CDW strongly distorts JDOS over 80mV range below $E_{\mathrm{F}}$ such that the near-quarter peak is almost non-dispersive. The distortion and its energy range are also clearly seen in the layer-by-layer comparison (B, C).

of the flat portion is not centered about the Fermi level in general. Changing the strength of the CDW ($\Delta_c$) will change the energy range only, with the mid-point unchanged.

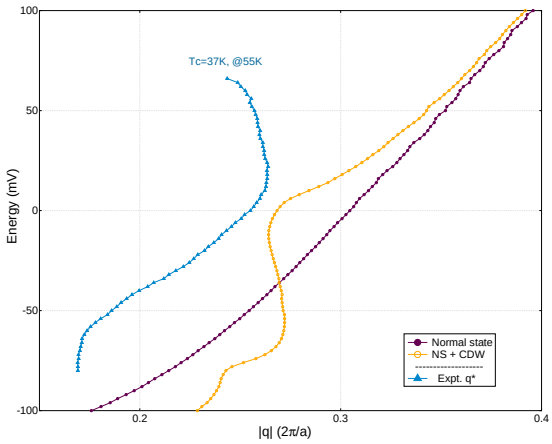


FIGURE 6.11: **CDW prediction compared with data.** The violet markers are for the normal state (Fig. 6.10A) , while the orange points are the renormalized dispersion due to the CDW (Fig. 6.10D). The blue data points from experiment exhibit markedly different dispersion.

Quantitative comparison of the two theoretical calculations with the actual data are given in Fig. 6.11. The distortion of the parabolic dispersion into flat vertical portion near $|q| \sim 2\pi/4$ is more evident. In addition, the shape of the resulting dispersion is very different from that of the experimental data: the former has slowly dispersive parts connected by a non-dispersive section ($S$-shape), while the latter has two non-dispersive section connected by a dispersive section (inverted $S$-shape). The two dispersions may seem to coincide by energy shift of 80mV, but this will require huge error in estimating the doping level. Manifestly, CDW is *not* the origin of the experimental $q^*(E)$ in the pseudogap phase of strongly underdoped cuprate, contrary to the conclusion of Wise *et al.*[178] and Ma *et al.*[179]

## 6.9 Open questions

The $p$-$h$ asymmetric dispersion of CBM wavevector $q^*$, dominant in compounds with low $T_c$ and consistent with many other experimental data, invalidates the CDW origin of the anti-nodal charge ordering. However, the $q^*$ raises other questions.

The imminent one is the nature of the $q^*$. If not associated with CDW, what physics does it represent? What is the origin of the apparently dispersive anti-nodal charge ordering? How does $q^*$ relate to the normal state band structure above $T^*$? Why does it occur?

The next inevitable issue in strongly underdoped regime is the strong setup-point effect. [166] If the asymmetrically dispersing $q^*$ is strong only in samples with strong setup effect, the $q^*$ might be simply the wavevector representing the effect. One direct way to check this possibility is to compare $q^*$ with anti-nodal ARPES MDC cut of strongly underdoped Bi2212. If MDC cut shows dispersing peak as in NCCOC[177] of wavevector matching $q^*$, then the setup effect must not be a major contribution. However, even in case $q^*$ is somehow confirmed to be merely representing the setup effect, it is a very useful piece of information as there has been no quantitative estimate of the spatial variation of the effect.

The absence of anti-nodal charge ordering proposed by Chatterjee *et al.*[164] is another opponent. Their conclusion is based on the absence of shadow band shifted from the original arc by the nesting vector. It could simply be because they measured $T_c$=76K Bi2212. The CBM could be too weak up to 20mV binding energy in this doping.

It should be noted that the energy range of all STM data in this chapter is limited to under 100mV. The relation of the anti-nodal asymmetric $q^*$ dispersion at low-energy to the high-energy pseudogap[87,187] is yet to be studied. Is the anti-nodal PG static at high energy but dispersive at low energy? Whether the two pseudogap physics can be consolidated into a unified picture and how it looks will be a key in constructing the right theory of pseudogap.

Another point worth noting is that the result of McElroy *et al.*[152] revealed a spatial mixture (or separation) of two regions with distinct spectra. In terms of coexisting SC and CBM, the data can also be interpreted as patchy CBM superposed onto the omnipresent strong SC, contrary to the pre-cursor picture in which SC develops out of PG. How does $q^*$ beyond $\Delta_0$ at higher doping relate to $q^*$ at lower doping? How does the anti-nodal CBM emerge in real space with decreasing doping from the optimal value?

Answering to these open questions will help further understand the CBM, anti-nodal physics, and eventually the pseudogap itself.

# Appendix A

# Anatomy of Cornell STM3

The SI-STM currently housed in building 480 of BNL (Brookhaven National Laboratory; Upton, NY) was the third STM located in the basement of the Clark Hall at Cornell University. After 5 months of preparation it was transported to BNL early March 2010, and it took about another year until the resumption of normal operation. A significant deal of components had to be either modified or added owing not only to the new environment, but also to the equipment availability.

Appendix A provides detailed information on the STM prior to the moving, most of which are inherited with no major modifications. Appendix B covers the new environment as well as the upgrades that had to be made after the moving, or that were decided to be made albeit not critical. Many diagrams in the appendices were drawn particulary for the parts that lacks relevant records, in order for anyone without prior knowledge on this STM to understand the detail quickly.

## A.1 Electronics connection diagram

STM3 was installed in two adjacent rooms of Clark Hall basement for years: probe and cryostat in BA09 (acoustic room), and control equipment in BA11 (control room). The electronic components in figure A.1 were mounted in two electric enclosures (racks) in the

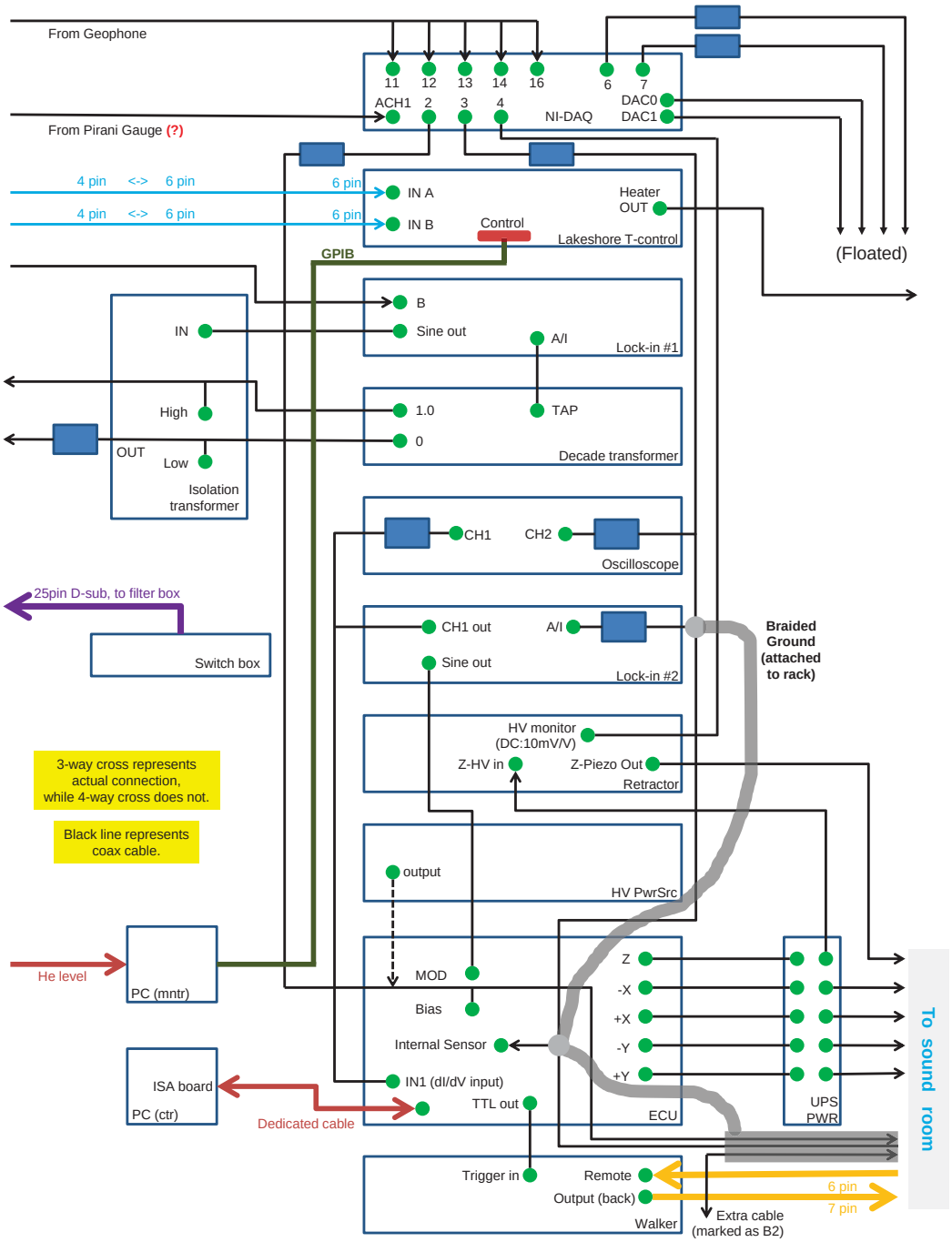


FIGURE A.1: **Electronics connection diagram** for components mounted on two racks in BA11 Clark Hall (control room), except for the two PCs. All lines and arrows into or out of the page represent connection from or to the acoustic room.

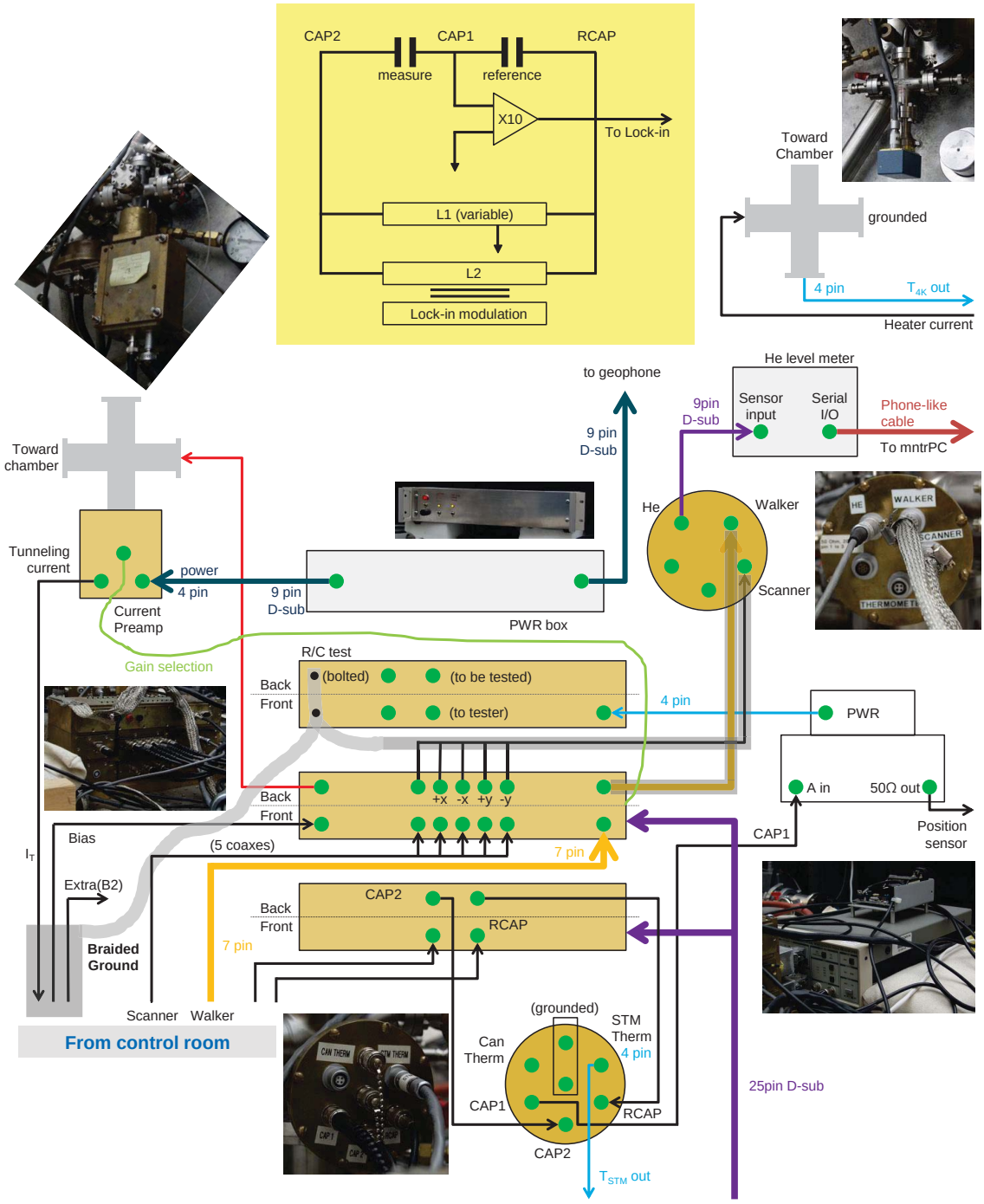


FIGURE A.2: **Electronics connection diagram** for components installed on the optical table in BA09 Clark Hall (acoustic room). All lines and arrows into or out of the page represent connection from or to the control room.

control room, and those in figure A.2 were installed on the optical table in the acoustic room. The electronics configuration implements key components of STM / STS described in Chapter 4, including ECU-based feedback scheme, spectroscopy with lock-in technique, semi-automatic walker, position measurement with LC-bridge and communication with control PC. A few things that are not covered in Chapter 4 are:

1. Temperature feedback. Stable temperatures above the base temperature is maintained with an independent feedback circuit run by a Lakeshore 340 controller. mA range of current (value range to be verified) flows through the heater unit at the STM base plate, and the temperature of the base plate is measured with Cernox CX-1070 RTD (Resistance Temperature Detector) by Lakeshore (see figure A.4 (d) and (e)). The tip needs to be walked back sufficiently before raising the temperature, as the thermal expansion of the head parts tends to reduce the tip-sample distance.

2. Liquid Helium level monitor. The liquid helium level inside the experimental dewar is measured with Lakeshore 241 monitor and 25"-long Nb-Ti superconducting sensor wire whose resistance varies linearly with the height of the superconducting portion. The sensor bottom sits on the 4K flange, so that the level reading is about 12.5" when the liquid helium tops off the dewar belly of 14" height.

3. Filter / relay switch box. Dr. Jhinhwan Lee designed a three-story brass tower (in the middle of figure A.2) dedicated for (1) the $\pi$-bridge LC filter to block RF noise (2) the relay switches for convenient selection of a number of parameters remotely in the control room, including current preamp gain / bias voltage divider bypass / cutoff frequency for piezo voltages.

4. HV bipolar power source. See Appendix B.

## A.2 Wiring around and inside the vacuum chamber

All signals in Fig. A.2 enter into or leave the main probe through either the two mushrooms (Brass cups) or the two 4-way cross ConFlat feedthroughs. Figure A.3 shows the connection

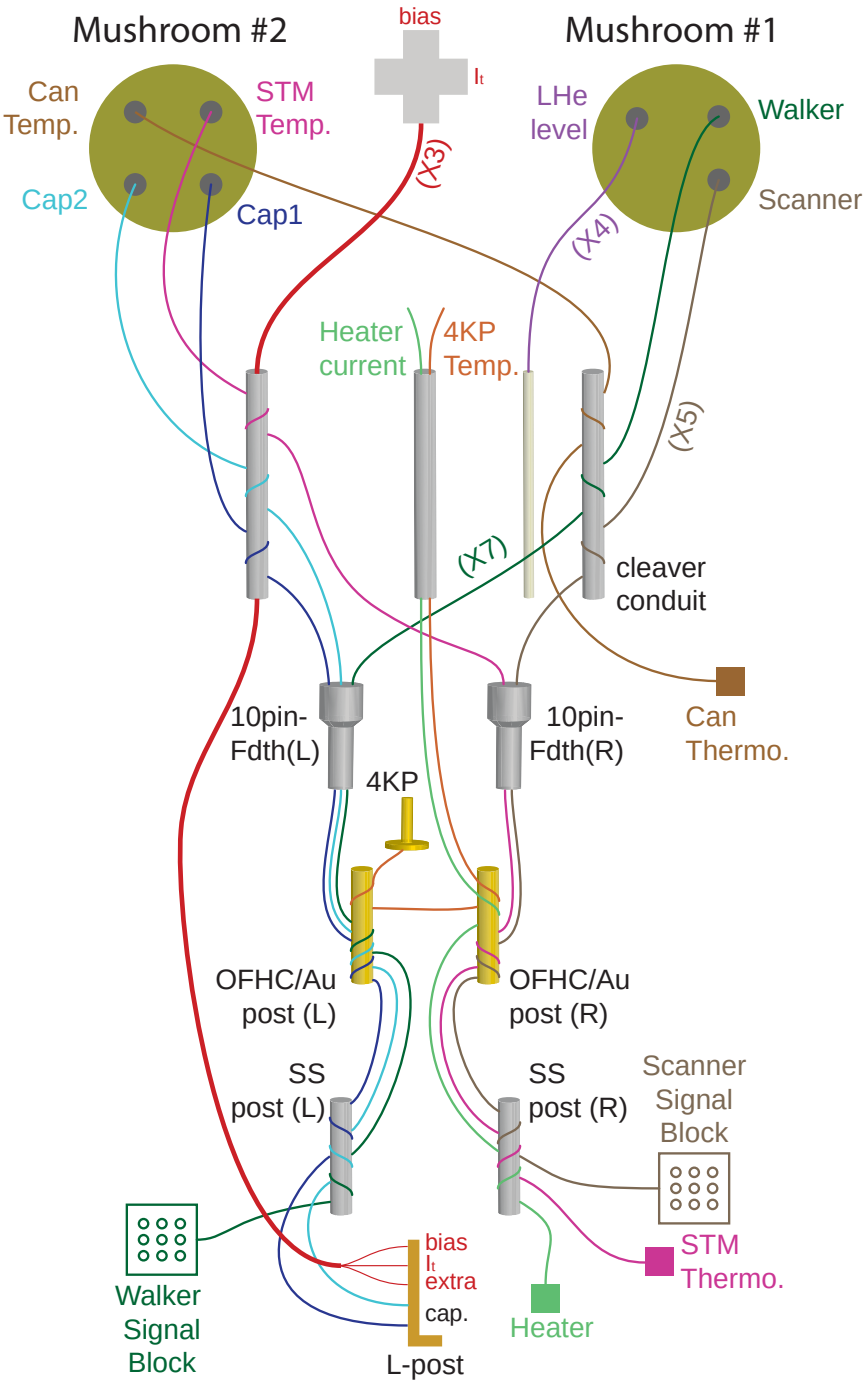


FIGURE A.3: **Wiring diagram of the main probe.** Left / Right is when seen from the back. All components are in UHV except for (1) the LHe level sensing line (2) can thermometer line (3) reference capacitor line, up to the 10-pin feedthrough (4) between the mushroom & the 10-pin feedthrough.

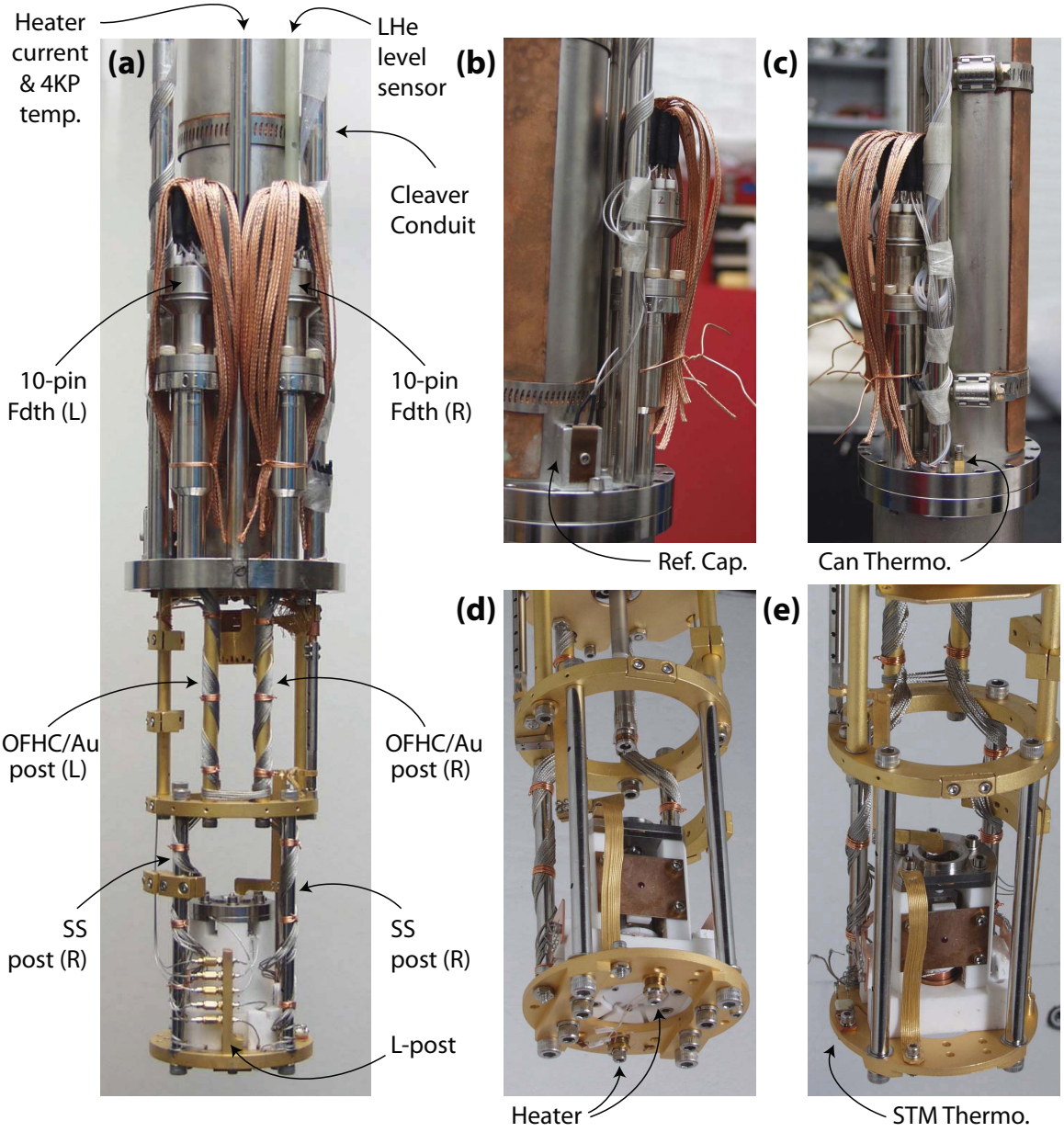


FIGURE A.4: **Actual wiring of the main probe.** (a) The back-side view of the actual wiring represented by Fig. A.3. (b)-(e) a few other components that are invisible in (a).

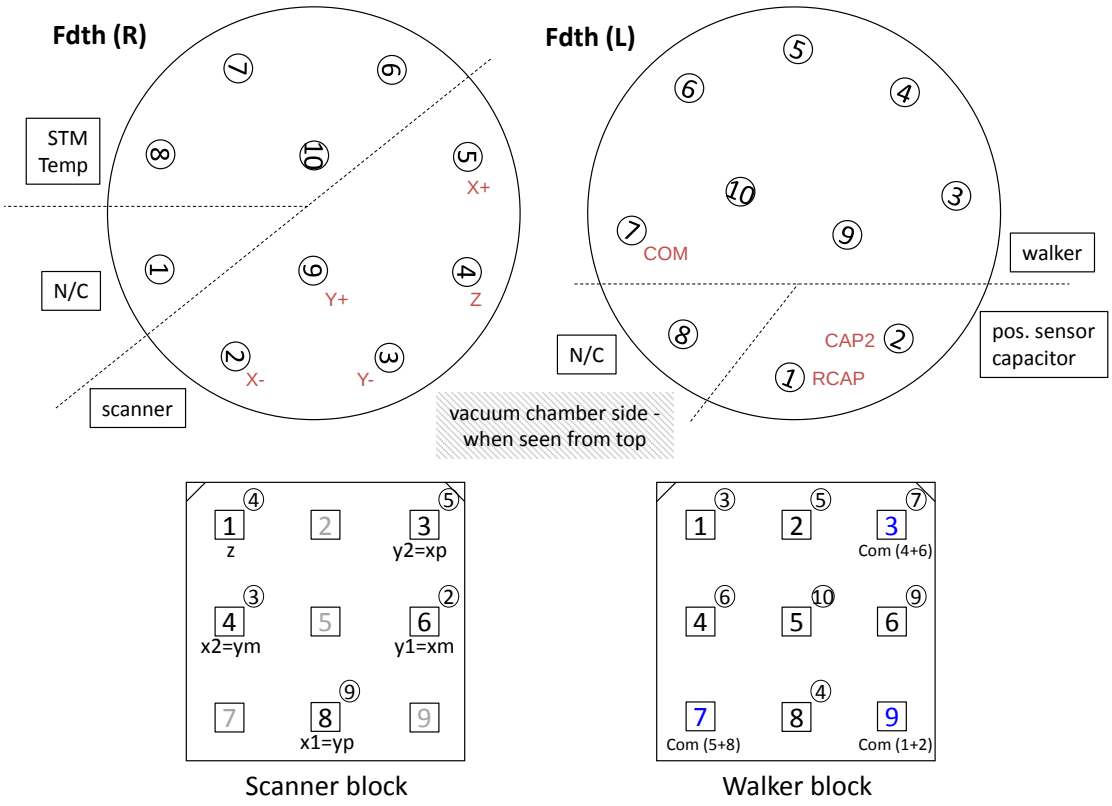


FIGURE A.5: **10-pin feedthrough and 9-pin signal block.** Connection configurations for the 10-pin feedthroughs and the scanner / walker block. Note that the feedthroughs are top-view, in an orientation in which the main chamber pipe is lying below so that the feedthrough on the left side is in fact "10-pin Fdth (R)" in Fig. A.3.

beyond them in schematic,[1] and figure A.4 shows the actual images. The signal wires are helically wound tight on tubing and posts wherever possible in order to minimize introducing mechanical vibration as well as to maximize heat dissipation. The cables are mostly flexible coaxial type, importantly except for the three semi-rigid coax wires for bias / tunneling current / extra line that connect to the L-post at the bottom.

[1]Fig. A.3 represents the current connections in BNL; only two capacitance signals have connection unlike the old configuration as in Fig. A.2 in which three capacitance connections are required. See appendix B for detail.

Pin arrangements of the two ten-pin feedthroughs, which delivers most signals into the vacuum chamber, are shown in Fig. A.5. 7 walker voltages and 5 piezo voltages are carried finally into the STM head through two 9-pin blocks on each side of the head. Configuration of them are also provided in Fig. A.5.

## A.3 Piezo retractor and repair

When compared with the other four piezo voltages, the $V_z$ passes through an additional box - retractor - as in Fig. A.1. The (piezo) retractor is a voltage supply which can selectively override the $V_z$ generated by ECU only toward the more negative values; the output is the lower between $V_{z,\mathrm{ECU}}$ and the internal voltage set by a knob. The name retractor derives from the fact that it can provide negative voltages only, so that it can only *retract* the piezo axially from the unstrained length.

The retractor is of significant help in cases $V_z$ lower than -220V beyond the range of the ECU is preferred, such as liquid helium refill. The tip can also be pulled away from the surface with walker, but the walking is a coarse irreversible process in which the tip location and the $V_z$ are not reproduced after the walking back and forth, neither the tip-sample distance can be fine-tuned during the field-emission tip treatment. In addition, the retractor protects the tip from crashing the surface on the first few steps of walk-back, a great benefit particularly after the *in-situ* field-emission.

Retractor needs to be used with caution due to its overriding capability. For example, the tip may stop approaching when the tunneling current saturates by crashing if the retractor is suppressing the $V_z$ variation (see 3.3). Retractor should be released to bypass mode immediately after finished with overriding.

In May 2011, the piezo retractor for BNL-STM was found to be malfunctioning. Following voltages at each node diagnosed that the input voltage to the comparator stage as well as to the seven-segment display were not in accordance with the design specification, due to burnt resistors in the voltage divider. Repair was simple: replacing two resistors fixed the problem. Figures A.6 and A.7 contain the circuit detail that was learned during the repair.

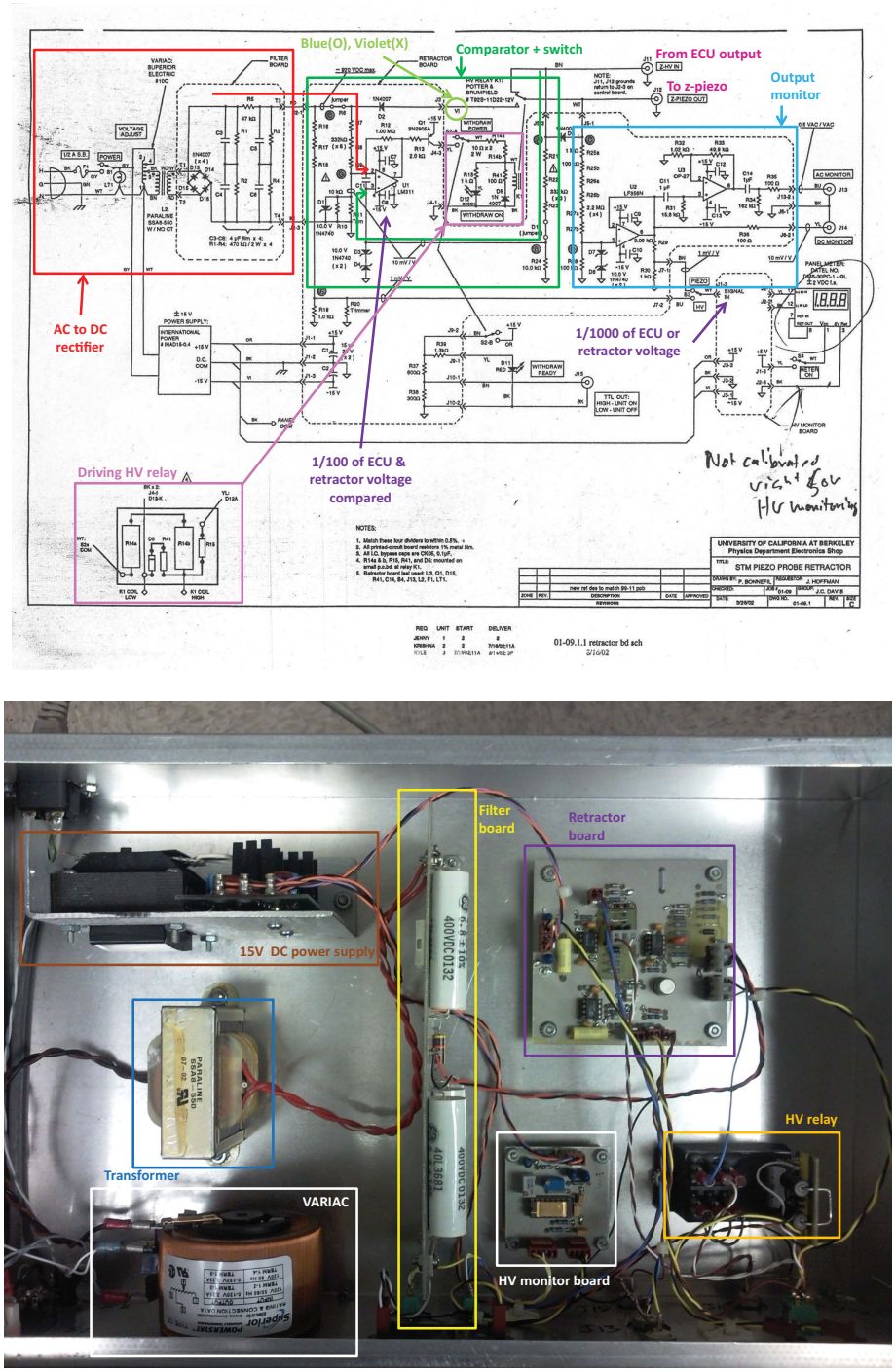


FIGURE A.6: **Piezo retractor.** (top) Circuit diagram of the retractor with the role of each block. (bottom) top-view image of the actual retractor.

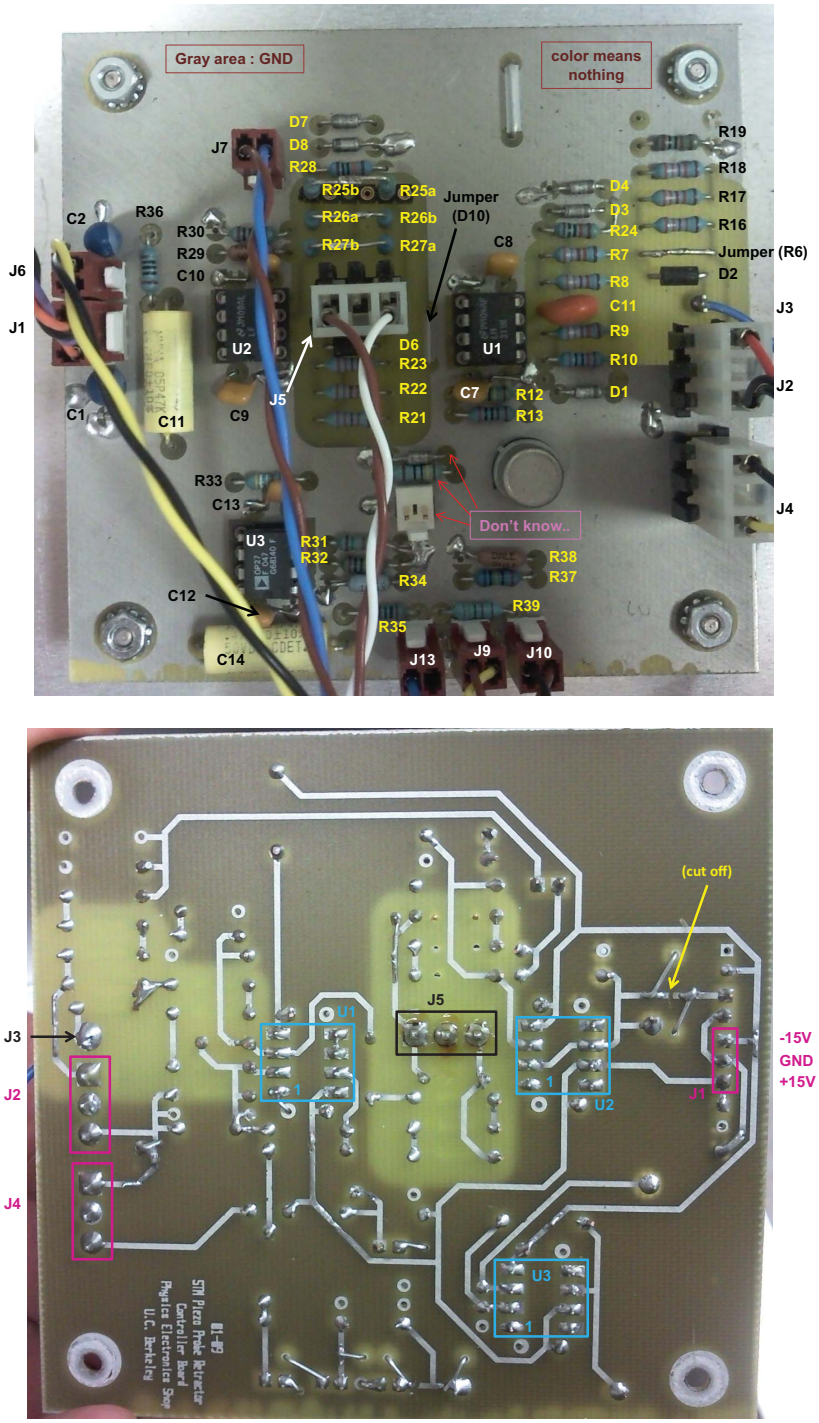


FIGURE A.7: **Retractor board.** Enlarged images of (top) the front and (bottom) the back side of the retractor board. Circuit elements are labeled in accordance with the diagram in Fig. A.6.

## A.4 Piezo-UPS

In rare but finite cases the operating system of the control PC freezes. The PC and the ECU can be restarted, but the piezo $z$-voltage turns zero immediately. The tip crashes hard to the surface if the feedback was engaged at negative $V_z$. Feedback with positive $V_z$ stands on a safer side, but it still accompanies soft crash with the strength proportional to the instantaneous voltage change. The best remedy to survive the tip is pulling it back slowly particularly at the beginning.

Dr. Jhinhwan Lee designed the "Piezo-UPS" (labeled as "UPS PWR" in A.1) which can provide arbitrary piezo voltages at any moment. Once the system freezes, the Piezo-UPS is set to supply piezo voltages matching those from the ECU to prevent sudden voltage jump, and then the $V_z$ is slowly retracted to the lowest value (-220V). The Piezo-UPS can match all five piezo voltages, but holding / retracting $V_z$ only is sufficient for most cases.

See figure A.8 for circuit schematic, as well as the notes and the operational procedure below for the actual application.

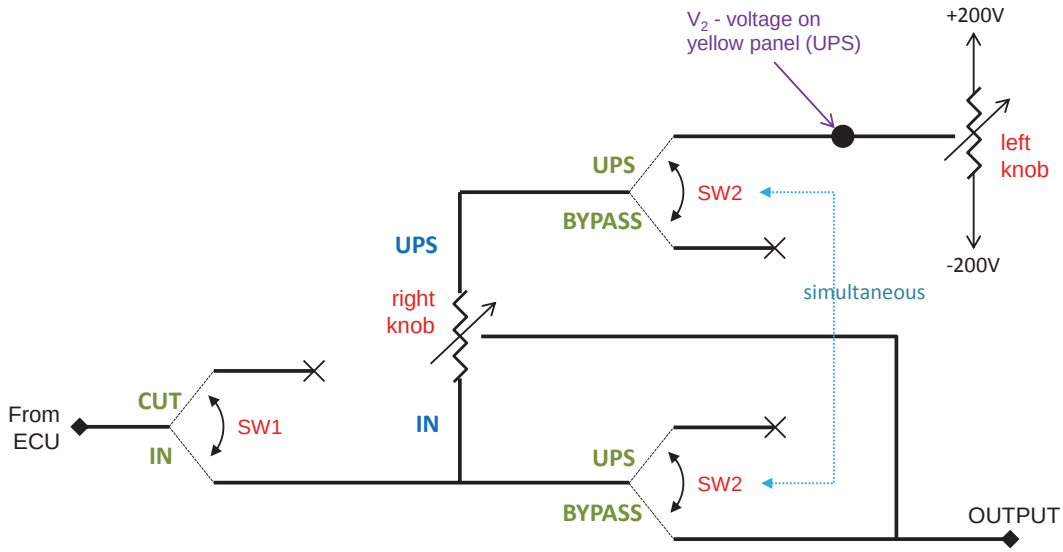


FIGURE A.8: **Piezo-UPS circuit diagram.** $V_{ECU}$ can be matched by the internal power supply on the top right corner. ECU and PC can be restarted after SW2 switches the voltage source from ECU to the internal supply. The Piezo-UPS has five sets of this circuit for each piezo signal.

[Notes]

1. Voltages float and the panel doesnt show correct values if the main power switch is off or when power is out. So *keep the switch ON* all the time. Bypass still works even with no power.

2. Normal stand-by position : Left knob in the middle so that $V_2$=0, right knob fully turned CW for IN position. SW1 - (IN), SW2 - (Bypass).

3. With SW1 (CUT) and SW2 (UPS), the lower input to the left variable resistor (to vary with right knob) floats and the output changes from $V_2$ to ∼80% of $V_2$ in magnitude. It is recommended to avoid this setup, though acceptable for both positive and negative ECU voltage. For negative $V_{ECU}$ we can use retractor, and for positive $V_{ECU}$ the output voltage decreases when the right knob is turned from IN to UPS. In short, no need to turn SW1 to CUT at any point.

[Operation]

1. Make sure that the right knob points IN.

2. Adjust the left knob so that $V_2$ matches $V_{ECU}$ input, so that all three voltage are the same.

3. Turn SW2 from BYPASS to UPS.

4. Turn the right knob from IN to UPS. For some reason this changes the input voltage reading to +200V. Output doesnt change.

5. Turn the left knob CCW toward the wanted voltage; preferably all the way to -220V, but at least below zero.

6. Hold $V_z$ with the retractor. Now we are safe.

7. Turn knobs back to the normal stand-by setup as described in the [Notes] above.

8. Restart PC & ECU.

9. The retractor can be turned off only after TopoSPM produces -220V.

## A.5 I-V offset adjustment

Ideally, current-voltage relations measured on a metallic sample of flat DOS near $E_F$ should be linear with slope inversely proportional to the tunneling junction resistance. More importantly, the lines should all pass through the origin, i.e., zero current at zero bias voltage. Which is not the case in practice as shown in Fig. A.9 for example.

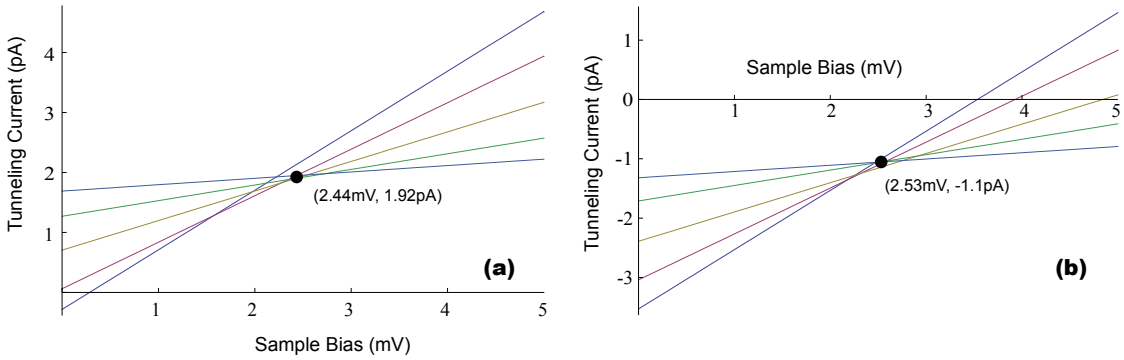


FIGURE A.9: **Measured I-V offset.** Lines represent the linear fits of the measured (I, V) variation at different junction resistances for (a) forward and (b) reverse voltage sweep. Measurement voltage range was 100mV; only the region near the offset origin is shown. The actual junction resistances were 1/1.25/2/4/10GΩ from the highest to the lowest slope.

Independent of the asymmetry from the voltage sweep direction, bias voltage and the average of the currents for two sweep directions at crossing points are slightly off from zero. One big source of the non-ideal behavior is the Op-amp itself. The deviation of the Op-amp off the ideal characteristics such as small but finite input offset voltage and input bias currents significantly shifts the ideal origin.

The offset can be corrected in two ways. First, Op-Amps typically have offset voltage trim, in which an external variable resistor changes the output reading by tens of mV, or tens of pA at $10^9$ gain. A few mV offset still remaining after rough adjustment with the variable resistor can be manually compensated with sub-mV precision by typing the required value into the TopoSPM software. The current offset can also be adjusted with `Setup` → `Trim Bias/Current` → `Trim Current ADC` in TopoSPM menu.

# Appendix B

# Anatomy of BNL SI-STM

## B.1 Acoustic room

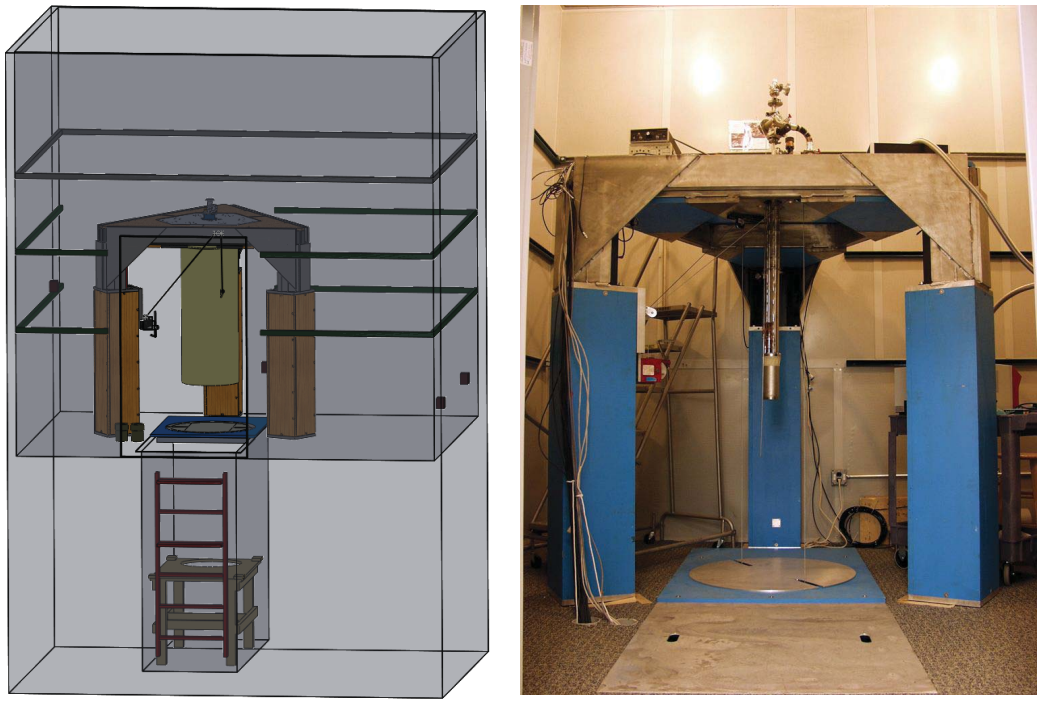

FIGURE B.1: **BNL acoustic room.** (left) Drawing and (right) image of the acoustic room in building 480.

Back in Cornell, STM3 was unique in that it didn't have metallic acoustic enclosure nor was mounted on a hexagonal plate fixed on top of the three-leg cryostat as other two STMs. It was installed on a *rectangular* optical table, with the Sonex foam providing the only acoustic isolation. The BNL-STM is now configured in a more standard style except for the air spring lifting the concrete block.

Installed on top of the 100-ton concrete block, the inner section of the acoustic enclosure manufactured by IAC (Industrial Acoustics Company) has inside dimension of 13'3"(W) × 11'(D) × 12'10"(H). The three-leg cryostat is installed at the inside end of the 3'(W) × 8'(D) × 7'(H) pit slightly off the room center (Fig. B.1). The pit is primarily to store the dewar when not in need, for example during tip replacement. A wooden platform of half the pit height is at the bottom along with a SS access ladder. Three rings of Uni-struts (in dark green color in the figure) are mounted on the wall for wall fixtures. Small brown boxes on the vertical wall in the drawing indicate the location of some of the AC power outlet. The two PVC conduits for signal cable connection with the control room are right in front of the left leg.

## B.2 AC mains power & grounding

AC power for BNL-STM1 is fed through a UPS (Uninterruptible Power Supply) unit by APC and a three-phase isolation transformer in Rm 1-147, and delivered to the electric panel in the control room. One big concern in electricity supply system is separating the ground for the sensitive equipments from the rest, to secure a stable voltage reference free from any external source of ground fluctuation.

BNL STM1 power lines are divided into two types: clean / dirty power depending on the nature of the power ground. Equipments critical to the measurement sensitivity are plugged into the clean power outlet where the ground comes from the concrete block, or essentially from the earth. All other non-critical utilities such as pumps and leak detector draw currents from dirty power which shares ground with the rest of the building (Fig. B.2).

Apart from the power ground, the safety ground for metallic conduits and the acoustic enclosure are also provided through the building ground. Therefore the 'regular outlet' for

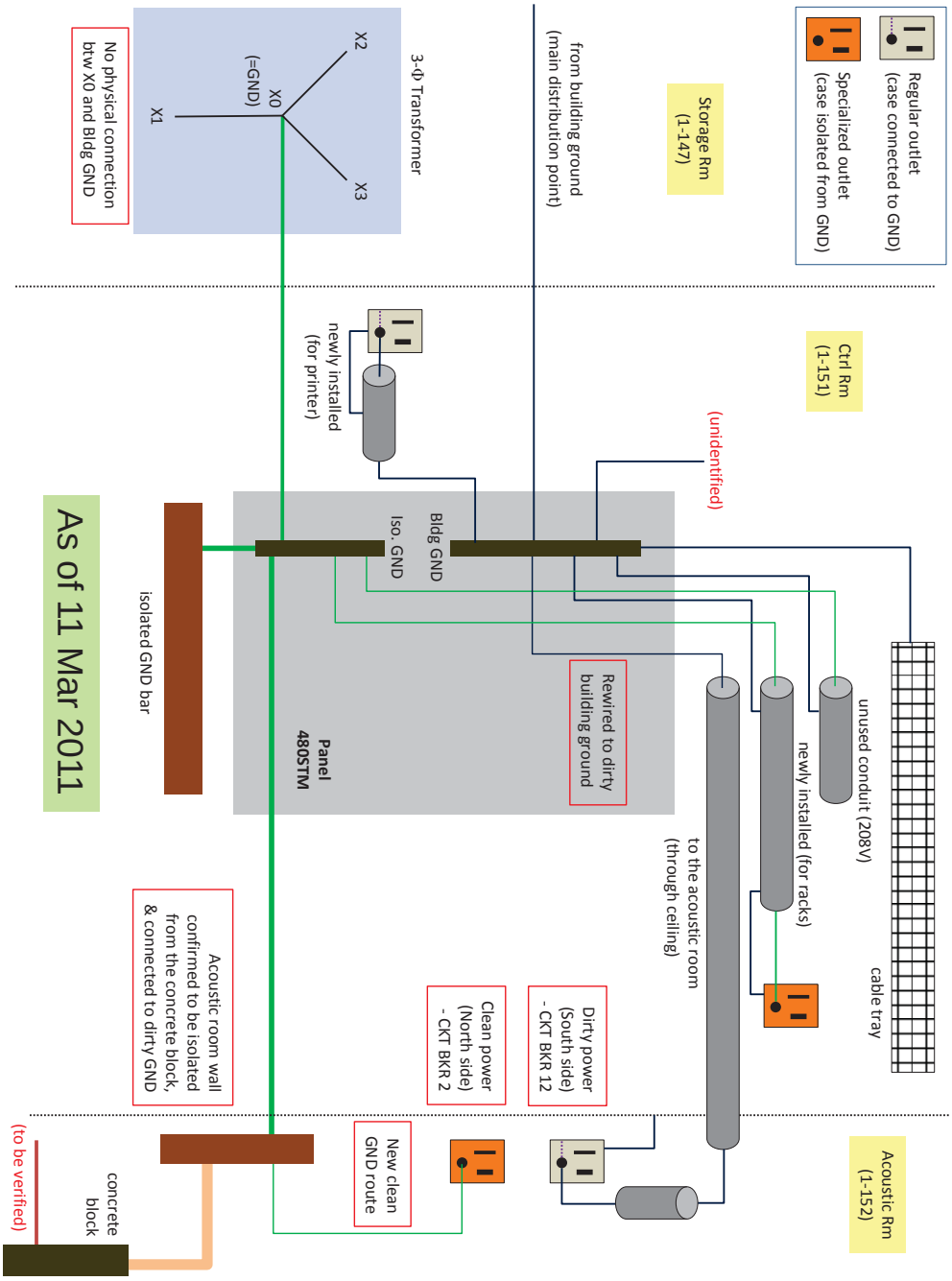


FIGURE B.2: **Grounding scheme.** Grounding diagram for BNL STM1. Green lines represent isolated clean ground for equipments, and dark blue lines represent dirty building ground for safety purpose.

dirty power has inner connection between the casing and the power ground (denoted by dotted line inside the regular outlets in Fig. B.2), while the 'specialized outlet' for clean power in orange does not.

## B.3 Electronics

The electronics connection for BNL STM1 is almost identical to the old STM3 as given in Appendix A. One major modification is the replacement of the LC bridge with a stand-alone capacitance bridge for position sensing as described in chapter 4. As a result, Lock-in #1 / decade transformer / reference capacitor (not shown in Fig. A.1) / amplifier for the CAP1 signal are dropped and a capacitance bridge box is added. The high-voltage power source is also replaced with a commercial power supply plus polarity switch as described in a later section.

## B.4 ECU internal connection

The extra ECU to be used in BNL had everything including PCB circuits, AC power, dedicated cable for communication with PC, ISA board and output panel for coaxial cables. But the missing internal connections between the PCB circuit and the coaxial cable panel had to be hard-wired based on the available resources such as a diagram of unidentified source (apparently by the ECU manufacturer, but no confirmation) and the ECU under normal operation. The current configuration that was tested good and is working fine so far is as below (see also Fig. B.3).

| Block | GND pin | Signal pin | Signal |
|---|---|---|---|
| CN4 | A04 | A03 | Sample bias |
| CN4 | B03 | C03 | Modulation in |
| CN4 | B17 | C17 | Tunneling current |
| CN3 | C05 | C06 | Pizeo Z |
| CN3 | C09 | C08 | Piezo -Y |
| CN3 | C09 | C10 | Piezo +Y |
| CN3 | C13 | C12 | Piezo -X |
| CN3 | C13 | C14 | Piezo +X |
| CN10 | B23 | C23 | Walker trigger |

| Block | pin1 | pin2 | |
|---|---|---|---|
| CN4 | B23 | C23 | Misc. connection |
| CN4 | B24 | C24 | Misc. connection |

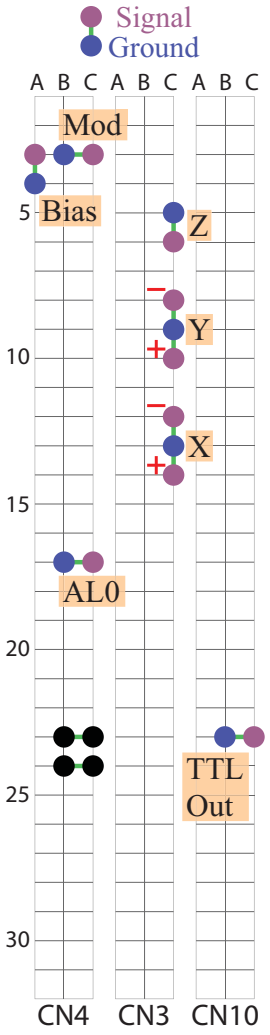


FIGURE B.3: Breakout panel.

ECU has three parallel PCB boards fixed on the front panel. The biggest one is the main board, and two small side boards are mostly for signal interface. The outer one of the two boards has three 3×32 pin blocks labeled as CN3 / CN4 / CN10. The IN1 / IN2 coax ports to accept output from the lock-in amplifier were already hard-wired to the inner board so didn't have to touch.

## B.5 Bipolar high-voltage power source

Unlike walker and piezo retractor, no extra bipolar high voltage power supply was available. One easy and affordable option was using a commercial power supply of *single* polarity (TDK Lambda, Genesys 600-1.3U: 600V / 1.3A 780W model) appended with an external polarity switch. The DC output can be safely inverted with a simple three-way switch, as 10 $\mu$A current flows at most during the field emission and even the simplest switches have a few hundred volts rating. See Fig. B.4 (a) for the wiring inside the switch.

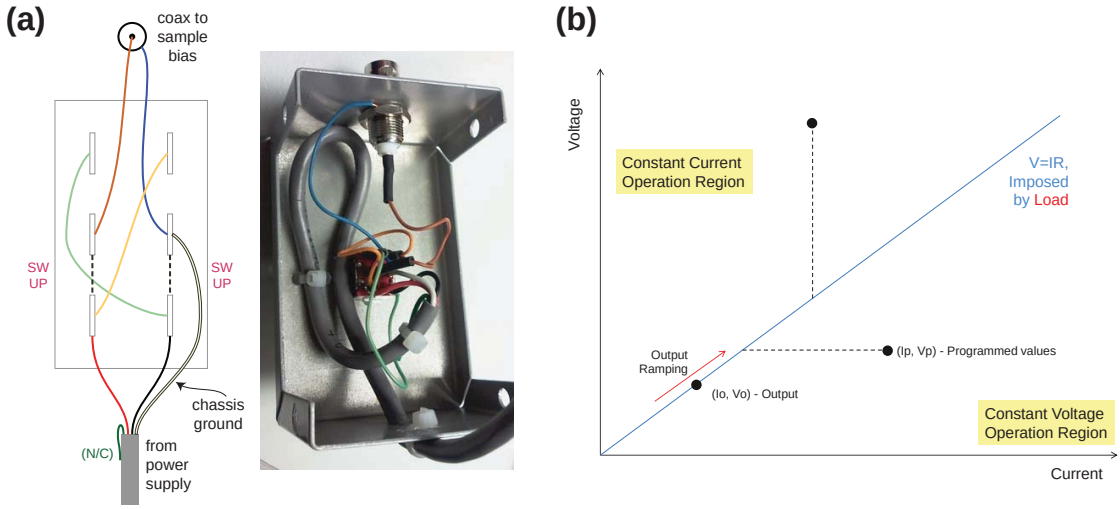


FIGURE B.4: **New high-voltage bipolar power supply.** (a) (left) Schematic of the polarity selection switch. (b) The actual switch. The colors of the wire match. The three-way switch (in the back of the case) can be in up / neutral / middle position. The electrodes in the middle row are connected to those in the bottom (top) row for up (down) position, and to neither in the neutral position respectively. (b) Behavior of a generic power supply. The output values move along a straight line determined by external load, until diverting to the dashed lines representing the configuration specified by voltage / current knobs.

A general-purpose power supply can typically operate either in constant voltage or current mode, depending on the user-defined voltage and current limit values as well as the load line. The output of the power supply can be summarized in a simple diagram such as Fig. B.4 (b), or as following.

1. Output voltage and current always vary in accordance with Ohm's law, $V_p = I_p \times R$. Here R is the equivalent load resistance. Change in load modifies the slope of V=IR line which separates the two regions.

2. Mode is determined by the position of ($I_p$, $V_p$) relative to the V=IR line. ($I_p$, $V_p$) determines ($I_o$, $V_o$).

3. Constant voltage operation means that voltage is the independent variable, with current given by I(V)=V/R. Similarly, current is the independent variable in constant current operation mode and V(I)=IR.

4. When the OUT button is pressed on, the output voltage and current slowly ramp up from zero along the V=IR line until either $I_o$=$I_p$ or $V_o$=$V_p$. For ($I_p$, $V_p$) given above, ramping stops on $V_o$=$V_p$ ($I_o$=$V_o/R < I_p$).

5. Knob moves programmed value. ($I_o$, $V_o$) simply readjusts to the new ($I_p$, $V_p$) according to 4.

6. In PREV (preview) mode - the display shows programmed values. Neither has anything to do with the actual output.

7. In OUT mode - the display shows output values determined by 4. Either $I_o$ or $V_o$ coincides with the programmed value.

8. One can change ($I_p$, $V_p$) in either PREV or OUT mode. In PREV mode, turning either knob will change the displayed value. In OUT mode, in contrast, only the independent variable knob will; turning dependent variable knob will change programmed value only, which will not be reflected on the output unless ($I_p$, $V_p$) points crosses the V=IR line.

9. Minimum values (specific to the current power supply): 4mA / 0.3V

## B.6 Sample transfer rod & differential feedthrough

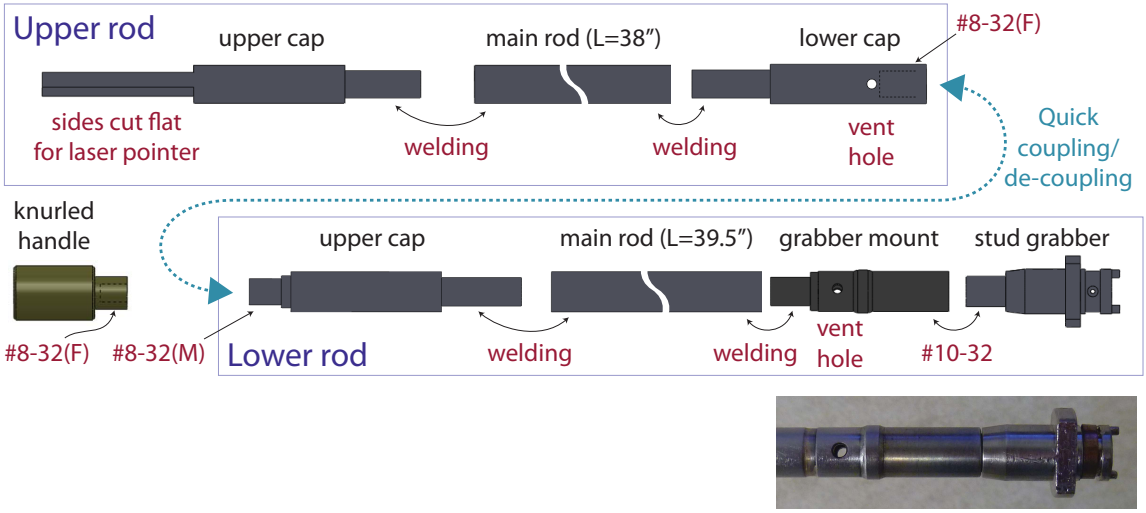


FIGURE B.5: **New sample transfer rod.** Parts in two boxes are assembled in one pieces (upper / lower rod). During sample transfer, the two rods are coupled and decoupled easily with threaded joint. At the bottom is the actual image of the bottom portion of the lower rod. The knurled handle is fastened to the lower rod when only the lower rod is inserted, for convenient handling and slip-loss prevention.

In Cornell, STM3 used a ∼100”-long single-body sample transfer rod. Due to the limited height clearance (∼50”) of the ceiling, sample transfer rod for BNL had to be redesigned into a unit of two pieces much like STM1. Separating the transfer rod into two pieces requires a few things, including (1) easy assembly and disassembly with threads (2) differential feedthrough for pre-evacuation of the threaded portion after the assembly but before being inserted into the UHV chamber (3) dedicated utility pump and pressure gauge which runs independent of the turbo pump for main vacuum chamber.

Similar to the STM1 transfer system, the new transfer rod has two parts (upper / lower rod) of comparable length that couples with #10-32 thread. The upper / lower rod are essentially long SS cylinder to minimize thermal inertia for fast cooling during the sample transfer. Solid pieces brazed at the ends hermetically seals the two cylinder, and sample stud grabber plus grabber mount are at the bottom of the rod assembly as shown in Fig. B.5.

The differential feedthrough shown in Fig. B.6 is sealed with o-rings on each side. The symmetric NW16 flanges are for vacuum pump and gauge connection. The small volume of threaded portion takes a few minutes to be evacuated to $\sim 4 \times 10^{-3}$ mTorr with the Varian DS202 rotary vane pump (model verification required). Then the transfer rod can be lowered further into the chamber without significantly disturbing the high-vacuum.

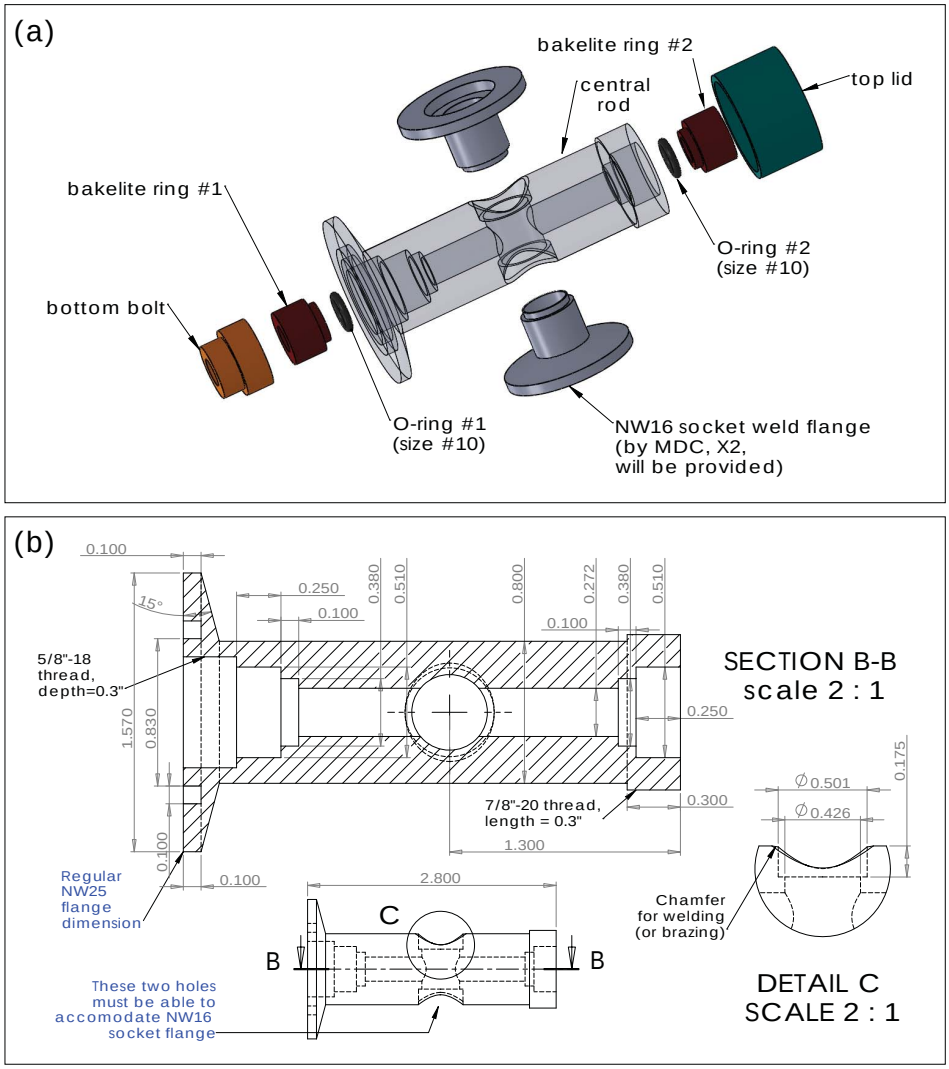


FIGURE B.6: **Differential feedthrough.** (a) Structure and components of the differential feedthrough. Dimension of the main body is in (b).

## B.7 Liquid cryogen transfer siphon extension

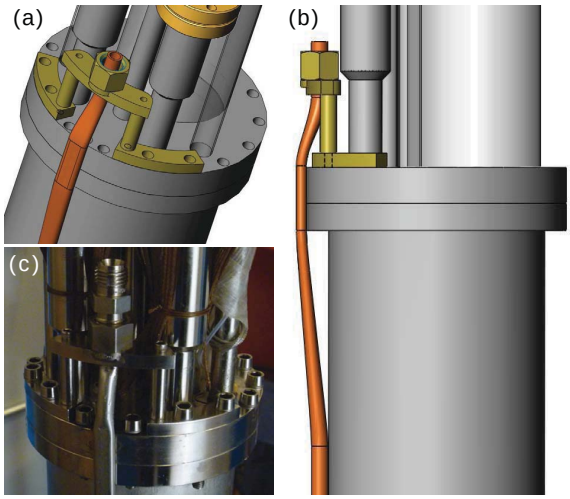


FIGURE B.7: **Liquid cryogen transfer siphon extension.** (a) Siphon extension pipe(brown) with frame(olive) attached on the 4K flange. (b) Side view of the extension. The pipe is bent and pressed such that it can detour the flange with minimal protrusion. (c) Image of the frame and pipe mounted on the flange.

In Cornell, the liquid nitrogen and helium were transferred and recovered with an L-shaped transfer pipe. It was not long enough to reach the bottom of the dewar; the L-pipe could access liquids down to the 4K flange height only. A longer but thinner tubing had to be inserted to remove the rest of the liquid, which took many hours particularly for nitrogen. A thicker tubing that runs all the way down to the bottom of the dewar should save significant amount of time (see Fig. 3.13). Another advantage of extension tubing is that the cryogen transfer will introduce less thermal shock, because the cryogen will fill up gradually from the dewar bottom instead of directly bombarding the 4K flange.

One problem in extending the transfer line was the existence of the 4K flange. Due to the requirement that the mating point with L-pipe lies *within* the flange, the extension tubing had to be bent around the flange area as apparent in Fig. B.7 (b). Another problem was that the tight space margin between the dewar neck ID and the 4K flange OD severely limited the radial protrusion beyond the flange. So the extension pipe had to be pressed flat and bent to barely avoid the flange.

Although not shown in Fig. B.7 (c), a 1/4" straight Swagelok union adapter fastened on the nut holds tight the extension pipe. The top cone of the adapter mates nicely with the bottom of the L-pipe.

## B.8 Gas handling unit

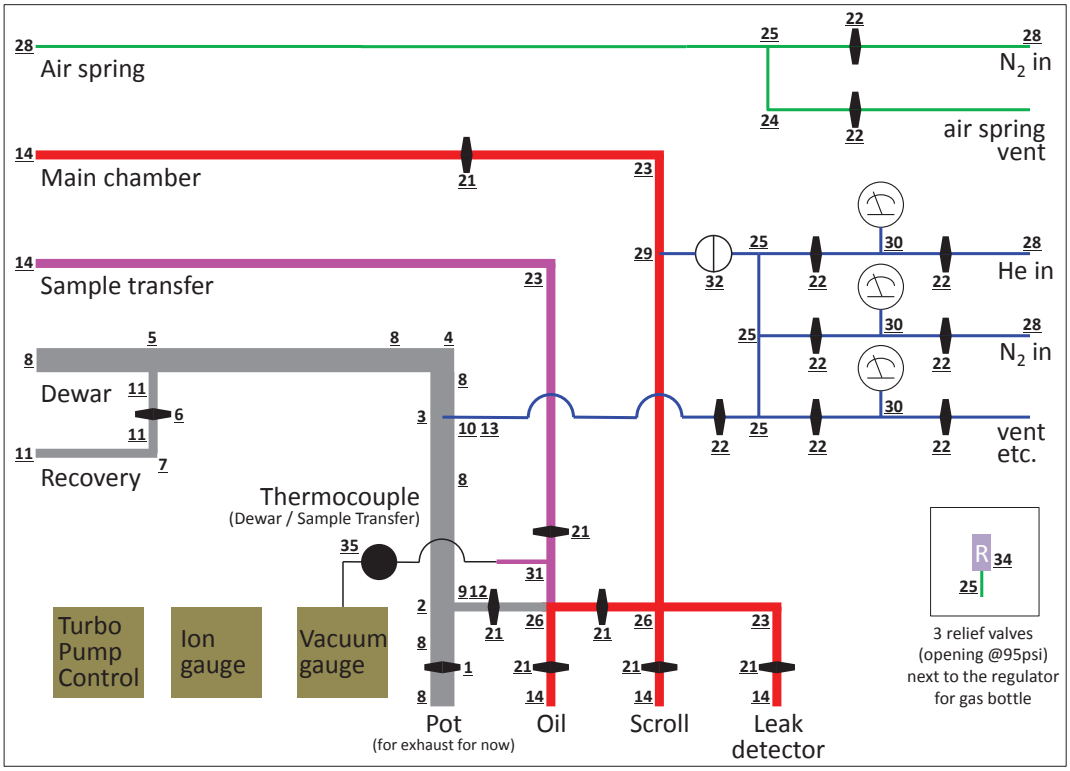


| # | Description | # | Description | # | Description | # | Description |
|---|---|---|---|---|---|---|---|
| 1 | NW50 ball valve | 9 | NW40 centering O-ring (Viton) | 21 | 3/4" ball valve | 29 | 3/8" to 1/4" reducing union |
| 2 | NW50 to NW40 Tee | | NW40 clamp (Al cast) | 22 | 1/4" ball valve | 30 | 1/4" union, NPT female Tee |
| 3 | NW50 to NW25 Tee | 10 | NW25 centering O-ring (Viton) | 23 | 3/4" union elbow | | Gauge |
| 4 | NW50 90 degree elbow | | NW25 clamp (Al cast) | 24 | 1/4" union elbow | 31 | 3/4" to 3/8" reducing Tee |
| 5 | NW50 to NW16 Tee | 11 | NW16 centering O-ring (Viton) | 25 | 1/4" union Tee | | 3/8" to 1/8" NPT female connector |
| 6 | NW16 butterfly valve | | NW16 clamp (Al cast) | 26 | 3/4" union cross | 32 | 1/4" bellows-sealed valve |
| 7 | NW16 90 degree elbow | 12 | NW40 to 3/4" SWL adapter | 28 | 1/4" SWL to 1/4" NPT female | 33 | Gas flow meter |
| 8 | NW50 centering O-ring (Viton) | 13 | NW25 to 1/4" SWL adapter | | 1/4" NPT to push-to-connect adapter | 34 | Pressure relief valve |
| | NW50 clamp (Al cast) | 14 | NW25 to 3/4" SWL adapter | 29 | 3/4" to 3/8" reducing Tee | 35 | Thermocouple vacuum gauge |

FIGURE B.8: **Gas handling unit for BNL STM1.** Gas panel diagram and the list of parts with corresponding numbers. Left side connects to the STM, bottom side to the pumps and leak detector, and right side to the pump room (Fig. 3.8). Green/blue (red/violet) lines in the diagram are for 1/4" (3/4") diameter tubing. Grey channel is made of NW-terminated parts only. Note the centralized pumping scheme: any of the three pumps can evacuate any of the three spaces. (SWL ≡ SwageLok)

# Appendix C

# The setup effect

## C.1 The first attempt

STM tunneling current is well approximated by [132]

$$I(\mathbf{r}, eV) \simeq -\frac{4\pi e}{\hbar} \mathrm{e}^{-d\sqrt{\frac{8m\varphi}{\hbar^2}}} \rho_t(0) \int_0^{eV} \rho_s d\varepsilon = C \cdot \mathrm{e}^{-d(\mathbf{r})/\lambda} \int_0^{eV} \rho_s(\mathbf{r}, \varepsilon) d\varepsilon \tag{C.1.1}$$

in which the exponential dependence on the tip-sample separation is characterized by the decay length $\lambda$ of the perpendicular transmission term. At feedback condition specified by $V_s$ and $I_t$,

$$I_t = C \cdot \mathrm{e}^{-d(\mathbf{r})/\lambda} \int_0^{eV_s} \rho_s(\mathbf{r}, \varepsilon) d\varepsilon$$

so that

$$I(\mathbf{r}, eV) = \frac{I_t}{\int_0^{eV_s} \rho_s(\mathbf{r}, \varepsilon) d\varepsilon} \cdot \int_0^{eV} \rho_s(\mathbf{r}, \varepsilon) d\varepsilon = S(\mathbf{r}) \cdot \Omega(\mathbf{r}, eV). \tag{C.1.2}$$

Here the spatially varying function $S(\mathbf{r})$ with the unit of current represents the setup effect, *i.e.*, non-uniformity of the actual tip-sample separation, and the dimensionless $\Omega(\mathbf{r}, eV)$ denotes the integrated setup-free LDOS.

The derivative of (C.1.2) with respect to the bias voltage extracts LDOS, still corrupted by the setup effect:

$$g(\mathbf{r}, eV) = \frac{eI_t\rho_s(\mathbf{r}, eV)}{\int_0^{eV_s}\rho_s(\mathbf{r}, \varepsilon)d\varepsilon} = eS(\mathbf{r})\rho_s(\mathbf{r}, eV) \tag{C.1.3}$$

Dividing (C.1.3) by (C.1.2), or $g(\mathbf{r}, E)$ by $I(\mathbf{r}, E)$ cancels out the setup effect:

$$\frac{g(\mathbf{r}, eV)}{I(\mathbf{r}, eV)} \equiv \frac{\texttt{1FL}(\mathbf{r}, eV)}{\texttt{FFL}(\mathbf{r}, eV)} = \frac{e\rho_s(\mathbf{r}, eV)}{\int_0^{eV}\rho_s(\mathbf{r}, \varepsilon)d\varepsilon} = \frac{d\Omega/dV}{\Omega} = \frac{d}{dV}\ln\Omega(\mathbf{r}, eV) \tag{C.1.4}$$

Then

$$\Omega(\mathbf{r}, eV) = \exp\left[\int_0^{eV}\frac{1}{e}\frac{\texttt{1FL}(\mathbf{r}, \varepsilon)}{\texttt{FFL}(\mathbf{r}, \varepsilon)}d\varepsilon + k(\mathbf{r})\right] = \exp[k(\mathbf{r})]\cdot\exp\left[\int_0^{eV}\frac{1}{e}\frac{\texttt{1FL}(\mathbf{r}, \varepsilon)}{\texttt{FFL}(\mathbf{r}, \varepsilon)}d\varepsilon\right], \tag{C.1.5}$$

so that the setup-free LDOS $\rho_s(\mathbf{r}, \varepsilon)$ is obtained in principle from the ratio of `1FL` to `FFL` data. In practice, however, (C.1.5) has two singularities:

- **#1.** All we know *a priori* is $\Omega(\mathbf{r}, eV = 0) = 0$, which gives $k(\mathbf{r}) = -\infty$.
- **#2.** $\texttt{FFL}(\mathbf{r})$ is negligibly small so the integrand diverges near $E_\mathrm{F}$.

## C.2 Singularity #2

There are at least two ways to remove the second singularity. The more intuitive way is using a dataset not identically zero at $E_\mathrm{F}$ in the denominator and its derivative in the numerator. Second derivative of the tunneling current normalized to the differential conductance

$$\frac{\texttt{2FL}}{\texttt{1FL}} = \frac{d^2I/dV^2}{dI/dV} \equiv h(\mathbf{r}, eV)$$

is one such combination where the integral from zero bias is not improper. The $h(\mathbf{r}, eV)$ can be rewritten in terms of setup-free differential conductance $\tilde{g}$ in which the tip-sample distance factor $S(\mathbf{r})$ is spatially uniform (see (C.1.3)):

$$h(\mathbf{r}, eV) = \frac{d\tilde{g}/dV}{\tilde{g}}$$

Solution to this differential equation is

$$\tilde{g}(\mathbf{r}, eV) = \tilde{g}(\mathbf{r}, 0) \cdot \exp \int_0^V h(\mathbf{r}, eV')dV' \tag{C.2.1}$$

With no further *a priori* information, we have only (re-)expressed the setup-free differential conductance in terms of its value at zero-bias, which we do not know.

## C.3 Another trick

Instead of $\texttt{1FL}/\texttt{FFL}$, we can try $\texttt{1FL}/(\texttt{FFL}/V)$ or $(dI/dV)/(I/V)$ which Feenstra *et al.* found to be nearly tip-sample-distance ($d$ in (C.1.1)) independent.[188] As V is a purely independent external variable, this ratio does not depend on $d$ for the same reason as (C.1.4) is free from the setup effect.

The authors avoid the singularity of the ratio by exponentially broadening the total conductance $(I/V)$ spectrum over the gap energy scale (∼1eV in GaAs semiconductor). But the singularity #2 near $E_\mathrm{F}$ is already absent due to the fact that $(dI/dV)/(I/V)$ approaches unity when $|V|$ is very small, regardless of bias as well as location.

Let $\tilde{I}$ denote setup-free current ($S(\mathbf{r}) = S$ in (C.1.2)), and $f(\mathbf{r}, V)$ the differential conductance normalized by the total conductance:

$$\frac{\texttt{1FL}}{\texttt{FFL}/V} \equiv f(\mathbf{r}, V) = \frac{d\tilde{I}/dV}{\tilde{I}/V}$$

Integration after separation of variable gives

$$\int_{\tilde{I}(0)}^{\tilde{I}(V)} \frac{d\tilde{I}}{\tilde{I}} = \log[\tilde{I}(\mathbf{r}, V)] - \log[\tilde{I}(\mathbf{r}, 0)] = \int_0^V \frac{f(\mathbf{r}, V')}{V'} dV' \tag{C.3.1}$$

Here we have extra singularities on both sides: (1) logarithm of zero (current) (2) 1/V. For both we can take advantage of their spatial homogeneity at low energy. First, $\tilde{I} \sim V \cdot (d\tilde{I}/dV)|_{V=0}$ at small V so that the term in the middle becomes

$$\log[\tilde{I}(\mathbf{r},0)] \simeq \log\left[\frac{d\tilde{I}}{dV}(\mathbf{r},0)\right] + \log V$$

where the singularity of logarithm is extracted to the location-independent second term $(\log V)$.

Second, $f(\mathbf{r},V)/V \sim 1/V$ at small V, losing both $\mathbf{r}$ and $V$ dependence. So if we rewrite (C.3.1) as

$$\log[\tilde{I}(\mathbf{r},V)] - \log\left[\frac{d\tilde{I}}{dV}(\mathbf{r},0)\right] - \log V = \int_0^{\delta} \frac{f(\mathbf{r},V')}{V'}dV' + \int_{\delta}^{V} \frac{f(\mathbf{r},V')}{V'}dV'$$

or

$$\log\left[\frac{\tilde{I}(\mathbf{r},V)}{d\tilde{I}/dV(\mathbf{r},0)}\right] - \int_{\delta}^{V} \frac{f(\mathbf{r},V')}{V'}dV' = \int_0^{\delta} \frac{f(\mathbf{r},V')}{V'}dV' + \log V \tag{C.3.2}$$

where $\delta$ defines the range of 'small' V such that $\tilde{I} \sim V \cdot (d\tilde{I}/dV)$ for $|V| < \delta$, the right-hand side is location-independent. Since the integral on the left-hand side can be evaluated from the actual data, we can obtain setup-free $\tilde{I}$ as a function of bias in terms of $g(\mathbf{r},0) = d\tilde{I}/dV(\mathbf{r},0)$, which again we do not know.

In summary, when singularities are eliminated, we only find another form of ratio of two setup-contaminated quantities; $dI/dV$ at one bias divided by $dI/dV$ at another bias as in (C.2.1), $I$ divided by $dI/dV$ as in (C.3.2), etc. It seems to be a quite general rule, that multiplicative setup factor (or setup-free quantity) cannot be uniquely determined nor eliminated without introducing some form of singularity. Analogous to indeterminate equations where the number of unknown variables is greater than the number of given equations.

One other point to note is that these are all 'local' quantities defined at each measurement position. Individual location has its own multiplicative factor, and there is no systematic way to associate the factors at different locations.

## C.4 Partial disproof

One straightforward way to drop the tip-sample-distance factor in (C.1.1) is to take logarithmic derivative with respect to bias voltage. It leads to setup-free quantity

$$\frac{d(\log I)}{dV} = \frac{e\rho_s(\mathbf{r}, eV)}{\int_0^{eV} \rho_s(\mathbf{r}, \varepsilon)d\varepsilon}$$

but once again in a ratio form. Note that we're simply back to (C.1.4). In inverse operation, integral of (C.1.4) gives back (C.1.1). Which means that the differential conductance normalized by total conductance (`1FL/FFL`) cannot provide any further information beyond (C.1.1). In other words, the equations (C.1.1) and (C.1.4) are a derivative-integral pair. Taking the ratio of such pair of the measured data therefore does not help *at all*.

# Bibliography


[1] Onnes, H. K. The resistance of pure mercury at helium temperatures. *Commun. Phys. Lab. Univ. Leiden* **12**, 120 (1911).

[2] Bardeen, J., Cooper, L. N. & Schrieffer, J. R. Theory of superconductivity. *Phys. Rev.* **108**, 1175 (1957).

[3] Mattuck, R. D. *A Guide to Feynman diagrams in the many-body problem* (Dover publications, Inc., 1992).

[4] Phillips, P. *Advanced solid state physics* (Westview Press, 2003).

[5] Fetter, A. L. & Walecka, J. D. *Quantum theory of many-particle systems* (Dover publications, Inc., 2003).

[6] Schrieffer, J. R. *Theory of superconductivity* (Westview Press, 1999).

[7] Yoichiro, N. Quasi-particles and gauge invariance in the theory of superconductivity. *Phys. Rev.* **117**, 648 (1960).

[8] Eliashberg, G. Interactions between electrons and lattice vibrations in a superconductor. *Soviet Physics JETP* **11**, 696 (1960).

[9] Scalapino, D. *Superconductivity*, vol. 1 (Marcel Dekker, Inc., 1969).

[10] Schrieffer, J. R., Scalapino, D. J. & Wilkins, J. W. Effective tunneling density of states in superconductors. *Phys. Rev. Lett.* **10**, 336 (1963).

[11] Rowell, J. M., Anderson, P. W. & Thomas, D. E. Image of the phonon spectrum in the tunneling characteristic between superconductors. *Phys. Rev. Lett.* **10**, 334 (1963).

[12] Tinkham, M. *Introduction to Superconductivity* (McGraw-Hill, 1996).

[13] Schmidt, A. R. *et al.* Imaging the fano lattice to 'hidden order' transition in $URu_2Si_2$. *Nature* **465**, 570 (2010).

[14] Steglich, F. *et al.* Superconductivity in the presence of strong pauli paramagnetism: $CeCu_2Si_2$. *Phys. Rev. Lett.* **43**, 1892 (1979).

[15] Pfleiderer, C. Superconducting phases of $f$-electron compounds. *Rev. Mod. Phys.* **81**, 1551 (2009).

[16] Petrovic, C. *et al.* Heavy-Fermion superconductivity in $CeCoIn_5$ at 2.3K. *Journal of the Physics: Condensed Matter* **13**, L337 (2001).

[17] Jrome, D., Mazaud, A., Ribault, M. & Bechgaard, K. Superconductivity in a synthetic organic conductor $(TMTSF)_2PF_6$. *Journal de Physique Letter* **41**, 95 (1980).

[18] Urayama, H. *et al.* A new ambient pressure organic superconductor based on BEDT-TTF with $T_c$ higher than 10K ($T_c$=10.4K). *Chemistry Letters* **17**, 55 (1988).

[19] Ardavan, A. *et al.* Recent topics of organic superconductors. *Journal of the Physical Society of Japan* **81**, 011004 (2012).

[20] Xiang, X. D., Hou, J. G., Crespi, V. H., Zettl, A. & Cohen, M. L. Three-dimensional fluctuation conductivity in superconducting single crystal $K_3C_{60}$ and $Rb_3C_{60}$. *Nature* **361**, 54 (1993).

[21] Emery, N., Hérold, C., Marêché, J.-F. & Lagrange, P. Synthesis and superconducting properties of $CaC_6$. *Science and Technology of Advanced Materials* **9**, 044102 (2008).

[22] Maeno, Y. *et al.* Superconductivity in a layered perovskite without copper. *Nature* **372**, 532 (1994).

[23] Maeno, Y., Rice, T. M. & Sigrist, M. The intriguing superconductivity of strontium ruthenate. *Physics Today* **54**, 42 (2001).

[24] Luke, G. M. *et al.* Time-reversal symmetry-breaking superconductivity in $Sr_2RuO_4$. *Nature* **394**, 558 (1998).

[25] Nagamatsu, J., Nakagawa, N., Muranaka, T., Zenitani, Y. & Akimitsu, J. Superconductivity at 39K in magnesium diboride. *Nature* **410**, 63 (2001).

[26] Bud'ko, S. L. *et al.* Boron isotope effect in superconducting $MgB_2$. *Phys. Rev. Lett.* **86**, 1877 (2001).

[27] Moshchalkov, V. *et al.* Type-1.5 superconductivity. *Phys. Rev. Lett.* **102**, 117001 (2009).

[28] Kamihara, Y., Watanabe, T., Hirano, M. & Hosono, H. Iron-based layered superconductor $La[O_{1-x}F_x]FeAs$ (x = 0.05-0.12) with $T_c$ = 26K. *Journal of the American Chemical Society* **130**, 3296 (2008).

[29] http://iopscience.iop.org/0034-4885/74/12.

[30] Bednorz, J. G. & Mller, K. A. Possible high $T_c$ superconductivity in the BaLaCuO system. *Zeitschrift für Physik B Condensed Matter* **64**, 189 (1986).

[31] Kishio, K. *et al.* New high temperature superconducting oxides. $(La_{1-x}Sr_x)_2CuO_{4-\delta}$ and $(La_{1-x}Ca_x)_2CuO_{4-\delta}$. *Chemistry Letters* **16**, 429 (1987).

[32] Cava, R. J., van Dover, R. B., Batlogg, B. & Rietman, E. A. Bulk superconductivity at 36K in $La_{1.8}Sr_{0.2}CuO_4$. *Phys. Rev. Lett.* **58**, 408 (1987).

[33] Wu, M. K. *et al.* Superconductivity at 93K in a new mixed-phase Y-Ba-Cu-O compound system at ambient pressure. *Phys. Rev. Lett.* **58**, 908 (1987).

[34] Maeda, H., Tanaka, Y., Fukutomi, M. & Asano, T. A new high-$T_c$ oxide superconductor without a rare earth element. *Jpn. J. Appl. Phys* **27**, L209 (1988).

[35] Sheng, Z. Z. & Hermann, A. M. Bulk superconductivity at 120K in the Tl-Ca/Ba-Cu-O system. *Nature* **332**, 138 (1988).

[36] Schilling, A., Cantoni, M., Guo, J. D. & Ott, H. R. Superconductivity above 130K in the Hg-Ba-Ca-Cu-O system. *Nature* **363**, 56 (1993).

[37] Gao, L. *et al.* Superconductivity up to 164K in $HgBa_2Ca_{m-1}Cu_mO_{2m+2+\delta}$ (m=1,2, and 3) under quasihydrostatic pressures. *Phys. Rev. B* **50**, 4260 (1994).

[38] Jorgensen, J. D. *et al.* Lattice instability and high-$T_c$ superconductivity in $La_{2-x}Ba_xCuO_4$. *Phys. Rev. Lett.* **58**, 1024 (1987).

[39] Jorgensen, J. D. *et al.* Structural properties of oxygen-deficient $YBa_2Cu_3O_{7-\delta}$. *Phys. Rev. B* **41**, 1863 (1990).

[40] Yamamoto, A. *et al.* Rietveld analysis of the modulated structure in the superconducting oxide $Bi_2(Sr,Ca)_3Cu_2O_{8+x}$. *Phys. Rev. B* **42**, 4228 (1990).

[41] Shimizu, S. *et al.* High-temperature superconductivity and antiferromagnetism in multilayer cuprates: $^{63}$Cu and $^{19}$F NMR on five-layer $Ba_2Ca_4Cu_5O_{10}(F,O)_2$. *Phys. Rev. B* **85**, 024528 (2012).

[42] Fisher, L. M., Kalinov, A. V., Savelev, S. E., Voloshin, I. F. & Yampolskii, V. A. Critical current anisotropy in YBCO superconducting samples. *Physica C* **309**, 284 (1998).

[43] Gu, G. D., Puzniak, R., Nakao, K., Russell, G. J. & Koshizuka, N. Anisotropy of Bi-2212 superconducting crystals. *Superconductor Science and Technology* **11**, 1115 (1998).

[44] Chang, J. *et al.* Decrease of upper critical field with underdoping in cuprate superconductors. *Nat. Phys.* **2**, 537 (2006).

[45] http://www.lanl.gov/orgs/mpa/nhmfl/.

[46] Batlogg, B. Physical properties of high-$T_c$ superconductors. *Physics Today* **44**, 44 (1991).

[47] Tallon, J. L., Loram, J. W., Cooper, J. R., Panagopoulos, C. & Bernhard, C. Superfluid density in cuprate high-$T_c$ superconductors: a new paradigm. *Phys. Rev. B* **68**, 180501 (2003).

[48] Hubbard, J. Electron correlations in narrow energy bands. *Proceedings of the Royal Society A* **276**, 238 (1963).

[49] Zhang, F. C. & Rice, T. M. Effective hamiltonian for the superconducting Cu oxides. *Phys. Rev. B* **37**, 3759 (1988).

[50] Uchida, S. *et al.* Optical spectra of $La_{2-x}Sr_xCuO_4$: Effect of carrier doping on the electronic structure of the $CuO_2$ plane. *Phys. Rev. B* **43**, 7942 (1991).

[51] Ohta, Y., Tohyama, T. & Maekawa, S. Charge-transfer gap and superexchange interaction in insulating cuprates. *Phys. Rev. Lett.* **66**, 1228 (1991).

[52] Mizuno, Y. *et al.* Electronic states and magnetic properties of edge-sharing Cu-O chains. *Phys. Rev. B* **57**, 5326 (1998).

[53] Eisaki, H. *et al.* Effect of chemical inhomogeneity in bismuth-based copper oxide superconductors. *Phys. Rev. B* **69**, 064512 (2004).

[54] Armitage, N. P., Fournier, P. & Greene, R. L. Progress and perspectives on electron-doped cuprates. *Rev. Mod. Phys.* **82**, 2421 (2010).

[55] Varma, C. High-temperature superconductivity: Mind the pseudogap. *Nature* **468**, 184 (2010).

[56] Cooper, R. A. *et al.* Anomalous criticality in the electrical resistivity of $La_{2-x}Sr_xCuO_4$. *Science* **323**, 603 (2009).

[57] Norman, M. R., Pines, D. & Kallin, C. The pseudogap: friend or foe of high $T_c$? *Adv. Phys.* **54**, 715 (2005).

[58] Hüfner, S., Hossain, M. A., Damascelli, A. & Sawatzky, G. A. Two gaps make a high-temperature superconductor? *Rep. Prog. Phys.* **71**, 062501 (2008).

[59] Tranquada, J. M., Sternlieb, B. J., Axe, J. D., Nakamura, Y. & Uchida, S. Evidence for stripe correlations of spins and holes in copper oxide superconductors. *Nature* **375**, 561 (1995).

[60] Hirschfeld, P. J., Korshunov, M. M. & Mazin, I. I. Gap symmetry and structure of Fe-based superconductors. *Rep. Prog. Phys.* **74**, 124508 (2011).

[61] Alldredge, J. W. *et al.* Evolution of the electronic excitation spectrum with strongly diminishing hole density in superconducting $Bi_2Sr_2CaCu_2O_{8+\delta}$. *Nat. Phys.* **4**, 319 (2008).

[62] Kondo, T., Takeuchi, T., Kaminski, A., Tsuda, S. & Shin, S. Evidence for two energy scales in the superconducting state of optimally doped $(Bi, Pb)_2(Sr, La)_2CuO_{6+\delta}$. *Phys. Rev. Lett.* **98**, 267004 (2007).

[63] Zeng, B. *et al.* Anisotropic structure of the order parameter in $FeSe_{0.45}Te_{0.55}$ revealed by angle-resolved specific heat. *Nat. Comm.* **1**, 112 (2010).

[64] Hardy, W. N., Bonn, D. A., Morgan, D. C., Liang, R. & Zhang, K. Precision measurements of the temperature dependence of $\lambda$ in $YBa_2Cu_3O_{6.95}$: Strong evidence for nodes in the gap function. *Phys. Rev. Lett.* **70**, 3999 (1993).

[65] Van Harlingen, D. J. Phase-sensitive tests of the symmetry of the pairing state in the high-temperature superconductors–evidence for $d_{x^2-y^2}$ symmetry. *Rev. Mod. Phys.* **67**, 515 (1995).

[66] Tsuei, C. C. *et al.* Pairing symmetry and flux quantization in a tricrystal superconducting ring of $YBa_2Cu_3O_{7-\delta}$. *Phys. Rev. Lett.* **73**, 593 (1994).

[67] Tsuei, C. C. & Kirtley, J. R. Pairing symmetry in cuprate superconductors. *Rev. Mod. Phys.* **72**, 969 (2000).

[68] Kivelson, S. A. *et al.* How to detect fluctuating stripes in the high-temperature superconductors. *Rev. Mod. Phys.* **75**, 1201 (2003).

[69] Parker, C. V. *et al.* Fluctuating stripes at the onset of the pseudogap in the high-$T_c$ superconductor $Bi_2Sr_2CaCu_2O_{8+x}$. *Nature* **468**, 677 (2010).

[70] Axe, J. D. *et al.* Structural phase transformations and superconductivity in $La_{2-x}Ba_xCuO_4$. *Phys. Rev. Lett.* **62**, 2751 (1989).

[71] Valla, T., Fedorov, A. V., Lee, J., Davis, J. C. & Gu, G. D. The ground state of the pseudogap in cuprate superconductors. *Science* **314**, 1914 (2006).

[72] Ino, A. *et al.* Doping-dependent evolution of the electronic structure of $La_{2-x}Sr_xCuO_4$ in the superconducting and metallic phases. *Phys. Rev. B* **65**, 094504 (2002).

[73] Liang, R., Bonn, D. A. & Hardy, W. N. Evaluation of $CuO_2$ plane hole doping in $YBa_2Cu_3O_{6+x}$ single crystals. *Phys. Rev. B* **73**, 180505 (2006).

[74] Doiron-Leyraud, N. *et al.* Quantum oscillations and the Fermi surface in an underdoped high-$T_c$ superconductor. *Nature* **447**, 565 (2007).

[75] Fong, H. F. *et al.* Neutron scattering from magnetic excitations in $Bi_2Sr_2CaCu_2O_{8+\delta}$. *Nature* **398**, 588 (1999).

[76] Slezak, J. A. *et al.* Imaging the impact on cuprate superconductivity of varying the interatomic distances within individual crystal unit cells. *Proc. Nat'l. Acad. Sci.* **105**, 3203 (2008).

[77] Ikeda, Y. *et al.* Bi, pb-sr-cu-o system including a modulation-free superconductor. *Physica C* **165**, 189 (1990).

[78] Damascelli, A., Hussain, Z. & Shen, Z.-X. Angle-resolved photoemission studies of the cuprate superconductors. *Rev. Mod. Phys.* **75**, 473 (2003).

[79] Kaminski, A. *et al.* Change of fermi-surface topology in $Bi_2Sr_2CaCu_2O_{8+\delta}$ with doping. *Phys. Rev. B* **73**, 174511 (2006).

[80] Manako, T., Kubo, Y. & Shimakawa, Y. Transport and structural study of $Tl_2Ba_2CuO_{6+\delta}$ single crystals prepared by the kcl flux method. *Phys. Rev. B* **46**, 11019 (1992).

[81] Vignolle, B. *et al.* Quantum oscillations in an overdoped high-$T_c$ superconductor. *Nature* **455**, 952 (2008).

[82] Li, Y. *et al.* Unusual magnetic order in the pseudogap region of the superconductor $HgBa_2CuO_{4+\delta}$. *Nature* **455**, 372 (2008).

[83] Kohsaka, Y. *et al.* Growth of na-doped $Ca_2CuO_2Cl_2$ single crystals under high pressures of several GPa. *J. of Am. Chem. Soc.* **124**, 12275 (2002).

[84] Tatsuki, T. *et al.* High-pressure synthesis of superconducting $(Ca,K)_2CuO_2C1_2$. *Physica C* **255**, 61 (1995).

[85] Ronning, F. *et al.* Photoemission evidence for a remnant fermi surface and a d-wavelike dispersion in insulating $Ca_2CuO_2Cl_2$. *Science* **282**, 2067 (1998).

[86] Kohsaka, Y. *et al.* Visualization of the emergence of the pseudogap state and the evolution to superconductivity in a lightly hole-doped Mott insulator. *Nat. Phys.* **8**, 534 (2012).

[87] Kohsaka, Y. *et al.* An intrinsic bond-centered electronic glass with unidirectional domains in underdoped cuprates. *Science* **315**, 1380 (2007).

[88] Hanaguri, T. *et al.* A 'checkerboard' electronic crystal state in lightly hole-doped $Ca_{2-x}Na_xCuO_2Cl_2$. *Nature* **430**, 1001 (2004).

[89] Akimitsu, J., Suzuki, S., Watanabe, M. & Sawa, H. Superconductivity in the nd-sr-ce-cu-o system. *Jpn. J. Appl. Phys.* **27**, L1859 (1988).

[90] Fujita, M., Matsuda, M., Lee, S.-H., Nakagawa, M. & Yamada, K. Low-energy spin fluctuations in the ground states of electron-doped $Pr_{1-x}LaCe_xCuO_{4+\delta}$ cuprate superconductors. *Phys. Rev. Lett.* **101**, 107003 (2008).

[91] Krockenberger, Y. *et al.* Superconductivity phase diagrams for the electron-doped cuprates $R_{2-x}Ce_xCuO_4$ ($R$=La, Pr, Nd, Sm, and Eu). *Phys. Rev. B* **77**, 060505 (2008).

[92] Jin, K., Butch, N. P., Kirshenbaum, K., Paglione, J. & Greene, R. L. Link between spin fluctuations and electron pairing in copper oxide superconductors. *Nature* **476**, 73 (2011).

[93] Zhao, J. *et al.* Electron-spin excitation coupling in an electron-doped copper oxide superconductor. *Nat. Phys.* **7**, 719 (2011).

[94] Warren, W. W. *et al.* Cu spin dynamics and superconducting precursor effects in planes above $T_c$ in $YBa_2Cu_3O_{6.7}$. *Phys. Rev. Lett.* **62**, 1193 (1989).

[95] Appelt, S. *et al.* NMR spectroscopy in the milli-Tesla regime: Measurement of $^1$H chemical-shift differences below the line width. *Chem. Phys. Lett.* **485**, 217 (2010).

[96] Timusk, T. & Statt, B. The pseudogap in high-temperature superconductors: an experimental survey. *Rep. Prog. Phys.* **62**, 61 (1999).

[97] Alloul, H., Ohno, T. & Mendels, P. $^{89}$Y NMR evidence for a Fermi-liquid behavior in $YBa_2Cu_3O_{6+x}$. *Phys. Rev. Lett.* **63**, 1700 (1989).

[98] Kawasaki, S., Lin, C., Kuhns, P. L., Reyes, A. P. & Zheng, G.-Q. Carrier-concentration dependence of the pseudogap ground state of superconducting $Bi_2Sr_{2-x}La_xCuO_{6+\delta}$ revealed by $^{63,65}$Cu-nuclear magnetic resonance in very high magnetic fields. *Phys. Rev. Lett.* **105**, 137002 (2010).

[99] Zheng, G.-Q., Kuhns, P. L., Reyes, A. P., Liang, B. & Lin, C. T. Critical point and the nature of the pseudogap of single-layered copper-oxide $Bi_2Sr_{2-x}La_xCuO_{6+\delta}$ superconductors. *Phys. Rev. Lett.* **94**, 047006 (2005).

[100] Loram, J. W., Mirza, K. A., Cooper, J. R. & Liang, W. Y. Electronic specific heat of $YBa_2Cu_3O_{6+x}$ from 1.8 to 300K. *Phys. Rev. Lett.* **71**, 1740 (1993).

[101] Loram, J. W., Mizra, K. A., Cooper, J. R. & Tallon, J. L. Superconducting and normal state energy gaps in $Y_{0.8}Ca_{0.2}Ba_2Cu_3O_{7-\delta}$ from the electronic specific heat. *Physica C* **282-287**, 1405 (1997).

[102] Loram, J. W., Tallon, J. L. & Liang, W. Y. Absence of gross static inhomogeneity in cuprate superconductors. *Phys. Rev. B* **69**, 060502 (2004).

[103] Loram, J. W., Luo, J., Cooper, J. R., Liang, W. Y. & Tallon, J. L. Evidence on the pseudogap and condensate from the electronic specific heat. *J. Phys. Chem. Solids* **62**, 59 (2001).

[104] Timusk, T. & Tanner, D. *Physical Properties of High Temperature Superconductors I* (World Scientific, 1989).

[105] Takagi, H. *et al.* Systematic evolution of temperature-dependent resistivity in $La_{2-x}Sr_xCuO_4$. *Phys. Rev. Lett.* **69**, 2975 (1992).

[106] Johnson, P. D. *et al.* Doping and temperature dependence of the mass enhancement observed in the cuprate $Bi_2Sr_2CaCu_2O_{8+\delta}$. *Phys. Rev. Lett.* **87**, 177007 (2001).

[107] Basov, D. N. & Timusk, T. Electrodynamics of high-$T_c$ superconductors. *Rev. Mod. Phys.* **77**, 721 (2005).

[108] Homes, C. C., Timusk, T., Liang, R., Bonn, D. A. & Hardy, W. N. Optical conductivity of $c$ axis oriented $YBa_2Cu_3O_{6.70}$: Evidence for a pseudogap. *Phys. Rev. Lett.* **71**, 1645 (1993).

[109] Fong, H. F. *et al.* Neutron scattering from magnetic excitations in $Bi_2Sr_2CaCu_2O_{8+\delta}$. *Nature* **398**, 588 (1999).

[110] http://neutron.magnet.fsu.edu/neutron_scattering.html.

[111] Mook, H. A., Yethiraj, M., Aeppli, G., Mason, T. E. & Armstrong, T. Polarized neutron determination of the magnetic excitations in $YBa_2Cu_3O_7$. *Phys. Rev. Lett.* **70**, 3490 (1993).

[112] Varma, C. M. Non-Fermi-liquid states and pairing instability of a general model of copper oxide metals. *Phys. Rev. B* **55**, 14554 (1997).

[113] Fauqué, B. *et al.* Magnetic order in the pseudogap phase of high-$T_c$ superconductors. *Phys. Rev. Lett.* **96**, 197001 (2006).

[114] Shen, Z.-X. *et al.* Anomalously large gap anisotropy in the *a*-*b* plane of $Bi_2Sr_2CaCu_2O_{8+\delta}$. *Phys. Rev. Lett.* **70**, 1553 (1993).

[115] Tanaka, K. *et al.* Distinct Fermi-momentum–dependent energy gaps in deeply underdoped Bi2212. *Science* **314**, 1910 (2006).

[116] Sacuto, A. *et al.* Electronic raman scattering in copper oxide superconductors: Understanding the phase diagram. *Comptes Rendus Physique* **12**, 480 (2011).

[117] Klein, M. V. *Electronic Raman scattering in Light Scattering in Solids 1* (Springer Verlag, 1983).

[118] Ashcroft, N. & Mermin, D. *Solid state physics* (Brooks Cole, 1976).

[119] Liang, R., Bonn, D. A. & Hardy, W. N. Growth of high quality YBCO single crystals using $BaZrO_3$ crucibles. *Physica C* **304**, 105 (1998).

[120] LeBoeuf, D. *et al.* Electron pockets in the Fermi surface of hole-doped high-$T_c$ superconductors. *Nature* **450**, 533 (2007).

[121] Sebastian, S. E. *et al.* Quantum oscillations from nodal bilayer magnetic breakdown in the underdoped high temperature superconductor $YBa_2Cu_3O_{6+x}$. *Phys. Rev. Lett.* **108**, 196403 (2012).

[122] Xu, Z. A., Ong, N. P., Wang, Y., Kakeshita, T. & Uchida, S. Vortex-like excitations and the onset of superconducting phase fluctuation in underdoped $La_{2-x}Sr_xCuO_4$. *Nature* **406**, 486 (2000).

[123] Emery, V. J. & Kivelson, S. A. Importance of phase fluctuations in superconductors with small superfluid density. *Nature* **374**, 434 (1995).

[124] Sonier, J. E. *et al.* Inhomogeneous magnetic-field response of $YBa_2Cu_3O_y$ and $La_{2-x}Sr_xCuO_4$ persisting above the bulk superconducting transition temperature. *Phys. Rev. Lett.* **101**, 117001 (2008).

[125] Xia, J. *et al.* Polar Kerr-effect measurements of the high-temperature $YBa_2Cu_3O_{6+x}$ superconductor: Evidence for broken symmetry near the pseudogap temperature. *Phys. Rev. Lett.* **100**, 127002 (2008).

[126] He, R.-H. *et al.* From a single-band metal to a high-temperature superconductor via two thermal phase transitions. *Science* **331**, 1579 (2011).

[127] Liu, Y. H. *et al.* Direct observation of the coexistence of the pseudogap and superconducting quasiparticles in $Bi_2Sr_2CaCu_2O_{8+y}$ by time-resolved optical spectroscopy. *Phys. Rev. Lett.* **101**, 137003 (2008).

[128] Hudson, E. W. *Investigating high-$T_c$ superconductivity on the atomic scale by Scanning Tunneling Microscopy.* Ph.D. thesis, University of California at Berkeley (1999).

[129] Taylor, C. B. *Coexistence of Bogoliubov quasiparticles and electronic cluster domains in lightly hole-doped cuprate superconductors.* Ph.D. thesis, Cornell University (2008).

[130] Giaever, I. Energy gap in superconductors measured by electron tunneling. *Phys. Rev. Lett.* **5**, 147–148 (1960).

[131] Bardeen, J. Tunnelling from a many-particle point of view. *Phys. Rev. Lett.* **6**, 57 (1961).

[132] Hoffman, J. E. Spectroscopic scanning tunneling microscopy insights into Fe-based superconductors. *Rep. Prog. Phys.* **74**, 124513 (2011).

[133] Tersoff, J. & Hamann, D. R. Theory of the scanning tunneling microscope. *Phys. Rev. B* **31**, 805 (1985).

[134] Nieminen, J., Lin, H., Markiewicz, R. S. & Bansil, A. Origin of the electron-hole asymmetry in the scanning tunneling spectrum of the high-temperature $Bi_2Sr_2CaCu_2O_{8+\delta}$. *Phys. Rev. Lett.* **102**, 037001 (2009).

[135] Suominen, I., Nieminen, J., Markiewicz, R. S. & Bansil, A. Effect of orbital symmetry of the tip on scanning tunneling spectra of $Bi_2Sr_2CaCu_2O_{8+\delta}$. *Phys. Rev. B* **84**, 014528 (2011).

[136] Pan, S. H., Hudson, E. W. & Davis, J. C. $^3$He refrigerator based very low temperature scanning tunneling microscope. *Review of Scientific Instruments* **70**, 1459 (1999).

[137] Kittel, C. *Introduction to solid state physics* (Wiley, 1996).

[138] Binnig, G. & Rohrer, H. Scanning tunneling microscopy — from birth to adolescence. *Rev. Mod. Phys.* **59**, 615 (1987).

[139] Lee, J. *et al.* Interplay of electronlattice interactions and superconductivity in $Bi_2Sr_2CaCu_2O_{8+\delta}$. *Nature* **442**, 546 (2006).

[140] Morgenstern, M., Haude, D., Meyer, C. & Wiesendanger, R. Experimental evidence for edge-like states in three-dimensional electron systems. *Phys. Rev. B* **64**, 205104 (2001).

[141] Hoffman, J. E. *et al.* Imaging quasiparticle interference in $Bi_2Sr_2CaCu_2O_{8+\delta}$. *Science* **297**, 1148 (2002).

[142] McElroy, K. *et al.* Relating atomic-scale electronic phenomena to wave-like quasiparticle states in superconducting $Bi_2Sr_2CaCu_2O_{8+\delta}$. *Nature* **422**, 592 (2003).

[143] Hoffman, J. E. *A Search for Alternative Electronic Order in the High Temperature Superconductor $Bi_2Sr_2CaCu_2O_{8+\delta}$ by Scanning Tunneling Microscopy.* Ph.D. thesis, University of California, Berkeley (2003).

[144] Kivelson, S. A., Fradkin, E. & Emery, V. J. Electronic liquid-crystal phases of a doped Mott insulator. *Nature* **393**, 550 (1998).

[145] Varma, C. M. Pseudogap phase and the quantum-critical point in copper-oxide metals. *Phys. Rev. Lett.* **83**, 3538 (1999).

[146] Chakravarty, S., Laughlin, R. B., Morr, D. K. & Nayak, C. Hidden order in the cuprates. *Phys. Rev. B* **63**, 094503 (2001).

[147] Kaminski, A. *et al.* Spontaneous breaking of time-reversal symmetry in the pseudogap state of a high-$T_c$ superconductor. *Nature* **416**, 610 (2002).

[148] Chuang, T.-M. *et al.* Nematic electronic structure in the parent state of the iron-based superconductor $Ca(Fe_{1-x}Co_x)_2As_2$. *Science* **327**, 181 (2010).

[149] Borzi, R. A. *et al.* Formation of a nematic fluid at high fields in $Sr_3Ru_2O_7$. *Science* **315**, 214 (2007).

[150] Daou, R. *et al.* Broken rotational symmetry in the pseudogap phase of a high-$T_c$ superconductor. *Nature* **463**, 519 (2010).

[151] Fischer, Ø., Kugler, M., Maggio-Aprile, I., Berthod, C. & Renner, C. Scanning tunneling spectroscopy of high-temperature superconductors. *Rev. Mod. Phys.* **79**, 353 (2007).

[152] McElroy, K. *et al.* Coincidence of checkerboard charge order and antinodal state decoherence in strongly underdoped superconducting $Bi_2Sr_2CaCu_2O_{8+\delta}$. *Phys. Rev. Lett.* **94**, 197005 (2005).

[153] Kohsaka, Y. *et al.* How Cooper pairs vanish approaching the Mott insulator in $Bi_2Sr_2CaCu_2O_{8+\delta}$. *Nature* **454**, 1072 (2008).

[154] McElroy, K. *et al.* Atomic-scale sources and mechanism of nanoscale electronic disorder in $Bi_2Sr_2CaCu_2O_{8+\delta}$. *Science* **309**, 1048 (2005).

[155] Del Maestro, A., Rosenow, B. & Sachdev, S. From stripe to checkerboard ordering of charge-density waves on the square lattice in the presence of quenched disorder. *Phys. Rev. B* **74**, 024520 (2006).

[156] Fradkin, E., Kivelson, S. A., Lawler, M. J., Eisenstein, J. P. & Mackenzie, A. P. Nematic fermi fluids in condensed matter physics. *Annual Review of Condensed Matter Physics* **1**, 153 (2006).

[157] Mesaros, A. *et al.* Topological defects coupling smectic modulations to intraunit-cell nematicity in cuprates. *Science* **333**, 426 (2011).

[158] Corson, J., Mallozzi, R., Orenstein, J., Eckstein, J. N. & Bozovic, I. Vanishing of phase coherence in underdoped $Bi_2Sr_2CaCu_2O_{8+\delta}$. *Nature* **398**, 221 (1999).

[159] Wang, Y., Li, L. & Ong, N. P. Nernst effect in high-$T_c$ superconductors. *Phys. Rev. B* **73**, 024510 (2006).

[160] Wang, Y. *et al.* Field-enhanced diamagnetism in the pseudogap state of the cuprate $Bi_2Sr_2CaCu_2O_{8+\delta}$ superconductor in an intense magnetic field. *Phys. Rev. Lett.* **95**, 247002 (2005).

[161] Bergeal, N. *et al.* Pairing fluctuations in the pseudogap state of copper-oxide superconductors probed by the Josephson effect. *Nat. Phys.* **4**, 608 (2008).

[162] Eschrig, M. & Norman, M. R. Effect of the magnetic resonance on the electronic spectra of high-$T_c$ superconductors. *Phys. Rev. B* **67**, 144503 (2003).

[163] Markiewicz, R. S., Sahrakorpi, S., Lindroos, M., Lin, H. & Bansil, A. One-band tight-binding model parametrization of the high-$T_c$ cuprates including the effect of $k_z$ dispersion. *Phys. Rev. B* **72**, 054519 (2005).

[164] Chatterjee, U. *et al.* Nondispersive Fermi arcs and the absence of charge ordering in the pseudogap phase of $Bi_2Sr_2CaCu_2O_{8+\delta}$. *Phys. Rev. Lett.* **96**, 107006 (2006).

[165] McElroy, K. *et al.* Elastic scattering susceptibility of the high temperature superconductor $Bi_2Sr_2CaCu_2O_{8+\delta}$: A comparison between real and momentum space photoemission spectroscopies. *Phys. Rev. Lett.* **96**, 067005 (2006).

[166] Hanaguri, T. *et al.* Quasiparticle interference and superconducting gap in $Ca_{2-x}Na_xCuO_2Cl_2$. *Nat. Phys.* **3**, 865 (2007).

[167] Hanaguri, T. *et al.* Coherence factors in a high-$T_c$ cuprate probed by quasi-particle scattering off vortices. *Science* **323**, 923 (2009).

[168] Li, Y. *et al.* Feedback effect on high-energy magnetic fluctuations in the model high-temperature superconductor $HgBa_2CuO_{4+\delta}$ observed by electronic raman scattering. *Phys. Rev. Lett.* **108**, 227003 (2012).

[169] Rourke, P. M. C. *et al.* Phase-fluctuating superconductivity in overdoped $La_{2-x}Sr_xCuO_4$. *Nat. Phys.* **7**, 455 (2011).

[170] Grbić, M. S. *et al.* Temperature range of superconducting fluctuations above $T_c$ in $YBa_2Cu_3O_{7-\delta}$ single crystals. *Phys. Rev. B* **83**, 144508 (2011).

[171] Kondo, T. *et al.* Disentangling cooper-pair formation above the transition temperature from the pseudogap state in the cuprates. *Nat. Phys.* **7**, 21 (2010).

[172] Sheet, G. *et al.* Phase-incoherent superconducting pairs in the normal state of $Ba(Fe_{1-x}Co_x)_2As_2$. *Phys. Rev. Lett.* **105**, 167003 (2010).

[173] Ren, J. K. *et al.* Energy gaps in $Bi_2Sr_2CaCu_2O_{8+\delta}$ cuprate superconductors. *Sci. Rep.* **2**, 248 (2012).

[174] Hoffman, J. E. *et al.* A four unit cell periodic pattern of quasi-particle states surrounding vortex cores in $Bi_2Sr_2CaCu_2O_{8+\delta}$. *Science* **295**, 466 (2002).

[175] Howald, C., Eisaki, H., Kaneko, N. & Kapitulnik, A. Coexistence of periodic modulation of quasiparticle states and superconductivity in $Bi_2Sr_2CaCu_2O_{8+\delta}$. *Proc. Nat'l. Acad. Sci.* **100**, 9705 (2003).

[176] Vershinin, M. *et al.* Local ordering in the pseudogap state of the high-tc superconductor $Bi_2Sr_2CaCu_2O_{8+\delta}$. *Science* **303**, 1995 (2004).

[177] Shen, K. M. *et al.* Nodal quasiparticles and antinodal charge ordering in $Ca_{2-x}Na_xCuO_2Cl_2$. *Science* **307**, 901 (2005).

[178] Wise, W. D. *et al.* Charge-density-wave origin of cuprate checkerboard visualized by scanning tunnelling microscopy. *Nat. Phys.* **4**, 696 (2008).

[179] Ma, J.-H. *et al.* Coexistence of competing orders with two energy gaps in real and momentum space in the high temperature superconductor $Bi_2Sr_{2-x}La_xCuO_{6+\delta}$. *Phys. Rev. Lett.* **101**, 207002 (2008).

[180] Meng, J.-Q. *et al.* Momentum-space electronic structures and charge orders of the high-temperature superconductors $Ca_{2-x}Na_xCuO_2Cl_2$ and $Bi_2Sr_2CaCu_2O_{8+\delta}$. *Phys. Rev. B* **84**, 060513 (2011).

[181] Lee, J. *et al.* Spectroscopic fingerprint of phase-incoherent superconductivity in the cuprate pseudogap state. *Science* **325**, 1099 (2009).

[182] Feng, D. L. *et al.* Signature of superfluid density in the single-particle excitation spectrum of $Bi_2Sr_2CaCu_2O_{8+\delta}$. *Science* **289**, 277 (2000).

[183] Vishik, I. M. *et al.* Phase competition in trisected superconducting dome. *Proc. Nat'l. Acad. Sci.* **109**, 18332 (2012).

[184] Gruner, G. *Density waves in solids* (Westview Press, 2000).

[185] Li, J.-X., Wu, C.-Q. & Lee, D.-H. Checkerboard charge density wave and pseudogap of high-$T_c$ cuprate. *Phys. Rev. B* **74**, 184515 (2006).

[186] Hashimoto, M. *et al.* Doping evolution of the electronic structure in the single-layer cuprate $Bi_2Sr_{2-x}La_xCuO_{6+\delta}$: Comparison with other single-layer cuprates. *Phys. Rev. B* **77**, 094516 (2008).

[187] Lawler, M. J. *et al.* Intra-unit-cell electronic nematicity of the high-$T_c$ copper-oxide pseudogap states. *Nature* **466**, 347 (2010).

[188] Feenstra, R. M., Stroscio, J. A. & Fein, A. P. Tunneling spectroscopy of the Si(111) 2×1 surface. *Surf. Sci.* **181**, 295 (1987).

# Abbreviations

| | |
|---|---|
| **BCS** | **B**ardeen **C**ooper **S**chrieffer |
| **SC** | **S**uper**C**onducting or **S**uper**C**onductivity |
| **OP** | **O**rder **P**arameter or **O**ptimally **D**oped |
| **PG** | **P**seudo**G**ap |
| **HTS** | **H**igh **T**emperature **S**uperconductor |
| **UD** | **U**nder**D**oped |
| **OD** | **O**ver**D**oped |
| **AFM** | **A**nti**F**erro**M**agnetic |
| **SI-STM** | **S**pectroscopic **I**maging **S**canning **T**unneling **M**icroscopy |
| **LDOS** | **L**ocal **D**ensity **O**f **S**states |
| **BG** | **B**o**G**oliubov |
| **QPI** | **Q**uasi **P**article **I**nterference |
| **FOV** | **F**ield **O**f **V**iew |
| **ARPES** | **A**ngle **R**esolved **P**hoto **E**mission **S**pectroscopy |
| **EDC** | **E**nergy **D**istribution **C**urve |
| **MDC** | **M**omentum **D**istribution **C**urve |
| **CBM** | **C**hecker-**B**oard **M**odulation |
| **CDW** | **C**harge **D**ensity **W**ave |
| **BZ** | **B**rillouin **Z**one |

# Symbols

| | |
|---|---|
| $T_c$ | superconducting transition temperature |
| $T^*$ | pseudogap on-set temperature |
| $A(k, \omega)$ | quasiparticle spectral weight |
| $p$ | hole doping level |
| $a_0$ | size of (tetragonal) unit cell |
| $g(\mathbf{r}, E)$ | (real-space) differential conductance |
| $Z(\mathbf{r}, E)$ | (real-space) ratio of $g(\mathbf{r}, E)$ at opposite bias |
| $q^*$ | near-quarter momentum space peak |
| | associated with PG anti-nodal charge ordering |
| $E_F$ | Fermi energy |
| | |
| $\rho_s$ | superfluid density |
| $\omega_D$ | Debye energy |
| $\Delta_{\mathbf{p}}$ | superconducting energy gap (order parameter) |
| $\lambda_{ab}, \lambda_c$ | penetration depth |
| $\xi$ | coherence length |
| $\chi$ | magnetic susceptibility |